Universidade de Évora - Instituto de Investigação e Formação Avançada

Programa de Doutoramento em Engenharia Mecatrónica e Energia

Área de especialização | Energia

Tese de Doutoramento

Modelling and optimisation of porous volumetric receivers in point-focus solar concentration systems

Germilly Reki Morais Barreto

Orientador(es) | Manuel Pedro Ivens Collares-Pereira

Paulo Manuel Ferrão Canhoto

Évora 2020

Universidade de Évora - Instituto de Investigação e Formação Avançada

Programa de Doutoramento em Engenharia Mecatrónica e Energia

Área de especialização | Energia

Tese de Doutoramento

Modelling and optimisation of porous volumetric receivers in point-focus solar concentration systems

Germilly Reki Morais Barreto

Orientador(es) | Manuel Pedro Ivens Collares-Pereira

Paulo Manuel Ferrão Canhoto

Évora 2020

A tese de doutoramento foi objeto de apreciação e discussão pública pelo seguinte júri nomeado pelo Diretor do Instituto de Investigação e Formação Avançada:

- Presidente | João Manuel Gouveia Figueiredo (Universidade de Évora)
- Vogal | António Domingos Heitor da Silva Reis (Universidade de Évora)
- Vogal | Luís Filipe Moreira Mendes (Universidade de Lisboa)
- Vogal | Pedro Jorge Martins Coelho (Instituto Superior Técnico)
- Vogal | Szabolcs Varga (Universidade do Porto - Faculdade de Engenharia)
- Vogal-orientador | Paulo Manuel Ferrão Canhoto (Universidade de Évora)

Évora 2020

To the memory of my grandparents Maria da Cruz and João Barreto

Summary

In this work, a detailed three-dimensional numerical model of porous volumetric receivers coupled to point-focus solar concentration systems is developed and used to optimise the thermal efficiency and pressure drop. A cylindrical receiver element made of open-cell SiC ceramic foam is considered using air as heat transfer fluid, and a parabolic dish concentrator is simulated to generate the concentrated solar radiation flux at the receiver inlet. The propagation and absorption of solar radiation is modelled through an in-house Monte Carlo Ray Tracing (MCRT) algorithm, in which the asymmetry factor of the scattering phase function was determined by combining this method with experimental measurements of hemispherical diffuse reflectance for five different samples. The fluid flow and heat transfer processes are simulated through a Computational Fluid Dynamics (CFD) model based on the Local Thermal Non-Equilibrium approach, developed using an open source software (OpenFOAM). The global model is used to conduct a comprehensive parametric analysis and optimisation where the geometric parameters of the receiver (porosity and pores size) and concentration system and the fluid flow conditions that maximise the performance of porous volumetric receivers are obtained. It was found that the main thermal losses are due to the backscattering, and the conditions to achieve high thermal efficiency while not increasing pressure drop correspond to receivers with higher porosity and pores size. For a given porosity, there is a pores size that maximise thermal efficiency, being this value lower for increasing porosity. It was also found that the optimum geometric parameters do not depend significantly on the velocity at the receiver inlet, and thus the mass flow rate of heat transfer fluid can be selected as a function of the target temperature at the outlet.

Resumo

Modelação e otimização de recetores volumétricos porosos em sistemas de concentração solar de foco pontual

Neste trabalho foi desenvolvido um modelo numérico tridimensional detalhado de recetores volumétricos porosos acoplados a sistemas de concentração solar de foco pontual, e depois usado para otimizar a eficiência térmica e a queda de pressão. Foi considerado um elemento de recetor cilíndrico feito de espuma cerâmica de SiC de células abertas usando ar como fluido de transferência de calor, e foi simulado um concentrador de disco parabólico para gerar o fluxo de radiação solar concentrada na entrada do recetor. A propagação e absorção de radiação solar é modelada através de um algoritmo de Monte Carlo de Traçamento de Raios (MCRT), onde o fator de assimetria da função de fase de espalhamento de radiação foi determinado combinando esse método com medições experimentais de refletância difusa hemisférica de cinco amostras diferentes. O escoamento e os processos de transferência de calor são simulados num modelo de Dinâmica dos Fluidos Computacional (CFD) baseado na abordagem de Não-Equilíbrio Térmico Local, que foi desenvolvido usando um software de código aberto (OpenFOAM). O modelo global é usado para fazer uma análise paramétrica abrangente e otimização, onde são obtidos os parâmetros geométricos do recetor (porosidade e dimensão dos poros) e do sistema de concentração e as condições de escoamento que maximizam o desempenho de recetores volumétricos porosos. Verificou-se que as principais perdas térmicas são devidas ao retroespalhamento e que as condições para obter alta eficiência térmica sem aumentar a queda de pressão correspondem a recetores com maiores porosidades e tamanho dos poros. Para uma dada porosidade, existe um tamanho dos poros que maximiza a eficiência térmica, sendo esse menor quando maior a porosidade. Verificou-se também que os parâmetros geométricos ótimos não dependem significativamente da velocidade na entrada e, assim, o caudal do fluido de transferência de calor pode ser escolhido em função da temperatura pretendida à saída.

Acknowledgments

Firstly, I would like to thank my supervisor Professor Paulo Canhoto for his great patience and always availability and motivation to help. His ideas, comments and suggestions were decisive for the work presented in this thesis. I also thank him for providing me the template of this thesis.

I thank to my co-supervisor Professor Manuel Collares-Pereira for his comments and suggestions which contributed to the development of this work.

I acknowledge the support of the Portuguese National Science Foundation – FCT (Fundação para a Ciência e a Tecnologia) – through the Grant No. SFRH/BD/115923/2016. I also acknowledge the support of the ICT - Institute of Earth Sciences through the funding provided by the European Union through the European Regional Development Fund, included in the COMPETE 2020 (Operational Program Competitiveness and Internationalization) through the ICT project (UID/GEO/04683/2013) with the reference POCI-01–0145-FEDER-007690. A special acknowledgement to Millennium BCP Foundation for their financial support at the beginning of this work.

Acknowledgements are addressed to LANIK ceramic foam company for providing the ceramic foam samples and to the CFD online forum (OpenFOAM) members who helped me on the OpenFOAM coding.

I am grateful to the engineers Frederico Alvarez and Joel Barrenho for their computer support. I thank to Sérgio Aranha, Sandra Velez and Teresa Foito for their support during the experimental work. A special thanks to my colleague Edgar Abreu for sharing the office with me and to my housemate Hilas Miranda for sharing the house with me during these years.

I thank my father Hipólito Barreto, my mother Maria Morais and my uncle Amândio Barreto for their encouragement to accomplish this thesis. I owe great gratitude to the memory of my grandparents Maria da Cruz (Nha Cucha) and João Barreto (Nhô João), to whom I dedicate this thesis.

Contents

List of Papers

This thesis includes the following papers:

I. Germilly Barreto, P. Canhoto, and M. Collares-Pereira. Three-dimensional modelling and analysis of solar radiation absorption in porous volumetric receivers. *Applied Energy*, 215:602-614, 2018. https://doi.org/10.1016/j.apenergy.2018.02.065. [Chapter 2]

II. Germilly Barreto, P. Canhoto, and M. Collares-Pereira. Three-dimensional CFD modelling and thermal performance analysis of porous volumetric receivers coupled to solar concentration systems. *Applied Energy*, 252:113433, 2019. https://doi.org/10.1016/j.apenergy.2019.113433. [Chapter 3]

III. Germilly Barreto, P. Canhoto, and M. Collares-Pereira. Combined experimental and numerical determination of the asymmetry factor of scattering phase functions in porous volumetric solar receivers. *Solar Energy Materials and Solar Cells*, 206:110327, 2020. https://doi.org/10.1016/j.solmat.2019.110327. [Chapter 4]

IV. Germilly Barreto, P. Canhoto, and M. Collares-Pereira. Parametric analysis and optimisation of porous volumetric solar receivers made of open-cell SiC ceramic foam. *Energy*, 200:117476, 2020. https://doi.org/10.1016/j.energy.2020.117476. [Chapter 5]

Other publications related with the subject of the present thesis, but not included, are:

i. Germilly Barreto, P. Canhoto, and M. Collares-Pereira. OpenFOAM solver for 3D modelling of solar thermal volumetric receivers coupled to concentration systems. *In* 3rd Iberian Meeting of OpenFOAM technology, Porto, Portugal, 2019 (oral presentation).

ii. Germilly Barreto, P. Canhoto, and M. Collares-Pereira. Development and validation of a 3D CFD model for simulation of porous volumetric receivers in solar concentration systems. *In* Jornadas ICT 2019, Instituto de Ciências da Terra Évora, Évora, Portugal, 2019 (oral presentation).

iii. Germilly Barreto, P. Canhoto, and M. Collares-Pereira. Modelling of light propagation in porous media: Application to a volumetric solar receiver with porous structure. *In* Jornadas ICT 2017, Instituto de Ciências da Terra, Braga, Portugal, 2017 (poster session).

iv. Germilly Barreto, P. Canhoto, and M. Collares-Pereira. Effect of thickness on the thermo-hydraulic performance of porous volumetric solar receivers with different internal geometries. *In* 8th European Thermal Sciences Conference, Lisboa, Portugal, 2020 (Submitted).

List of Figures

List of Tables

Chapter 1

Introduction

1.1 Preliminary remarks

Concentrated solar power plants (CSP) are one of the most promising clean technologies to replace conventional fossil fuel power plants that contribute to global warming due to greenhouse gas emissions [1, 2]. In the conventional power plants based on the Rankine cycle, vapour at high temperature and pressure is generated through burning of fossil fuels (thermal energy) which is then used to drive a turbine (mechanical energy) that is coupled to an electrical generator. In CSP plants, the same energy conversion process is applied to convert thermal to electrical energy, but in this case the vapour is generated through concentration of solar radiation, which makes it a clean technology. Most actual CSP plants use the water/vapour Rankine cycle in the power block, while thermal oil or molten nitrate salts are used as heat transfer fluids in the solar concentration field and in thermal energy storage. Improving the efficiency of CSP plants is the first step to reduce the energy production cost, which will make them more competitive against conventional technologies [3].

The efficiency of power cycles increases with the temperature difference between the hot and cold sides according to the Carnot's theorem. Therefore, a fundamental solution to increase the efficiency of thermal to electric conversion is making the CSP plants to work with higher temperatures. However, CSP plants are not yet adapted for very high temperatures due to the limitation of the currently used heat transfer fluids to support temperatures above 600 °C [3] in the case of molten salts and about 400 °C in the case of thermal oils. In this sense, research is being targeted to point-focus solar concentration systems coupled to new designs of thermal receivers and heat transfer fluids capable of withstand high temperatures. Among such point-focus solar concentration systems are solar tower [4] and parabolic dish [5] technologies. For the heat transfer fluid, gases are being proposed and tested, such as, air [6, 7, 8] and carbon dioxide at supercritical conditions [9], due to their capabilities to support higher temperatures and to achieve higher efficiencies when combined with Brayton cycles. Regarding high-temperature solar thermal receivers, new configurations are being proposed aiming to use gases as heat transfer fluid. The

main configurations, design and optimisation challenges of these high temperature thermal receivers are addressed in the following section. Among these receivers, a special attention is given to the porous volumetric thermal receivers.

1.2 High-temperature solar thermal receivers

The high-temperature thermal receivers in point-focus solar concentration systems are designed for using gases as heat transfer fluid [10]. The work by Sedighi et al. [10] presents an in-depth look of their configurations, working principle and recent progresses. It is shown that these receivers present the best near-term solution to push CSP systems to higher temperatures, enabling integration with advanced/combined power cycles. Regarding their configurations, these receivers can be divided into two main groups [10]: (i) indirectly-irradiated receivers, in which a physical separation exists between the heat transfer fluid and the surface where concentrated solar radiation is absorbed; and (ii) directly-irradiated receivers, where the heat transfer fluid is in direct contact with the surface where concentrated solar radiation is absorbed. Among the indirectly-irradiated receivers, the tubular receiver is the most mature technology [10]. This configuration consist in an array of thin-walled tubes (normally made of stainless steel), where a pressurized gas flows inside the tubes and the external surface is exposed to the concentrated solar radiation [3]. Sedighi et al. [10] presented a summary of the main designs and thermal performance of tubular receivers. The main drawbacks are the pressure drop in the tubes and the thermal resistance between the heat transfer fluid and the surface where the solar radiation is absorbed [10]. This is one of the reasons for the emergence and development of the directly-irradiated receivers which present very low thermal resistance. The pressure drop still is a problem in this case, but which nevertheless can be minimised. This type of receivers can be divided in two main groups: (i) with a fixed porous structure as absorber; and (ii) suspended solid particles in a gas [10]. The receivers with porous structure [8], also known as porous volumetric receivers, have been studied more thoroughly. In these receivers, solar radiation is absorbed in a volume filled with a porous structure, through which also flows the heat transfer fluid, thus converting solar radiation to thermal energy [11]. The main advantages of these receives are that the fluid is in direct contact with the surface where solar radiation is absorbed and the very high heat transfer area between the solid structure and the fluid. These two characteristics decrease the thermal resistance, which improves the thermal performance, and increase both temperature and power density, that is, the heat exchanged per unit volume, which is an important feature for the design of high-temperature receivers in CSP plants with high concentration factors.

1.2.1 High-temperature porous volumetric receivers

Porous volumetric receivers are drawing attention due to their capabilities to achieve high values of outlet temperature and thermal efficiency [3]. Ávila-Marín [11] reviewed porous volumetric receivers development in CSP plants. The author identified the different receiver configurations, materials, power plant configurations, advantages and main problems. Regarding the geometry of porous volumetric receivers, there are two main configurations, which are honeycomb and open-cell structures [12]. The honeycomb structures comprise parallel channels oriented in the fluid flow direction and arranged in a hexagonal shape, while the open-cell structures are formed by randomly packed open cells. The materials of the solid structure may be metal or ceramic [11], with the ceramic materials, such as silicon carbide (SiC) foam, being the most used because of their resistance to oxidising atmospheres, high melting point, low thermal expansion and thermal shock resistance. These properties make them more suitable for the high temperature applications [13, 12]. Other configurations of porous volumetric receivers can also be found in literature, as for example in the work of Jafari and Wits [14]. Regarding their integration in CSP plants, there are two main configurations, which are open-loop (open volumetric receiver) and closed-loop (pressurized volumetric receiver) systems [11]. The first uses atmospheric air as heat transfer fluid, while the second uses a pressurized gas. For example, Stadler et al. [15] performed a Computational Fluid Dynamics (CFD) analysis of the thermal performance of an open volumetric receiver integrated with a tower type CSP plant. They found thermal efficiencies of 70.9% and 75.4% and mean fluid temperatures at outlet of 650 °C and 450 °C, respectively, which agreed well with experimental measurements. Several studies on these receivers focused on their numerical modelling aiming to obtain thermal and hydrodynamic performances, as discussed in the next sections.

1.2.2 Modelling approaches to simulate the performance of porous volumetric receivers

The main strategies adopted for modelling porous volumetric receivers in CSP systems are reviewed by Avila-Marin et al. [16]. Due to the complexity of modelling solar radiation propagation and absorption in the three-dimensional geometry of the porous structure, as well as fluid flow and heat transfer, some simplifications for its geometry are usually considered. There are two main approaches in the numerical modelling of porous volumetric receivers. The first is the continuous-scale approach (CSA) [17], where the porous media is assimilated to a continuous semi-transparent medium and the volume-averaged concept is used. The other approach is the discrete-scale approach (DSA) [18], where the porous structure is modelled explicitly using a detailed description of the pores geometry. In the DSA approach, the pores geometry

must be fully described, while in the CSA this complexity is not modelled in such detail. Beyond these two methods, Xia et al. [19] and Li et al. [20] proposed a new method known as scale-coupled approach (SCA). This method consists in the combination of the CSA and DSA into a single computational domain, which allows to unite the advantages of both methods, that is, less computational effort (CSA) and accurate prediction of local radiative properties (DSA). Regarding the application of porous volumetric receivers, research is focused on describing energy conversion on macroscopic scale, not in pores scale, which makes the CSA very suitable and the most used approach, since it also requires much less computational effort in comparison to the DSA and SCA methods. Regarding the heat transfer between the solid matrix structure and the fluid, among the various numerical methods available, there are two main approaches used in the case of porous volumetric receivers [11, 16]. The first is the local thermal equilibrium model (LTE), in which the temperatures of the solid and fluid are assumed to be the same, and thus only one energy equation is needed. The second is the local thermal non-equilibrium model (LTNE), in which the temperature of the two phases are considered different, and thus two energy equations are included in the model, one for the solid and other for the fluid, where the heat transfer between them should be described. The LTNE is the most used approach, because of the better accuracy when significant temperature difference between the two phases are expected.

1.2.2.1 Propagation and absorption of solar radiation

Modelling of solar radiation propagation and absorption in porous media plays an important role in theoretical studies of porous volumetric receivers, because the absorbed radiation is the heat source to the receiver. Modelling is usually conducted considering the porous media as a continuum semi-transparent and participating medium (CSA) where the absorption, emission and scattering phenomena are modelled. The fluid is usually considered as a non-participating media of radiation. Radiation propagation and absorption in participating media is well established in literature, as for example in the works of Modest [21] and van de Hulst [22]. There are two main approaches. The first is solving the broadband radiative transfer equation assuming the integration of thermal (infrared) and solar radiation (visible) using one suitable method, as for example the P1 approximation of the spherical harmonics method [23]. The second is modelling separately the propagation and absorption of solar radiation using the Monte Carlo Ray Tracing (MCRT) method [24], and the thermal radiation exchange through the P1 method. The MCRT is the most used strategy due to the high accuracy and simplicity [25, 26]. There are two main approaches in the MCRT method, which are: computation of ray packages with a specific statistical weight [25], in which energy absorption occurs in every interaction

point and their energy decreases gradually; and modelling the propagation of each ray, one by one, until they are absorbed or exit the system [26].

The flux of concentrated solar radiation at the receiver aperture is also an important aspect to consider. In some works a Gaussian distribution of solar radiation is considered [27], however, the concentration system (heliostat field or parabolic dish, for example) can also be modelled through the MCRT method [26]. In the work of Cui et al. [25], solar radiation propagation in a volumetric receiver was modelled using the MCRT method through the ray packages approach and assuming an uniform solar radiation flux in the receiver aperture. On the other hand, in the work by Chen et al. [26], the MCRT is also used with the single ray approach, while a parabolic dish concentrator was modelled to generate the concentrated radiation field. After solar radiation propagation and absorption in the receiver are modelled, the spatial distribution of absorbed radiation is then used in the energy equation of the solid structure (Section 1.2.2.2). Modelling of radiation propagation in porous media by describing the pores scale geometry (DSA) is mostly used to extract the radiative properties of the porous media, as discussed in Section 1.2.3.

1.2.2.2 Fluid flow and heat transfer

To obtain the thermal and hydrodynamic performances of porous volumetric receivers, the fluid flow and heat transfer including the thermal radiation (infrared) exchange must be modelled. Fluid flow and heat transfer modelling in porous media is well established in literature, as for example, in the work of Vafai [17] and Bejan et al. [28], and in the work of Modest [21] for the thermal radiation exchange. The CSA is the most used approach for modelling radiative heat exchange in porous media. For the fluid flow modelling, the volume averaged (CSA) mass and momentum conservation equations are solved [17], which are similar to the Navier-Stokes equations but considering the volume averaged concept and including a source term in the momentum equation based on the Darcy–Forchheimer model to represents the porous media [17]. Several other works describe the pressure drop in porous media as, for example, the works by Wu et al. [29] and Nie et al. [30]. For the heat transfer, the local thermal non-equilibrium (LTNE) approach between the solid and fluid is most often used, and an energy equation of each phase is solved. The heat transfer between the solid and fluid (convection) is being described with correlations obtained through modelling of ideal 3D structures and through experimental measurements [31, 32, 33]. The thermal radiation exchange inside the solid matrix structure is modelled by solving the radiative transfer equation, where the P1 approximation of the spherical harmonics method [21] is most often used.

1.2.3 Radiative properties of porous media

For an accurate modelling of radiation propagation in porous volumetric receivers, the radiative properties of the porous media must be known in detail. Considering the CSA, the radiative properties of interest are the absorption, scattering and extinction coefficients (the latter is the sum of the first two), scattering albedo (ratio between the scattering and extinction coefficients), scattering phase function and emissivity of the solid material [34]. Several studies have been conducted on the prediction of these properties, which can be divided in two main approaches. The first is the combination of experimental measurements with numerical modelling [35] (usually through the CSA) to predict the equivalent volumetric radiative properties. The other approach consists in modelling an idealized structure of the porous media (DSA) obtained through a computational algorithm [34], or modelling the real structure obtained through tomography techniques [36, 37], which allows an accurate prediction of the local radiative properties. In both approaches, the Monte Ray Carlo Tracing (MCRT) method is used to model the radiation propagation. The extinction coefficient has been proved to depend of the geometric parameters (porosity and pores size) and that the scattering albedo depends of the radiative properties of the solid material [34]. The scattering phase function, is one of the most important and difficult radiative properties to estimate. Different phase functions have been proposed for modelling porous volumetric receivers, as can be found, for example, in the works by Zhao et al. [38] and Hou et al. [39].

1.2.4 Optimisation of porous volumetric receivers

Numerical models are also used for optimisation of porous volumetric receivers. They can be used to find optimum geometries of porous structures (porosity and pores size) and fluid flow conditions that maximise the performance of the receiver. Such studies are mainly focused on the: (i) improvement of temperature distribution in the receiver in order to avoid hot spots [40, 41], which can damage the receiver material; and (ii) maximisation of thermal efficiency while keeping low fluid flow resistance [42, 43]. Different techniques can be used to optimise the temperature distribution, such as, receivers with composite porous structures (different porosities) [40], receivers with gradual variation of porosity and pores size [41, 44], and optimisation of the concentrated solar radiation flux at the receiver aperture [45]. However, only a few studies on detailed parametric analysis and optimisation of thermal (efficiency and mean fluid temperature at outlet) and hydrodynamic (pressure drop) performances are found in literature. One of these few examples is the work by Du et al. [43], where a genetic algorithm is coupled to a numerical model aiming to find the receiver configuration that maximises the thermal efficiency and keeps low fluid flow resistance.

1.3 Objectives of the thesis

The purpose of this work is the development and validation of a detailed three-dimensional numerical model of porous volumetric receivers coupled to point-focus solar concentration systems and the use of that global model to optimise the receiver. For this purpose, the following phenomena are considered: (i) concentration of solar radiation; (ii) propagation and absorption of solar radiation in the porous receiver; (iii) flow of the heat transfer fluid; (iv) heat transfer between the fluid and the solid structure; and (v) thermal radiation exchange in the receiver. Once the global model is developed and validated, it will be used to study thermal and hydrodynamic performance of porous volumetric receivers with different: (i) porous structures; (ii) concentrated solar radiation flux in the inlet; and (iii) fluid flow conditions, aiming to provide answers to the current challenges on these receivers optimisation.

1.4 Outline of the thesis

This thesis comprises six chapters. Chapter 1 presents a general introduction to the thesis and the review of the state of the art regarding the porous volumetric receivers modelling and optimisation. Chapter 2 presents a three-dimensional modelling and analysis of solar radiation propagation and absorption in porous volumetric receivers. A parabolic dish was used to generate the concentrated solar radiation field at the receiver inlet, and a Monte Carlo Ray Tracing (MCRT) was developed to study the radiation propagation and absorption in a cylindrical receiver element made of open-cell ceramic foam. Chapter 3 presents the Computational Fluid Dynamics (CFD) modelling and thermal performance analysis of porous volumetric receivers coupled to solar concentration systems, using the same concentration system and geometry of the receiver from Chapter 2. Chapter 4 addresses the combined experimental and numerical determination of the asymmetry factor of scattering phase function in porous volumetric solar receivers. Diffuse reflectance of five different samples is measured and the MCRT method described in the Chapter 2 is used to simulate the same conditions of the experimental apparatus. Chapter 5 addresses a parametric analysis and optimisation of porous volumetric solar receivers made of open-cell SiC ceramic foam. The global model that results from coupling the solar radiation absorption model (Chapter 2) with the fluid flow and heat transfer model (Chapter 3), using the radiative properties determined from experimental measurements and numerical simulations (Chapter 4), was used to investigate the thermal and hydrodynamic performance of receivers with different internal geometries (porosity and pores size) and different fluid flow conditions. Chapters 2 through 5 are published papers to international peer-reviewed journals, as presented in the List of Papers. Chapter 6 presents the general conclusions.

References

[1] O. Behar, A. Khellaf, and K. Mohammedi. A review of studies on central receiver solar thermal power plants. *Renew Sust Energ Rev*, 23:12–39, 2013.

[2] L. Teng and Y. Xuan. Design of a composite receiver for solar-driven supercritical CO2 Brayton cycle. *J CO2 Util*, 32:290–298, 2019.

[3] C. K. Ho and B. D. Iverson. Review of high-temperature central receiver designs for concentrating solar power. *Renew Sust Energ Rev*, 29:835–846, 2014.

[4] C. K. Ho. Advances in central receivers for concentrating solar applications. *Sol Energy*, 38–56, 2017.

[5] W. Schiel and T. Keck. 9 - Parabolic dish concentrating solar power (CSP) systems. In *Concentrating Solar Power Technology*, 284–322. 2012.

[6] F. Bai. One dimensional thermal analysis of silicon carbide ceramic foam used for solar air receiver. *Int J Therm Sci*, 49:2400–2404, 2010.

[7] Q. Li, F. Bai, B. Yang, Z. Wang, B. El Hefni, S. Liu, S. Kubo, H. Kiriki, and M. Han. Dynamic simulation and experimental validation of an open air receiver and a thermal energy storage system for solar thermal power plant. *Appl Energy*, 178:281–293, 2016.

[8] J.-F. P. P. de la Beaujardiere and H. C. R. Reuter. A review of performance modelling studies associated with open volumetric receiver CSP plant technology. *Renew Sust Energ Rev*, 82:3848–3862, 2018.

[9] M. A. Silva-Pérez. Solar power towers using supercritical CO_2 and supercritical steam cycles, and decoupled combined cycles. *Adv Conc Sol Therm Res Techno*, 383–402, 2017.

[10] M. Sedighi, R. V. Padilla, R. A. Taylor, M. Lake, I. Izadgoshasb, and A. Rose. High-temperature, point-focus , pressurised gas-phase solar receivers: A comprehensive review. *Energ Convers Manage*, 185:678–717, 2019.

[11] A. L. Ávila-Marín. Volumetric receivers in Solar Thermal Power Plants with Central Receiver System technology: A review. *Sol Energy*, 85:891–910, 2011.

[12] F. Gomez-Garcia, J. González-Aguilar, G. Olalde, and M. Romero. Thermal and hydrodynamic behavior of ceramic volumetric absorbers for central receiver solar power plants: A review. *Renew Sust Energ Rev*, 57:648–658, 2016.

[13] J.-H. Eom, Y.-W. Kim, and S. Raju. Processing and properties of macroporous silicon carbide ceramics: A review. *J Asian Ceram Soc*, 1:220–242, 2013.

[14] D. Jafari and W. W. Wits. The utilization of selective laser melting technology on heat transfer devices for thermal energy conversion applications: A review. *Renew Sust Energ Rev*, 91:420–442, 2018.

[15] H. Stadler, D. Maldonado, M. Offergeld, P. Schwarzbözl, and J. Trautner. CFD model for the performance estimation of open volumetric receivers and comparison with experimental data. *Sol Energy*, 177:634–641, 2019.

[16] A. L. Avila-Marin, J. Fernandez-Reche, and A. Martinez-Tarifa. Modelling strategies for porous structures as solar receivers in central receiver systems: A review. *Renew Sust Energ Rev*, 111:15–33, 2019.

[17] K. Vafai. *Handbook of porous media*. Taylor and Francis, New York, third edition, 2015.

[18] S. Du, M.-J. Li, Q. Ren, Q. Liang, and Y.-L. He. Pore-scale numerical simulation of fully coupled heat transfer process in porous volumetric solar receiver. *Energy*, 140:1267–1275, 2017.

[19] X.-L. Xia, Y. Li, C. Sun, Q. Ai, and H.-P. Tan. Integrated simulation of continuous-scale and discrete-scale radiative transfer in metal foams. *J Quant Spectrosc Ra*, 212:128–138, 2018.

[20] Y. Li, X.-L. Xia, C. Sun, S.-D. Zhang, and H.-P. Tan. Integrated simulation of continuous-scale and discrete scale radiative transfer in an open-cell foam made of semitransparent absorbing scattering ceramics. *J Quant Spectrosc Ra*, 225: 156–165, 2019.

[21] M. F. Modest. *Radiative Heat Transfer*. Academic Press, New York, third edition, 2013.

[22] H. C. van de Hulst. *Multiple Light Scattering*, volume II. Academic Press, New York, 1980.

[23] Z. Wu, C. Caliot, G. Flamant, and Z. Wang. Coupled radiation and flow modeling in ceramic foam volumetric solar air receivers. *Sol Energy*, 85:2374–2385, 2011.

[24] X. Chen, X.-L. Xia, H. Liu, Y. Li, and B. Liu. Heat transfer analysis of a volumetric solar receiver by coupling the solar radiation transport and internal heat transfer. *Energ Convers Manage*, 114:20–27, 2016.

[25] F. Q. Cui, Y. L. He, Z. D. Cheng, D. Li, and Y. B. Tao. Numerical simulations of the solar transmission process for a pressurized volumetric receiver. *Energy*, 46:618–628, 2012.

[26] X. Chen, X.-L. Xia, X.-H. Dong, and G.-L. Dai. Integrated analysis on the volumetric absorption characteristics and optical performance for a porous media receiver. *Energ Convers Manage*, 105:562–569, 2015.

[27] K. Reddy and S. Nataraj. Thermal analysis of porous volumetric receivers of concentrated solar dish and tower systems. *Renew Energy*, 132:786–797, 2019.

[28] A. Bejan, I. Dincer, S. Lorente, A. F. Miguel, and A. H. Reis. *Porous and Complex Flow Structures in Modern Technologies*. Springer, New York, 2004.

[29] Z. Wu, C. Caliot, F. Bai, G. Flamant, Z. Wang, J. Zhang, and C. Tian. Experimental and numerical studies of the pressure drop in ceramic foams for volumetric solar receiver applications. *Appl Energy*, 87:504–513, 2010.

[30] Z. Nie, Y. Lin, and Q. Tong. Numerical investigation of pressure drop and heat transfer through open cell foams with 3D Laguerre-Voronoi model. *Int J Heat Mass Tran*, 113:819–839, 2017.

[31] Z. Wu, C. Caliot, G. Flamant, and Z. Wang. Numerical simulation of convective heat transfer between air flow and ceramic foams to optimise volumetric solar air receiver performances. *Int J Heat Mass Tran*, 54:1527–1537, 2011.

[32] X.-l. Xia, X. Chen, C. Sun, Z.-h. Li, and B. Liu. Experiment on the convective heat transfer from airflow to skeleton in open-cell porous foams. *Int J Heat Mass Tran*, 106:83–90, 2017.

[33] A. L. Ávila-Marín, C. Caliot, G. Flamant, M. A. de Lara, and J. Fernandez-Reche. Numerical determination of the heat transfer coefficient for volumetric air receivers with wire meshes. *Sol Energy*, 162:317–329, 2018.

[34] Y. Li, X.-L. Xia, C. Sun, S.-D. Zhang, and H.-P. Tan. Volumetric radiative properties of irregular open-cell foams made from semitransparent absorbing-scattering media. *J Quant Spectrosc Ra*, 224:325–342, 2019.

[35] T. J. Hendricks and J. R. Howell. Absorption/Scattering Coefficients and Scattering Phase Functions in Reticulated Porous Ceramics. *J Heat Transfer*, 118:79–87, 1996.

[36] P. Parthasarathy, P. Habisreuther, and N. Zarzalis. Identification of radiative properties of reticulated ceramic porous inert media using ray tracing technique. *J Quant Spectrosc Ra*, 113:1961–1969, 2012.

[37] Y. Li, X.-L. Xia, C. Sun, J. Wang, and H.-P. Tan. Tomography-based radiative transfer analysis of an open-cell foam made of semitransparent alumina ceramics. *Sol Energ Mat Sol C*, 188:164–176, 2018.

[38] S. Zhao, X. Sun, Q. Que, and W. Zhang. Influence of Scattering Phase Function on Estimated Thermal Properties of Al_2O_3 Ceramic Foams. *Int J Thermophys*, 40:11, 2019.

[39] J. Hou, Q. Wei, Y. Yang, and L. Zhao. Experimental evaluation of scattering phase function and optimization of radiation absorption in solar photocatalytic reactors. *Appl Therm En*, 127:302–311, 2017.

[40] X. Chen, X.-L. Xia, X.-W. Yan, and C. Sun. Heat transfer analysis of a volumetric solar receiver with composite porous structure. *Energ Convers Manage*, 136: 262–269, 2017.

[41] S. Du, Q. Ren, and Y.-L. He. Optical and radiative properties analysis and optimization study of the gradually-varied volumetric solar receiver. *Appl Energy*, 207:27–35, 2017.

[42] F. Zaversky, L. Aldaz, M. Sánchez, A. L. Ávila-marín, M. I. Roldán, J. Fernández-Reche, A. Füssel, W. Beckert, and J. Adler. Numerical and experimental evaluation and optimization of ceramic foam as solar absorber – Single-layer vs multi-layer configurations. *Appl Energ*, 210:351–375, 2018.

[43] S. Du, Y.-L. He, W.-W. Yang, and Z.-B. Liu. Optimization method for the porous volumetric solar receiver coupling genetic algorithm and heat transfer analysis. *J Heat Transf*, 122:383–390, 2018.

[44] B. Wang, Y. Hong, L. Wang, X. Fang, P. Wang, and Z. Xu. Development and numerical investigation of novel gradient-porous heat sinks. *Energ Convers Manage*, 106:1370–1378, 2015.

[45] Y.-L. He, K. Wang, Y. Qiu, B.-C. Du, Q. Liang, and S. Du. Review of the solar flux distribution in concentrated solar power: Non-uniform features, challenges, and solutions. *Appl Therm En*, 149:448–474, 2019.

Chapter 2

Three-dimensional modelling and analysis of solar radiation absorption in porous volumetric receivers[†]

Abstract

This work addresses the three-dimensional modelling and analysis of solar radiation absorption in a porous volumetric receiver using the Monte Carlo Ray Tracing (MCRT) method. The receiver is composed of a solid matrix of homogeneous porous material and isotropic properties, bounded on its side by a cylindrical wall that is characterized through a diffuse albedo. The Henyey-Greenstein phase function is used to model the radiation scattering inside the porous media. The effect of the angle of incidence, optical thickness (porosity, pores size and height of the receiver), asymmetry factor of the phase function and wall properties on the solar radiation absorption in the porous media is studied in order to obtain the receiver efficiency as a function of these parameters. The model was validated by comparing the results for a simple geometry composed of a long slab of finite thickness with the values available in the literature, and then tested with a cylindrical receiver using a parabolic dish as concentration system with a concentration factor of 500. A peak of absorbed solar radiation of 156 MW m^{-3} and an absorption efficiency of 90.55% were obtained for a phase function asymmetry factor of 0.4 (forward scattering) and scattering albedo and extinction coefficient of 0.54 and 100 m^{-1}, respectively. The results for the diffuse reflectance, diffuse transmittance and absorption are also presented. The model developed in this work is useful to obtain and understand the energy absorption distribution in porous volumetric receivers coupled to solar concentration systems, when different porous structures and geometric parameters are used.

Keywords: Solar energy; Solar concentration; Volumetric receiver; Porous media; Monte Carlo ray tracing.

[†]Germilly Barreto[(1)], P. Canhoto[(1)], and M. Collares-Pereira[(1)]. Three-dimensional modelling and analysis of solar radiation absorption in porous volumetric receivers. *Applied Energy*, 215:602-614, 2018.

[(1)] Institute of Earth Sciences, University of Évora.

2.1 Introduction

Non-linear solar concentration systems are promising technologies to replace the conventional generation of electricity based on fossil fuels [1]. In recent years, a notable progress in concentrating solar thermal energy was achieved in terms of improving reflector designs, materials and heat transfer fluids, thermal to electric energy conversion and energy storage [2]. In these systems, two important components are the solar concentrators, which should concentrate the solar radiation on the thermal receiver, and the thermal receiver itself, where solar radiation is converted to thermal energy. In the recent work of Ho and Iverson [3], a description of typical configurations of solar thermal receivers is made and, according to that work, the volumetric thermal receivers present great challenges from the point of view of their numerical modelling and optimization. The volumetric receivers with solid matrix (porous media) have been under investigation, mainly due to their capability to achieve high values of temperature and thermal efficiency, being one of the most promising technologies to improve the thermal efficiency of solar concentration power systems [4, 5, 6, 7]. In the work of Ávila-Marín [8], a chronological review of volumetric receivers development associated with concentrating solar power (CSP) plants is presented. The author identified the various receiver configurations, materials, power plant configurations, advantages and main problems.

In terms of modelling porous volumetric receivers associated with CSP plants, the recent work of de la Beaujardiere and Reuter [9] presents a review of performance modelling of these systems, including the energy conversion system, the thermal energy storage and the receiver modelling. Regarding the receiver modelling, two different fields of study can be identified. One of them is the absorption of solar radiation in the porous media, in which the Monte Carlo Ray Tracing (MCRT) method [6, 10, 11] is used, and the other one is the integration of solar radiation absorption with fluid flow and heat transfer modelling in order to obtain the thermal performance of receivers [7, 12, 13]. The MCRT method used to describe the light transport in biological media [14, 15, 16] can be also used to solve the problem of light transport in porous media with solid matrix [6, 10, 11]. In this case, there are two possible approaches: one is the computation of the propagation of ray packages with a specified statistical weigth [10, 11, 14], in which energy absorption occurs in every interaction point and their energy decreases gradually; and the other one is the modelling of propagation of each ray, one by one, until they are absorbed or exit the system [6].

Wang et al. [14] addressed the light transport in multi-layered tissues using MCRT method and presented the results of diffuse reflectance and transmittance as function of the exit angle, which were validated with data from the work of van de Hulst [17].

Gao et al. [18] modelled and studied the effect of incidence angle, optical thickness and asymmetry factor on the diffuse reflectance of a infinite slab turbid medium. They found that for large optical thickness and small incidence angles, the angular distribution of diffuse reflectance is similar to that of Lambertian surface. In the work of Cui et al. [10], solar radiation propagation in a pressurized volumetric receivers was modelled using the MCRT method and assuming a solar radiation flux in the front face of the receiver while a non-uniform cylindrical coordinate grid was employed in the statistical analisys of energy distribution. This technique reduces the number of cells and computation time compared to that for a uniform grid. He et al. [11] did a similar study but using a heliostat field as concentration system. In other works [10, 11, 14], the MCRT method was based on the propagation of ray packages while in the work of Chen et al. [6] the same method was implemented by computing the propagation of every single ray. They used a parabolic dish as the concentration system and studied the effects of porous structure parameters, slope error of the concentrator and receiver misalignment on the performance of the receiver. Zhao and Tang [19] used the MCRT method to determine the extinction coefficients of silicon carbide porous media based on the Fresnel and Beer laws in order to obtain the optical properties of the porous media. They concluded that the extinction coefficient of the silicon carbide strongly depends on the porosity and pores size. Gomez-Garcia et al. [20] modelled the radiation propagation in a porous volumetric receiver with a stack of thick square grids and also analysed the influence of geometric parameters in the receiver performance, such as the grid length and the gap between consecutive layers.

The thermal energy in the receiver is collected using a heat transfer fluid, which will transfer heat to a thermodynamic cycle that converts thermal to mechanical energy and then to electrical energy through an electric generator. Recently, Benoit et al. [21] did a review of current and future liquid, gas, supercritical, two-phase and particulate heat transfer fluids. Using air as heat transfer fluid in porous volumetric receivers offers significant advantages, such as high conversion efficiency, low environmental impact and the possibility of being used in deserts or other isolated regions with scarce water resources [22].

Regarding the heat transfer processes in the receiver, Capuano et al. [23] presented an overview of various numerical modelling approaches of solar radiation conversion when air is used as heat transfer fluid, developed at the German Aerospace Center (DLR), and results for different numerical models are compared with experimental measurements. Fuqiang et al. [24] studied the effect of using different radiative transfer models (P1 and Rosseland approximation) on the heat transfer modelling of a porous media solar receiver by combining the MCRT method and CFD modelling. They concluded that the difference in the maximum temperature in the solar receiver

between these two approximations is small. According to the work of Smirnova et al. [25], the volumetric receivers are exposed to severe thermal loads, where maximum temperatures of more than 1000 °C are reached. These high thermal loads might reduce the lifetime of the receivers. In this way, Smirnova et al. [25] conducted a study where the effect of thermal loads in the receiver is quantified. They presented the mechanical stresses and the maximum thermal load up to which the receiver should be operated. Recently, Gomez-Garcia et al. [26] presented a review of thermal and hydrodynamic modelling of conventional ceramic volumetric absorbers. They identified the radiative and thermal properties that a good absorber must have, providing values of reference for the characteristics of ceramic volumetric receivers. Fend et al. [27] conducted an experimental study using a variety of porous materials and reported the measuring method and the results for the thermal conductivity, convective heat transfer coefficient and efficiency. Recommendations on the design of volumetric absorbers were also given.

As for the design of the porous volumetric receivers, high porosity or large pores means low pressure drop in the receiver, however this also implies a lower heat transfer coefficient between the porous material and the heat transfer fluid [13]. Therefore, an optimal thermal receiver should have a structure that causes low pressure drop and maintains good heat transfer characteristics. In this regard, Wu et al. [28] presented experimental and numerical studies on the pressure drop in ceramic foams for air receiver applications using two modified structures, and presented an empirical model to predict the pressure drop based on those results. Albanakis et al. [29] did an experimental assessment of the response of various foam materials, and the results showed that the efficiency of porous volumetric receivers depends on both materials characteristics and flow conditions. Roldán et al. [30] investigated the thermal performance of different configurations of volumetric receivers using Computational Fluid Dynamics. They carried out simulations for various values of porosity in order to find the optimal working configurations. Wang et al. [31] presented a novel design of gradient-porous heat sinks for volumetric receivers. They compared the receiver performance to that of an homogeneous porous receiver configuration and concluded that the gradient-porous arrangement can improve both pressure drop and thermal performance. Wu et al. [32] developed a correlation for the local convective heat transfer coefficient between the air flow and ceramic foams based on numerical simulations, and validated it with experimental data. Porous volumetric receivers still is an area of growing research, for example, in terms of radiation flux distribution and experimental study on the efffect of differents geometrical parameters [33], determination of representative elementary volumes [34], techniques to improve its performance, such as volumetric solar receiver with structured packed bed [35], composite porous structure [36] and micro heat

exchangers with multi-leyered porous media which can be used in solar thermal receivers [37]. An interesting and recent study was presented by Zaversky et al. [38] where two different types of one-dimensional models of radiation propagation inside the foam were developed. Those models were checked for consistency against experimental data and then used to optimize the absorbed thermal efficiency by considering single, double and triple layer absorber configurations. They found that the optimized single-layer is the best absorber configuration while, if necessary, the second layer can be used to satisfy mechanical and stability requirements.

The absorption of solar radiation is a very important aspect in the performance of porous volumetric receivers because the spatial distribution of absorbed energy is the source of the heat transfer process. Thus, the first step to optimize the thermal efficiency of a volumetric receiver is understanding how solar radiation is distributed in the receiver and how this distribution and the absorption efficiency are affected by the different characteristic parameters of the receiver. The state of the art shows some gap in the detailed and parametric analysis of solar radiation absorption in porous volumetric receivers. For this reason, a detailed three-dimensional modelling and analysis of solar radiation absorption in a single layer porous media receiver is presented in this work, using the MCRT method to simulate the concentrated solar radiation flux incident in the front face (inlet) of the volumetric receiver. The model includes the effect of the angle of incidence on the absorption of energy while the receiver wall is modelled as a diffuse surface. One of the main innovation of this work is using Henyey-Greenstein phase function to model light scattering inside the porous media. Other contributions of this work are the study of the effect of optical thickness (porosity, pore diameter and height of the receiver), asymmetry factor of the phase function, boundary wall properties and geometric parameters of the concentration system on the distribution and performance of solar radiation absorption in the receiver. Based on the results presented in this paper, a discussion on the distribution of absorbed solar radiation and absorption efficiency are conducted, and the conditions to improve the performance of the receiver are presented.

2.2 Solar radiation propagation and absorption

In this work, solar radiation is concentrated by a parabolic dish in the aperture (front face) of the porous volumetric receiver. Then, radiation propagates inside the pores of the medium until it is absorbed by the porous material or exits the receiver. The propagation and absorption phenomena depend on the two most important geometric characteristics of the porous media, the porosity and the size of the pores, and of others parameters, namely the radiative and thermal properties of the porous material and of the incidence angle that is determined by the type of solar concentration

system. The concentrator generates the spatial distribution of energy flux and angle of incidence at the receiver inlet. Therefore, it is important to study the effect of the incidence angle because the receiver performance will depend on the design and optical efficiency of the concentration system. For this purpose, this work is organized in such way that the model of the solar concentration system and the model of solar radiation propagation and absorption in the porous media are linked through the spatial distribution of energy flux and angle of incidence in the inlet of the receiver. Once the concentration system is modelled through the MCRT method, the spatial distribution of energy flux (coordinates of all rays) and the angle of incidence (unit direction vector of all rays) are obtained in the aperture area of the receiver.

2.2.1 Propagation of solar radiation in the porous media

Porous materials are very complex structures. In practice, the porous media can be heterogeneous, anisotropic and the pores may have many geometric shapes. Moreover, when solar radiation is absorbed in the porous media, its temperature increases and the emissivity and scattering albedo of both the porous material and boundary surface can be affected. These aspects increase the numerical modelling complexity of solar radiation transport in porous media. For that reason, in this work the following simplifications were assumed: the porous media is homogeneous, isotropic, the pores can be modelled as spherical, the emissivity and the scattering albedo of the receiver and wall are uniform and constant.

The MCRT method is also used to model energy absorption in the porous volumetric receiver. The method was implemented in Matlab software using parallel computing to decrease the computation time. When solar radiation enters in the porous volumetric receiver, there are two phenomena that must be considered, that is, absorption and scattering [39]. These two phenomena are illustrated in Fig. 2.1 for the case of a cylindrical receiver with height h_{rec} and radius r_{rec}. The porous

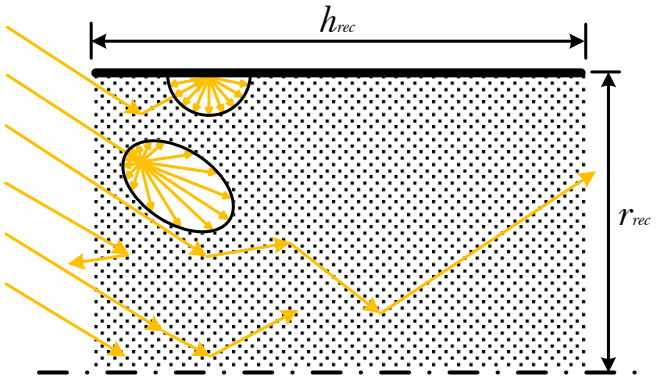

Fig. 2.1: Propagation of solar radiation in a porous volumetric receiver.

media is characterized by a absorption coefficient κ_a, a scattering coefficient κ_s and a extinction coefficient β, which can be expressed in the following way [40], respectively:

$$\kappa_a = 1.5\varepsilon(1-\phi)/d_p \tag{2.1}$$

$$\kappa_s = 1.5(2-\varepsilon)(1-\phi)/d_p \tag{2.2}$$

$$\beta = \kappa_a + \kappa_s = 3(1-\phi)/d_p \tag{2.3}$$

where ϕ is the porosity, d_p the pores diameter and ε is the emissivity of the porous material. In this work, an open porous volumetric receiver (without glass window) is considered [41]. If a glass window is included then the transmissivity of the glass must be known as a function of the incidence angle, and the multiple reflections between the receiver surface and the inner surface of the window should also be modelled. The angle of incidence at the inlet of the receiver will be the same in both cases if the refractive index of the gas in the two sides of the window are the same. In this type of porous volumetric receiver air is usualy used as working fluid; this also means that the relative refractive index is unity and the specular reflectance is zero [14]. Therefore, it is considered that when a ray from the concentration system hits the front surface of the receiver, it directly enters in the receiver [6, 42], and the effects of polarization and dependence on the wavelength of light were neglected. Thus, based on radiation transfer theory and considering the simplifications presented above, when sunlight is transmitted into the receiver, a path length l_β is computed through [39]:

$$l_\beta = -\frac{1}{\beta}\ln\xi \tag{2.4}$$

where ξ is a random number between 0 and 1. Then, another random number ξ is generated to decide if the ray is absorbed or scattered by using the following conditions:

$\xi \leqslant \omega$, scattering

$\xi > \omega$, absorption

in which $\omega = \kappa_s/\beta$ is the scattering albedo. When scattering occurs, spherical coordinates are used to compute the new direction using the polar and azimutal angles. In this work, the Henyey-Greenstein phase function [43] is used to determine the polar angle, which is defined as:

$$p(\theta) = \frac{1}{4\pi}\frac{1-g^2}{(1+g^2-2g\cos\theta)^{3/2}} \tag{2.5}$$

where p is the phase function, θ is the polar angle and g is the asymmetry factor. The asymmetry factor varies between -1 and 1, with -1 being used in the case of full backscattering; 1 is for full forward scattering and 0 for an uniform distribution [43].

In literature there are many other phase functions [17]. The Henyey-Greenstein phase function is often used in the astronomical literature [43], and it allows a smooth variation from isotropic ($g = 0$) to narrow forward peak ($g = 1$) or narrow backward peak ($g = -1$) scattering [17]. Due to these characteristics and simplicity, it is a function ideal for test calculations on multiple light scattering when one want to study the influence of anisotropy with a continuous parameter. The phase function must be normalized, such that the integral over 4π steradians is unity. When normalized, it provides the probability of occurrence of a given polar angle. Fig. 2.2 presents the polar plot of $p(\theta)$ for different values of the asymmetry factor. Then, in the MCRT

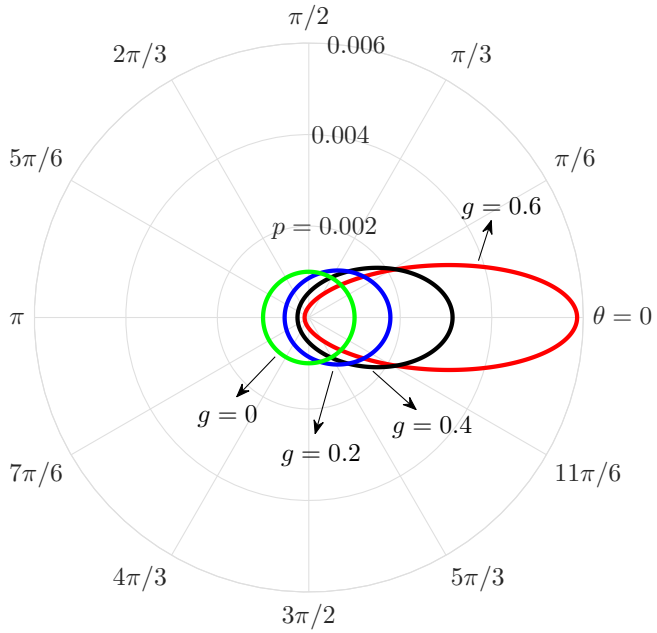

Fig. 2.2: Polar plot of normalized $p(\theta)$ for different values of g.

method, the polar angle θ is expressed as a function of a random number ξ as follows [14]:

$$\theta = \cos^{-1} \begin{cases} \dfrac{1}{2g}\left(1 + g^2 - \left[\dfrac{1-g^2}{1-g+2g\xi}\right]^2\right) & \text{if } g \neq 0 \\ 2\xi - 1 & \text{if } g = 0 \end{cases} \tag{2.6}$$

The azimuthal angle, which is needed to compute the three-dimensional direction of scattering, is uniformly distributed between 0 and 2π and is obtained from [14]:

$$\psi = 2\pi\xi \tag{2.7}$$

based on a new random number ξ. When using the Henyey-Greenstein phase function, a local coordinates system is needed at the point of scattering to calculate the new direction [39]. Therefore, let $\hat{\mathbf{s}}$ ($\hat{\mathbf{v}}_{\mathbf{D}}$ at the inlet of the receiver) be the direction before scattering, and considering that the new polar angle θ' measured from the z-direction

($\hat{\mathbf{s}}$ direction), the local x-direction (from where ψ' is measured) and y-direction are given by:

$$\hat{\mathbf{e}}_{\mathbf{1}} = \mathbf{a} \times \hat{\mathbf{s}} / \mid \mathbf{a} \times \hat{\mathbf{s}} \mid, \qquad \hat{\mathbf{e}}_{\mathbf{2}} = \hat{\mathbf{s}} \times \hat{\mathbf{e}}_{\mathbf{1}} \tag{2.8}$$

respectively, where $\mathbf{a}$ is an arbitrary vector. The new direction $\hat{\mathbf{s}}'$ is computed through:

$$\hat{\mathbf{s}}' = \sin\theta'(\cos\psi'\hat{\mathbf{e}}_{\mathbf{1}} + \sin\psi'\hat{\mathbf{e}}_{\mathbf{2}}) + \cos\theta'\hat{\mathbf{s}} \tag{2.9}$$

and then the new position of the ray is given by:

$$\mathbf{r}_2 = \mathbf{r}_1 + l_\beta \hat{\mathbf{s}}' \tag{2.10}$$

in which $\mathbf{r}_1$ and $\mathbf{r}_2$ are, respectively, the initial and final position vectors of the ray, considering the origin of the global coordinate system located in the center of the receiver inlet, and l_β is given by Eq. (2.4). The rays may reach the wall of the receiver and, in that case, the wall is considered as an ideal diffuse surface with an albedo ω_w. For the receiver of the present work, cylindrical coordinates are used to compute the radial position and check if it is larger than the radius r_{rec}. If this condition is true, then Eq. (2.11) is used to compute the interaction point on the wall:

$$\mathbf{r}_w = \mathbf{r}_1 + f l_\beta \hat{\mathbf{s}}' \tag{2.11}$$

where $\mathbf{r}_w$ is the point on the wall and f is the fraction of l_β that satisfies the condition of radial position in the cylindrical coordinates (equal to r_{rec}). If scattering occurs in the wall then the new direction is computed through Eq. (2.8) and Eq. (2.9) with the $\hat{\mathbf{s}}$ vector in Eq. (2.8) being the unit vector defined by the direction of the radial position (the normal vector to the tangent plane at the point of scattering), and the polar angle for the diffuse reflection is computed through:

$$\theta = \cos^{-1}(\xi - 1) \tag{2.12}$$

in which ξ is a new random number. To determine if the rays exit the receiver through the front side (inlet) or back side (outlet), the following conditions are used:

$h_k < 0$, front side

$h_k \geqslant h_{rec}$, back side

where h_k is the value of the position vector $\mathbf{r}_2$ that corresponds to the depth position of the ray in the receiver. Fig. 2.3 presents the flowchart of the MCRT method to compute the final position of all rays in the porous volumetric receiver including the wall and the rays that exit the receiver.

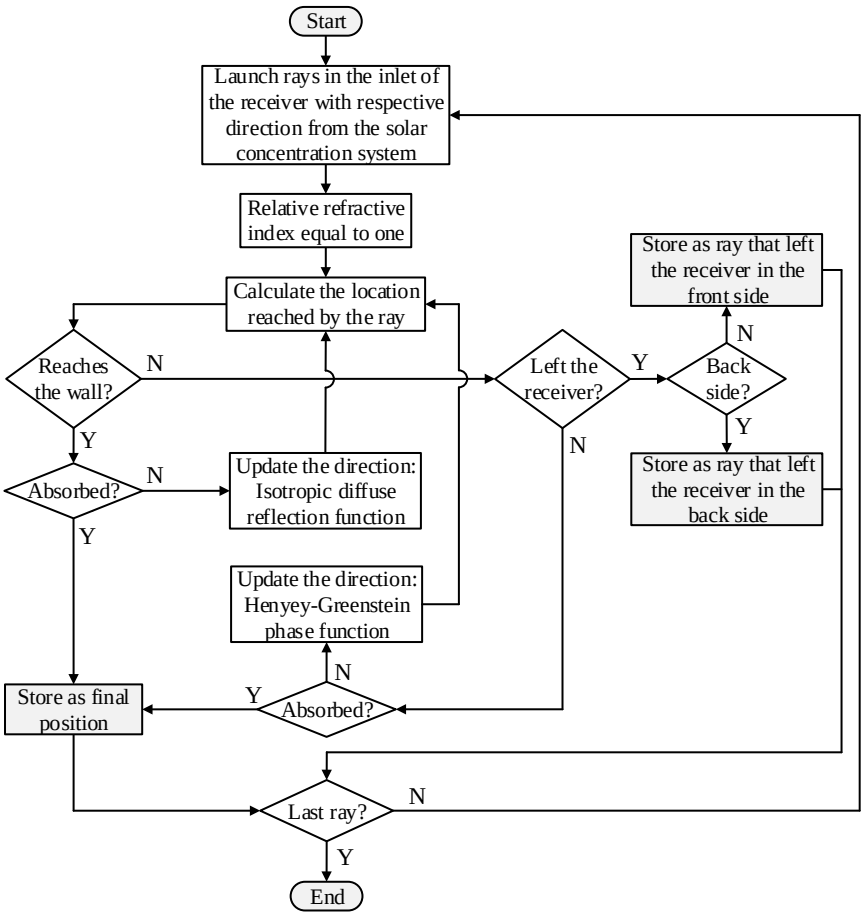

Fig. 2.3: Flowchart of MCRT method for solar radiation transport modelling in porous media.

2.2.2 Volumetric absorption of radiation and efficiencies

After the final position of all rays was computed using the method described in the subsection 2.2.1, a statistical analysis is needed to compute the spatial distribution of the absorbed solar radiation. For this purpose, and considering the cylindrical porous receiver of height h_{rec} and radius r_{rec} of the present work, a discretization of the volume into small elements (cells) is performed, as showed in Fig. 2.4, and the number of rays absorbed in each element is counted. The spatial distribution of absorbed solar radiation per unit of volume is given by:

$$S_{i,j,k} = \frac{N^S_{i,j,k} p}{V_{i,j,k}} \tag{2.13}$$

in which S is the absorbed solar radiation in the element of volume i, j, k of the receiver, N^S is the total number of rays, V is the volume of the cell, and p is the power per ray. The number of cells in each direction of the cylindrical coordinates system used for discretization is presented in Table 2.1. The rays absorbed in the wall are included in the adjacent boundary cells in the radial direction.

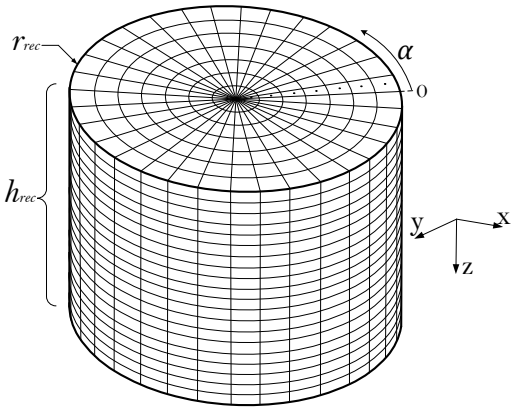

Fig. 2.4: Spatial discretization of the porous volumetric receiver.

To study the performance of the receiver, four quantities are considered, namely, the fraction of energy lost through the receiver inlet (L_{is}) and outlet (L_{os}), the fraction of energy absorbed in the wall W_f and the absorption efficiency η_{abs}, all of them defined with respect of the total energy incident on the receiver aperture, respectively as follows:

$$L_{is} = \frac{N_T^{is}}{N_T^F} \tag{2.14}$$

$$L_{os} = \frac{N_T^{os}}{N_T^F} \tag{2.15}$$

$$W_f = \frac{N_T^w}{N_T^F} \tag{2.16}$$

$$\eta_{abs} = \frac{N_T^S + N_T^w}{N_T^F} \tag{2.17}$$

where N_T^{is} and N_T^{os} are the total number of rays that exit through the front and back surfaces of the receiver, respectively, and N_T^S, N_T^w and N_T^F are the total number of rays absorbed in the volume, absorbed in the wall and incident on the inlet plane of the receiver. It should be noted that the fraction of energy absorbed in the wall is defined separately because it is one of the quantities to be studied, but it is also included in the definition of the absorption efficiency, according to Eq. (2.17). The total power absorbed in the receiver is then given by:

$$P_T = p(N_T^S + N_T^w) \tag{2.18}$$

The geometric and radiative parameters of the porous volumetric receiver used to obtain the simulation results presented in the next sections are given in Table 2.1. The value for the asymmetry factor presented in Table 2.1 and the values that will be presented in Section 2.3 can be obtained by using a combination of different sizes and shapes of the pores, porosity, optical properties of the porous material and foam structure. For example, some foam structures (tomographic, concave kelvin

and convex Weaire-Phelan) were studied in the work by Cunsolo et al. [42]; and micro-/nano-porous medium were addressed in the work by Xu [37].

Table 2.1: Geometric and radiative parameters of the porous volumetric receiver.

Parameter	Value
r_{rec} (cm)	2.5
h_{rec} (cm)	5
d_p (mm)	3
ϕ	0.9
ε	0.92
g	0.4
ω_w	0.2
Number of cells in radial direction	20
Number of cells in azimuthal direction	30
Number of cells in longitudinal direction	100

2.2.3 Sensitivity analysis on the total number of ray used in the MCRT method

The results of the MCRT method depend on the number of rays used in the simulation. However, as these results tend to stabilize with a increasing number of rays, a value can be selected from which that variation is admissible. To select the number of rays, a sensitivity analysis was carried out, using the same method presented in the work of Cui et al. [10]. The most sensible quantity to the number of rays is the spatial distribution of the absorbed solar radiation. In this regard, the average of the deviation of the flux distribution $\overline{\delta}$ with respect to a benchmark solution is used as criterium:

$$\overline{\delta} = \frac{\sum \delta[i,j,k]}{N_v} \tag{2.19}$$

where $\delta[i,j,k]$ is the matrix of the dimensionless deviations of the flux distribution and N_v is the total number of elements of volume (cells). The deviation for each element of volume, $\delta_{i,j,k}$, is given by:

$$\delta_{i,j,k} = \begin{cases} \dfrac{|S_{i,j,k} - \widehat{S}_{i,j,k}|}{\widehat{S}_{i,j,k}} & \text{if } \widehat{S}_{i,j,k} \neq 0 \\ 0 & \text{if } \widehat{S}_{i,j,k} = 0 \end{cases} \tag{2.20}$$

where $\widehat{S}_{i,j,k}$ is the benchmark solution obtained using a total number of rays of 1×10^9. The comparison for the cases with a total number of rays of 1×10^7, 5×10^7, 1×10^8 and 5×10^8 are presented in Table 2.2. An average deviation of 4.31% was found for the flux distribution (dimensionless) when a total number of rays of 1×10^8 is

used, which is an acceptable value to use in order to ensure that the flux distribution will not change too much with respect to the benchmark case while reducing the computation time.

Table 2.2: Average dimensionless desviation of flux distribution using different number of rays.

Total number of rays	$\overline{\delta}$
1×10^7	0.1308
5×10^7	0.0598
1×10^8	0.0431
5×10^8	0.0228

2.2.4 Model validation

In order to validate the MCRT method a comparison was done by adjusting the model parameters to those of light transport in the semi-infinite turbid medium presented in the work of Wang et al. [14] and Cui et al. [10], and comparing the results to the exact solution from the work of van de Hulst [17]. This comparison was done for a relative refractive index between the inside and outside of the semi-infinite medium equal to 1.0, absorption coefficient $\kappa = 10$ cm^{-1}, scattering coefficient $\sigma = 90$ cm^{-1}, asymmetry factor $g = 0.75$, height of the medium $h_{rec} = 0.02$ cm, 1×10^8 rays, and for three different values of the cosine of the incidence angle, $\mu_0 = 1$, $\mu_0 = 0.9$ and $\mu_0 = 0.7$. The total reflectance and transmittance was compared against the reference values as presented in Table 2.3, and the angular distribution of diffuse reflectance and transmittance as shown in Fig. 2.5 (a) and (b), respectively, for the three values of cosine of angle of incidence. It is important to refer that the unscattered transmittance is not included in the results presented in Fig. 2.5 (b), but it is included in the values of Table 2.3. The values of total unscattered transmittance for $\mu_0 = 1$, $\mu_0 = 0.9$ and $\mu_0 = 0.7$ are, respectively, 0.13480, 0.10860 and 0.05682. The results are in a good agreement with those from the work of van de Hulst [17], since the discrepancy of the total transmittance and reflectance is less than 0.41%.

Table 2.3: Comparison of the total reflectance and transmittance with the results from van de Hulst [17].

Source	Total reflectance			Total transmittance		
	$\mu_0 = 1$	$\mu_0 = 0.9$	$\mu_0 = 0.7$	$\mu_0 = 1$	$\mu_0 = 0.9$	$\mu_0 = 0.7$
van de Hulst [17]	0.09739	0.11548	0.16385	0.66096	0.62182	0.52772
This work	0.09779	0.11568	0.16352	0.66143	0.62178	0.52779

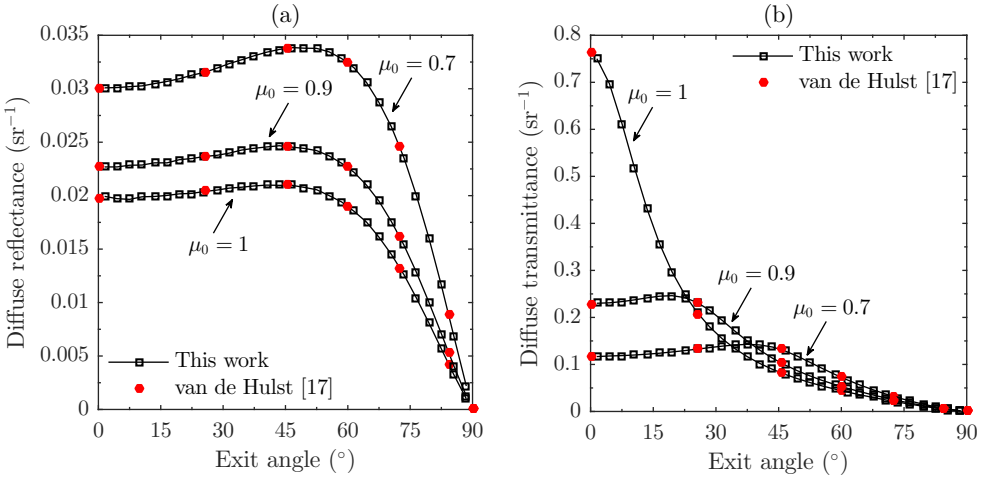

Fig. 2.5: Angular resolved representation of diffuse reflectance (a) and transmittance (b) for three different values of cosine of incidence angle.

2.2.5 Generation of the incident energy flux on the receiver

In order to test the 3D model of solar radiation absorption inside the porous volumetric receiver a parabolic dish of radius r_{dis} and focal distance f_{dis} was used to generate the incident energy flux, as shown in Fig. 2.6. The concentration of solar radiation on the inlet of the receiver is modelled using the Tonatiuh software [44], an open-source software based also in the MCRT method, considering the effect of the receiver shadow on the concentrator. The Tonatiuh output are the coordinates of the interception points of all rays in the parabolic dish and in the front aperture of the receiver. To

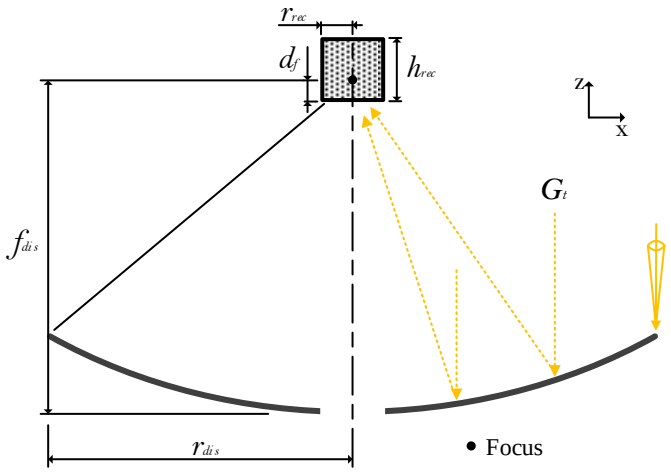

Fig. 2.6: Schematic of the parabolic dish concentration system.

design the concentration system the radius of the parabolic dish was described as a function of the concentration factor C and of the radius of the receiver r_{rec} using:

$$r_{dis} = r_{rec}(C+1)^{1/2} \tag{2.21}$$

The concentration factor is defined as the ratio between the aperture area of the parabolic dish irradiated by the sun and the area of the receiver aperture. The focal distance f_{dis} and the distance d_f are geometric parameters which can be chosen in order to improve the spatial distribution of solar radiation and incidence angle in the receiver. To compute the unit vector direction, $\hat{\mathbf{v}}_\mathbf{D}$, the coordinates of the rays in the parabolic dish and in the receiver are used:

$$\hat{\mathbf{v}}_\mathbf{D} = \frac{\mathbf{r}_{rec} - \mathbf{r}_{dis}}{|\mathbf{r}_{rec} - \mathbf{r}_{dis}|} \tag{2.22}$$

where $\mathbf{r}_{rec}$ and $\mathbf{r}_{dis}$ are, respectively, the position vector of the rays in the front surface of the receiver and in the parabolic dish. The incidence angle Θ is then computed by considering the normal unit vector $\hat{\mathbf{n}}$ at the inlet, expressed as:

$$\Theta = \cos^{-1}(\hat{\mathbf{v}}_\mathbf{D} \cdot \hat{\mathbf{n}}) \tag{2.23}$$

The spatial distribution of solar radiation flux on the receiver aperture is obtained from:

$$F_{i,j} = \frac{N^F_{i,j} p}{A_{i,j}} \tag{2.24}$$

where F is the solar radiation flux, N^F is the total number of rays and A is the area of each element i, j of the receiver aperture. For the spatial distribution of the incidence angle, an average is computed for each element of area. The efficiency of the concentration system, η_{cs}, is defined as:

$$\eta_{cs} = \frac{N^F_T}{N^I_T} \tag{2.25}$$

in which N^I_T and N^F_T are the total number of rays incident on the aperture area of the parabolic dish and receiver, respectively. By defining the efficiency of the concentration system with respect to the total number of rays incident on its aperture area, the effect of the reflectance of the concentrator, ρ, is already included in the that efficiency. The effect of the circumsolar radiation ratio (CSR) [45] is considered for clear sky conditions which corresponds to model the sun as a dish (half angle of 4.65 mrad) together with the circumsolar aureole.

The main focus of this work is to study the absorption of energy in the porous volumetric receiver using a concentration system only to generate the energy flux on its inlet. For this reason, some details of the concentration system were not included, as for example the tracking errors. The characteristics and simulation conditions of the concentration system are presented in Table 2.4. A value of 800 W m^{-2} for the incident direct normal irradiance and a CSR value of 2% are used as typical values for clear sky conditions with an air mass of 1.5 (AM1.5).

Table 2.4: Characteristics and simulation conditions of the solar concentration system.

Parameter	Value
C	500
f_{dis} (cm)	70
d_f (cm)	2.25
G_t (W m^{-2})	800
ρ	0.95
Circumsolar ratio, CSR	2%
Total number of rays	1×10^8

2.3 Results and discussion

The models for solar radiation absorption in the porous volumetric receiver and concentrator are coupled together and used for the system simulation with the parameters and conditions presented in Table 2.1 and Table 2.4. In Fig. 2.7 (a) and (b), the distribution of energy flux and incidence angle on the inlet area of the receiver are presented, respectively, with a resulting efficiency of the concentration system of 93.71%.

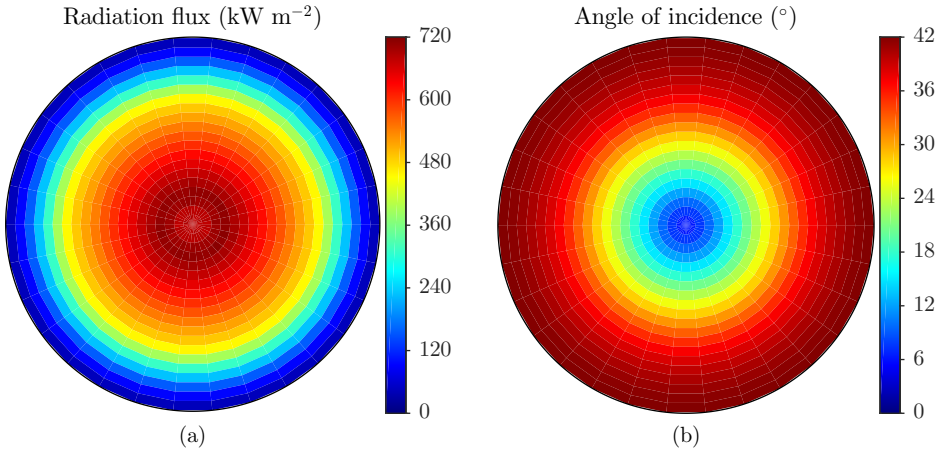

Fig. 2.7: Solar radiation flux (a) and angle of incidence (b) on the inlet area of the receiver.

The spatial distribution of the absorbed solar radiation in the porous volumetric receiver for the energy flux of Fig. 2.7 (a) and incidence angle of Fig. 2.7 (b) is shown in Fig. 2.8, for the conditions presented in Table 2.1 (these conditions result in an extinction coefficient of $\beta = 100$ m^{-1} and a scattering albedo of $\omega = 0.54$). Due to the symmetry of this problem when an ideal parabolic dish is used as concentration system, in Fig. 2.8 only the distribution for a cross section through the axial distance of the receiver is presented. A peak of absorbed energy of 156 MW m^{-3} can be observed close to the focal point of the parabolic dish, i.e, close to the depth of the

volumetric receiver, which corresponds to the distance d_f between the inlet of the receiver and the focal point. This is mainly due to the convergence of the incident solar rays and to the use of a porous receiver with a low extinction coefficient of $\beta = 100$ m^{-1}, and also due to the forward scattering factor of $g = 0.4$. The receiver wall is a barrier for the radiation propagation, making that a certain amount of energy is absorbed there, which decreases along the depth of the receiver due to the presence of less rays, as shown in Fig. 2.8.

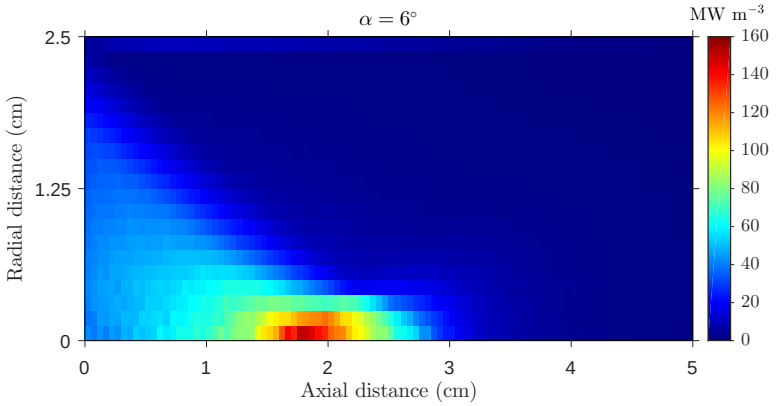

Fig. 2.8: Spatial distribution of absorbed solar radiation in the porous volumetric receiver.

Table 2.5 presents the total power absorbed in the receiver P_T, the losses of energy through the inlet L_{is} and outlet L_{os}, and the absorption efficiency η_{abs}. The fraction of energy absorbed in the wall W_f is 5.71%. These results show that the largest losses occur through the aperture of the receiver due to the backscattering of radiation.

Table 2.5: Energy losses and receiver efficiency.

Parameter	Value
P_T (W)	666.43
L_{is}	8.03%
L_{os}	1.42%
η_{abs}	90.55%

2.3.1 Study on the effect of the geometric parameters of the receiver

The internal geometry of the porous media is a crucial factor that affects the distribution of the absorbed solar radiation. In this section, the effect of the extinction coefficient and of the asymmetry factor g on the spatial distribution of solar radiation absorption is studied. The effect of the optical thickness and of the parameter g on the losses, fraction of energy absorbed in the wall and absorption efficiency, is also studied. The use of an optical thickness defined as the product of the extinction coefficient with the height of the receiver ($b = \beta h_{rec}$) is justified because it includes

the three main geometric parameters (porosity, pore diameter and height). The results presented here and in the following sections were obtained by keeping all the other parameters equal to those presented in Table 2.1 and Table 2.4.

Fig. 2.9 shows the distribution of absorbed energy using extinction coefficients of 150 m^{-1} and 300 m^{-1}. Generally, the depth up to which solar radiation propagates increases by decreasing the extinction coefficient, i.e, by increasing the porosity and pores diameter. The amount of energy absorbed in the wall depends on both the extinction coefficient and scattering albedo of the wall. If a low extinction coefficient and fixed scattering albedo of the wall is used, then there are more rays reaching the wall, which increases absorption in the wall.

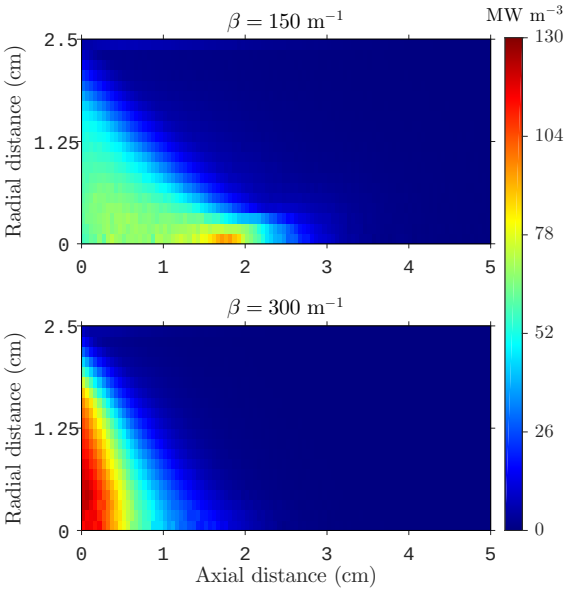

Fig. 2.9: Effect of the extinction coefficient on the distribution of solar radiation absorption.

Fig. 2.10 presents the effect of the asymmetry factor on the energy distribution for the case when materials that provide isotropic scattering ($g = 0$) and forward scattering with $g = 0.6$ are used. In a porous media with low extinction coefficient, the solar rays will have little interaction with the porous material, making the distribution less affected by the type of scattering.

Figs. 2.11, 2.12, 2.13 and 2.14 present the losses through the inlet (front) and outlet (back) of the receiver, fraction of energy absorbed in the wall and absorption efficiency, respectively, as a function of the optical thickness and asymmetry factor, for the case without scattering ($\omega_w = 0$) and with scattering ($\omega_w = 0.2$) in the wall. For a receiver with a large optical thickness, the solar rays will interact with the porous material just close to the front surface, thus contributing to the increase of energy losses through the inlet (Fig. 2.11) due to backscattering while reducing drastically the losses through the back surface (Fig. 2.12). Even with a losses increase through the front side, the absorption efficiency still increases due to the large

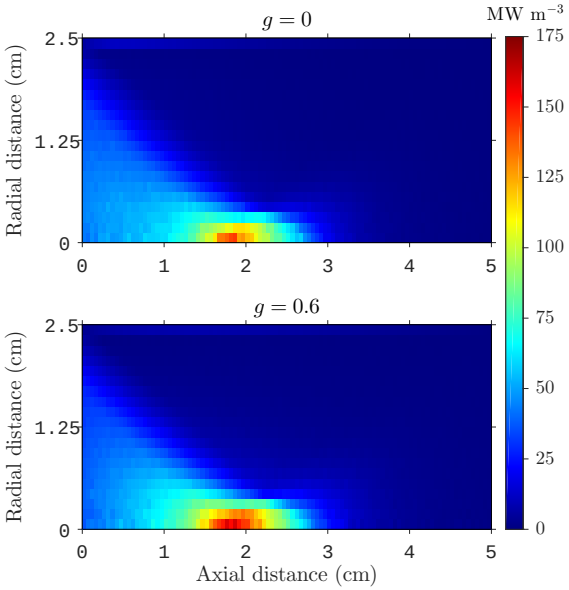

Fig. 2.10: Effect of the asymmetry factor on the distribution of solar radiation absorption.

decrease of the losses through the back side, as shown in Fig. 2.14. A larger optical thickness is obtained when using receivers with small pores and low porosities or using higher receivers. However, the optimization of the receiver should not be done without considering the distribution of absorbed energy, fluid flow and heat transfer processes (pressure losses and heat transfer characteristics of the receiver). For values of optical thickness in the range from 7.5 to 15 the absorption efficiency presents a small variation (Fig. 2.14), although the distribution of energy absorption is affected, as shown in Fig. 2.9.

The radiation scattering inside the porous material also affects mainly the losses through the inlet than through the outlet; thus to increase the absorption efficiency it is necessary to decrease the backscattering by using a porous material which provides more forward scattering (Fig. 2.11). To achieve this effect, changes on the pores geometry and optical properties of the porous material are required. Regarding the pores geometry, some porous structures are being studied [37, 42] while the optical properties of the porous material should be changed in order to promote the forward scattering of light when combined with a particular pores geometry.

For lower values of optical thickness, increasing the scattering albedo of the wall results in a increase of the losses through the front and a very small increase of the losses through the back, as shown in Figs. 2.11 and 2.12, respectively. This results in a decrease in the absorption efficiency of the receiver, as shown in Fig. 2.14. For a lower value of optical thickness, there are more rays that will interact with the wall, resulting in more energy available to be absorbed there. This absorption is lower when scattering increases, as shown in Fig. 2.13.

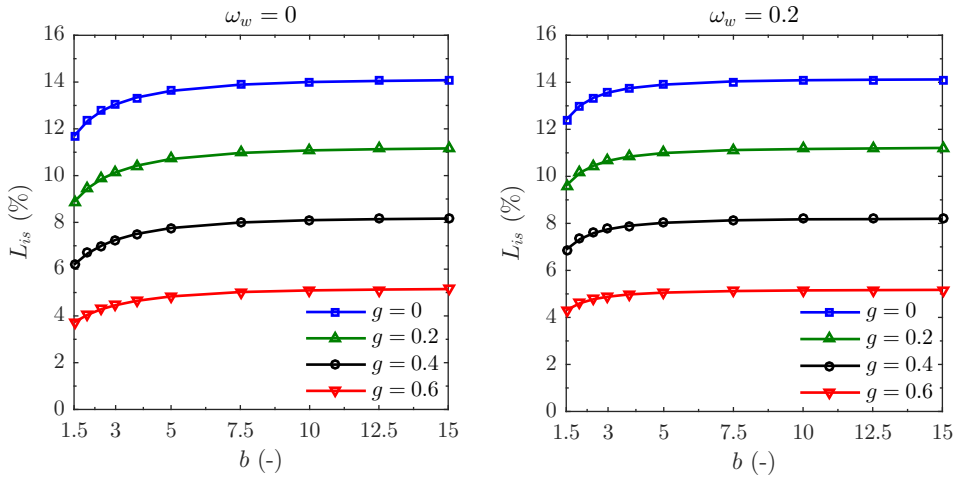

Fig. 2.11: Effect of b, g and ω_w on the losses through the front surface of the receiver.

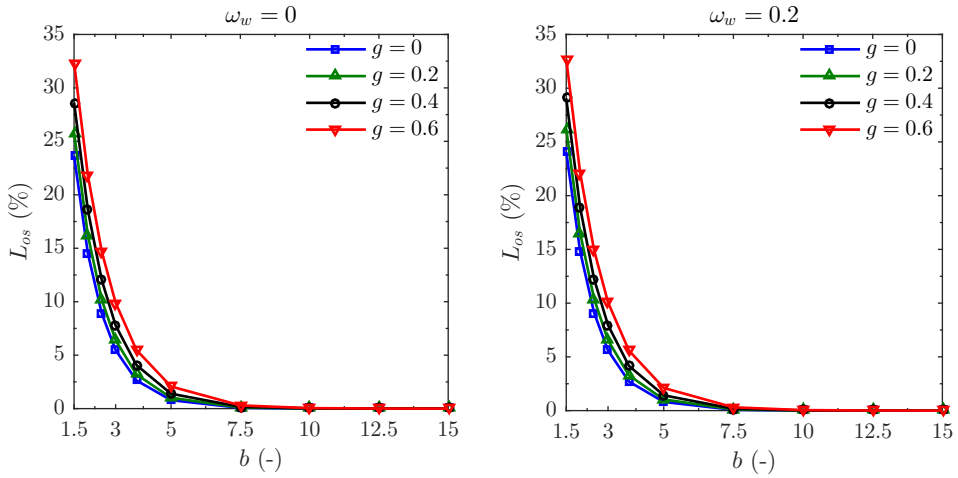

Fig. 2.12: Effect of b, g and ω_w on the losses through the back surface of the receiver.

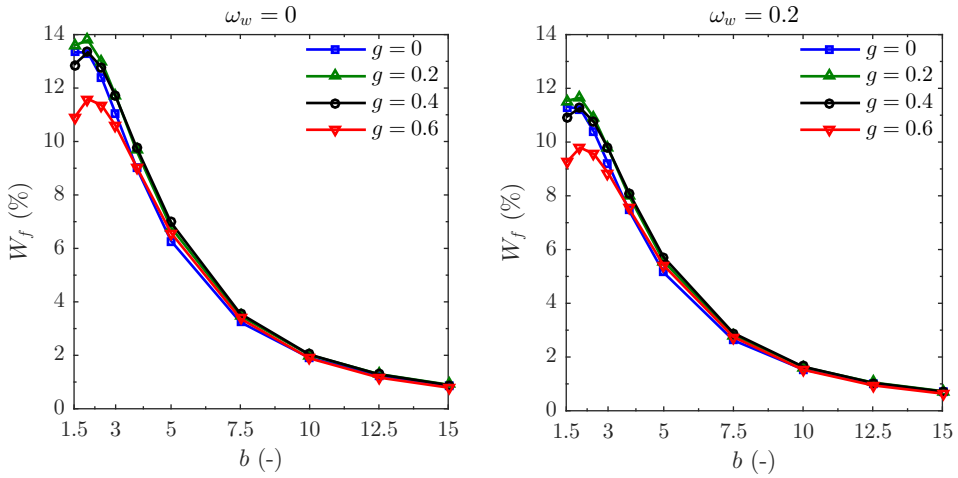

Fig. 2.13: Effect of b, g and ω_w on the fraction of energy absorbed in the receiver wall.

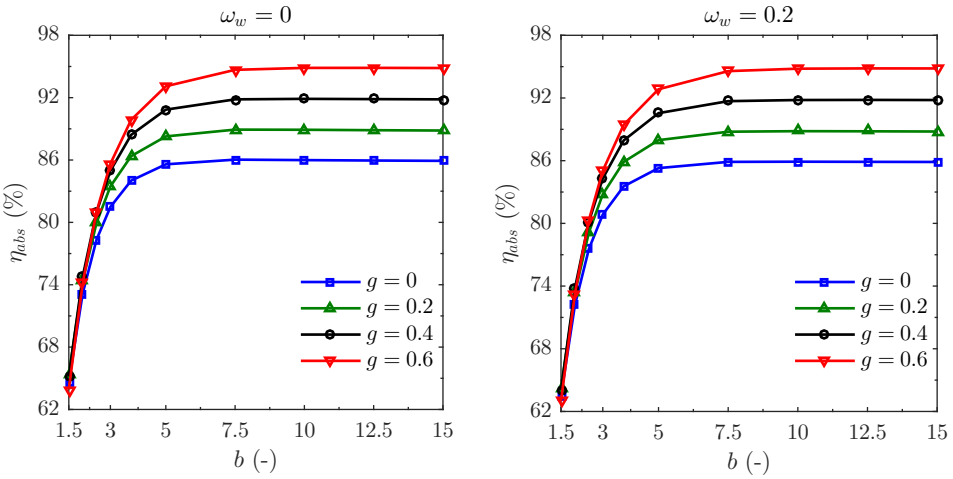

Fig. 2.14: Effect of b, g and ω_w on the efficiency of the receiver.

2.3.2 Study on the effect of convergent and divergent incidence of solar rays

To study the effect of convergent and divergent incidence of solar rays on the distribution of absorbed solar radiation, the inlet surface of the receiver is placed in two different positions, below ($d_f > 0$) and above ($d_f < 0$) the focus length, respectively (see Fig. 2.6). When the front of the receiver is placed below the focus, one has convergent incidence of the solar rays while when is placed above the incidence is divergent. Fig. 2.15 presents the distribution of absorbed energy for this two cases. In the first case, a peak flux of 353 MW m^{-3} is observed, which decreases to 86 MW m^{-3} in the second case, while the distribution is more uniform and a considerable amount of energy is absorbed in the wall. Table 2.6 presents the efficiency of the concentration system and the performance of the receiver for these two cases. As it can be seen, the difference is mainly in the amount of energy absorbed in the wall.

Table 2.6: Results for convergent and divergent incidence at the inlet surface.

d_f (cm)	η_{cs} (%)	L_{is} (%)	L_{os} (%)	W_f (%)	η_{abs} (%)	P_T (W)
1.5	94.04	8.06	1.41	5.31	90.53	668.62
-1.5	94.01	8.58	1.02	15.31	90.40	667.44

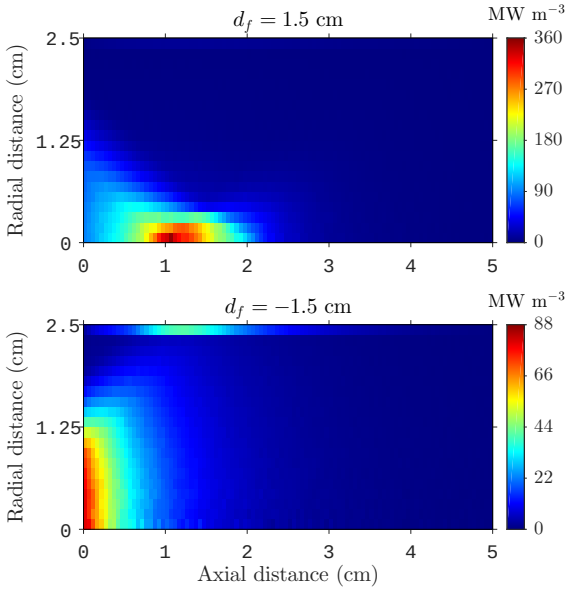

Fig. 2.15: Effect of convergent and divergent incidence on the distribution of solar radiation absorption.

2.3.3 Study on the effect of manufacturing imperfections of the parabolic dish

In addition to the deviation angle of solar rays caused by the sunshape (already considered in this work), in real applications there are also some source of optical errors, such as: slope error, tracking error, non-specular reflection and alignment error [46]. From all these optical errors, the predominant is the slope error σ_{slope} [6] which is defined as the angular deviation of normal vectors of the actual surface with respect to their ideal directions [46]. According to the work of Chen et al. [6], this deviation ranges from 1 mrad for high quality to 6 mrad for low quality optical reflectors. In order to study the effect of manufacturing imperfections, two values of slope error of 1 and 5 mrad were considered in the system simulation. The Tonatiuh software calculates the deviation of the reflector surface that is caused by a given slope error. Fig. 2.16 shows the distribution of absorbed energy for these two cases. In the first case, a peak flux of 146 MW m^{-3} is observed, which decreases to 79 MW m^{-3} in the second case. Table 2.7 presents the efficiency of the concentration system and the performance of the receiver. Higher values of slope error results in less energy available to be absorbed in the receiver and a more uniform distribution of energy without a high peak flux.

Table 2.7: Results for different slope error of the parabolic dish.

σ_{slope} (mrad)	η_{cs} (%)	L_{is} (%)	L_{os} (%)	W_f (%)	η_{abs} (%)	P_T (W)
1	93.53	8.02	1.43	5.72	90.55	665.16
5	90.08	7.99	1.43	5.94	90.58	640.80

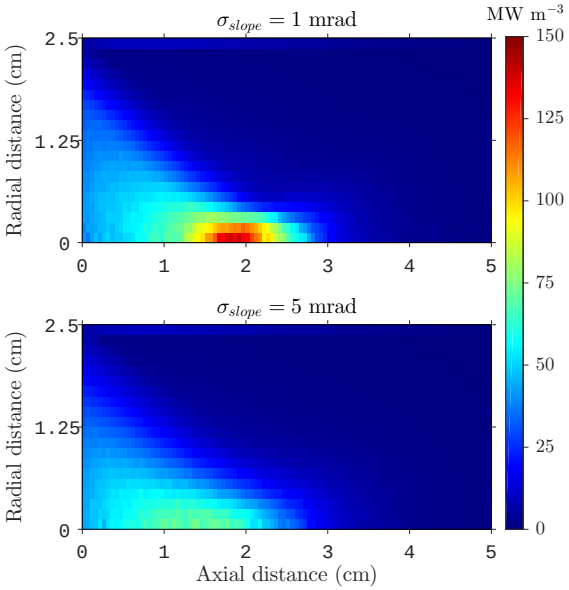

Fig. 2.16: Effect of slope error on the distribution of solar radiation absorption.

2.4 Conclusions

In this work a three-dimensional modelling and analysis of solar radiation absorption in porous volumetric receivers is developed. The model of the solar radiation propagation in porous media includes the effect of the incidence angle at the front surface (inlet) of the receiver. The Henyey-Greenstein phase function is used to model the scattering inside the porous media and the wall of the receiver is modelled as a diffuse surface. The receiver under study is cylindrical and a parabolic dish is used to generate the energy flux at the inlet of the receiver. The spatial distribution of solar energy absorbed in the porous volumetric receiver was computed and the performance of the receiver for different parameters, such as, optical thickness (porosity, pore diameter and height), asymmetry factor and the distance between the front of the receiver and the focal point is also studied. The results show that the performance of the system depends strongly on the choice of these parameters. The largest losses occur through the inlet of the receiver due to backscattering, which can be decreased by using porous structures that provide mainly forward scattering. The properties of the wall are more important when receivers with low optical thickness are used.

Whenever convergent incidence of solar rays is used, and with a receiver with low extinction coefficient, the peak flux occurs in the middle of the receiver close to a depth equal to the distance between the inlet and the focal point. For the case of divergent incidence, the peak flux decreases drastically, the distribution is more uniform and large amount of energy is absorbed in the receiver wall. The effect of the imperfections of a real reflector was also simulated, showing that higher values of slope error results in lower values of energy absorption, even without a peak flux

due to a more uniform energy distribution.

The results presented in this work are very useful to study and understand energy absorption in porous volumetric receivers when different porous structures, porosities, pore diameter, height of receiver and geometric parameters of the concentration system are used. The developed model and the results obtained allow to determine in which conditions and where the peak flux occurs, thus providing essential information on how the flow conditions and materials of the receiver should be designed and adjusted to prevent hot spots which can damage the receiver material while maximizing its efficiency. In the future, this model will be coupled to a fluid flow and thermal model and used to carry out several optimizations also taking into account different concentrator optics, as in tower type concentrators, with and without second stage concentration.

References

[1] O. Behar, A. Khellaf, and K. Mohammedi. A review of studies on central receiver solar thermal power plants. *Renew Sust Energ Rev*, 23:12–39, 2013.

[2] D. Barlev, R. Vidu, and P. Stroeve. Innovation in concentrated solar power. *Sol Energ Mat Sol C*, 95:2703–2725, 2011.

[3] C. K. Ho and B. D. Iverson. Review of high-temperature central receiver designs for concentrating solar power. *Renew Sust Energ Rev*, 29:835–846, 2014.

[4] T. Fend, R. Pitz-Paal, O. Reutter, J. Bauer, and B. Hoffschmidt. Two novel high-porosity materials as volumetric receivers for concentrated solar radiation. *Sol Energ Mat Sol C*, 84:291–304, 2004.

[5] Z. Wu, C. Caliot, G. Flamant, and Z. Wang. Coupled radiation and flow modeling in ceramic foam volumetric solar air receivers. *Sol Energy*, 85:2374–2385, 2011.

[6] X. Chen, X.-L. Xia, X.-H. Dong, and G.-L. Dai. Integrated analysis on the volumetric absorption characteristics and optical performance for a porous media receiver. *Energ Convers Manage*, 105:562–569, 2015.

[7] X. Chen, X.-L. Xia, H. Liu, Y. Li, and B. Liu. Heat transfer analysis of a volumetric solar receiver by coupling the solar radiation transport and internal heat transfer. *Energ Convers Manage*, 114:20–27, 2016.

[8] A. L. Ávila-Marín. Volumetric receivers in Solar Thermal Power Plants with Central Receiver System technology: A review. *Sol Energy*, 85:891–910, 2011.

[9] J.-F. P. P. de la Beaujardiere and H. C. R. Reuter. A review of performance modelling studies associated with open volumetric receiver CSP plant technology. *Renew Sust Energ Rev*, 82:3848–3862, 2018.

[10] F. Q. Cui, Y. L. He, Z. D. Cheng, D. Li, and Y. B. Tao. Numerical simulations of the solar transmission process for a pressurized volumetric receiver. *Energy*, 46:618–628, 2012.

[11] Y.-L. He, F.-Q. Cui, Z.-D. Cheng, Z.-Y. Li, and W.-Q. Tao. Numerical simulation of solar radiation transmission process for the solar tower power plant: From the heliostat field to the pressurized volumetric receiver. *Appl Therm Eng*, 61: 583–595, 2013.

[12] F. Wang, Y. Shuai, H. Tan, and C. Yu. Thermal performance analysis of porous media receiver with concentrated solar irradiation. *Int J Heat Mass Tran*, 62: 247–254, 2013.

[13] X. Chen, X.-L. Xia, X.-L. Meng, and X.-H. Dong. Thermal performance analysis on a volumetric solar receiver with double-layer ceramic foam. *Energ Convers Manage*, 97:282–289, 2015.

[14] L. Wang, S. L. Jacques, and L. Zheng. MCML - Monte Carlo modeling of light transport in multi-layered tissues. *Comput Meth Prog Bio*, 47:131–146, 1995.

[15] M. Atif, A. Khan, and M. Ikram. Modeling of Light Propagation in Turbid Medium Using Monte Carlo Simulation Technique. *Opt Spectrosc*, 111:107–112, 2011.

[16] A. K. Glaser, S. C. Kanick, R. Zhang, P. Arce, and B. W. Pogue. A GAMOS plug-in for GEANT4 based Monte Carlo simulation of radiation-induced light transport in biological media. *Biomed Opt Express*, 4:741–759, 2013.

[17] H. C. van de Hulst. *Multiple Light Scattering*, volume II. Academic Press, New York, 1980.

[18] M. Gao, X. Huang, P. Yang, and G. W. Kattawar. Angular distribution of diffuse reflectance from incoherent multiple scattering in turbid media. *Appl Optics*, 52:5869–5879, 2013.

[19] Y. Zhao and G. H. Tang. Monte Carlo study on extinction coefficient of silicon carbide porous media used for solar receiver. *Int J Heat Mass Tran*, 92:1061–1065, 2016.

[20] F. Gomez-Garcia, J. Gonzalez-Aguilar, S. Tamayo-Pacheco, G. Olalde, and M. Romero. Numerical analysis of radiation propagation in a multi-layer volumetric solar absorber composed of a stack of square grids. *Sol Energy*, 121: 94–102, 2015.

[21] H. Benoit, L. Spreafico, D. Gauthier, and G. Flamant. Review of heat transfer fluids in tube-receivers used in concentrating solar thermal systems: Properties and heat transfer coefficients. *Renew Sust Energ Rev*, 55:298–315, 2016.

[22] F. Bai. One dimensional thermal analysis of silicon carbide ceramic foam used for solar air receiver. *Int J Therm Sci*, 49:2400–2404, 2010.

[23] R. Capuano, T. Fend, P. Schwarzbözl, O. Smirnova, H. Stadler, B. Hoffschmidt, and R. Pitz-Paal. Numerical models of advanced ceramic absorbers for volumetric solar receivers. *Renew Sust Energ Rev*, 58:656–665, 2016.

[24] W. Fuqiang, T. Jianyu, S. Yong, T. Heping, and C. Shuangxia. Thermal performance analyses of porous media solar receiver with different irradiative transfer models. *Int J Heat Mass Tran*, 78:7–16, 2014.

[25] O. Smirnova, T. Fend, R. Capuano, G. Feckler, P. Schwarzbözl, and F. Sutter. Determination of critical thermal loads in ceramic high concentration solar receivers. *Sol Energ Mat Sol C*, 176:196–203, 2018.

[26] F. Gomez-Garcia, J. González-Aguilar, G. Olalde, and M. Romero. Thermal and hydrodynamic behavior of ceramic volumetric absorbers for central receiver solar power plants: A review. *Renew Sust Energ Rev*, 57:648–658, 2016.

[27] T. Fend, B. Hoffschmidt, R. Pitz-Paal, O. Reutter, and P. Rietbrock. Porous materials as open volumetric solar receivers: Experimental determination of thermophysical and heat transfer properties. *Energy*, 29:823–833, 2004.

[28] Z. Wu, C. Caliot, F. Bai, G. Flamant, Z. Wang, J. Zhang, and C. Tian. Experimental and numerical studies of the pressure drop in ceramic foams for volumetric solar receiver applications. *Appl Energ*, 87:504–513, 2010.

[29] C. Albanakis, D. Missirlis, N. Michailidis, K. Yakinthos, A. Goulas, H. Omar, D. Tsipas, and B. Granier. Experimental analysis of the pressure drop and heat transfer through metal foams used as volumetric receivers under concentrated solar radiation. *Exp Therm Fluid Sci*, 33:246–252, 2009.

[30] M. I. Roldán, O. Smirnova, T. Fend, J. L. Casas, and E. Zarza. Thermal analysis and design of a volumetric solar absorber depending on the porosity. *Renew Energ*, 62:116–128, 2014.

[31] B. Wang, Y. Hong, L. Wang, X. Fang, P. Wang, and Z. Xu. Development and numerical investigation of novel gradient-porous heat sinks. *Energ Convers Manage*, 106:1370–1378, 2015.

[32] Z. Wu, C. Caliot, G. Flamant, and Z. Wang. Numerical simulation of convective heat transfer between air flow and ceramic foams to optimise volumetric solar air receiver performances. *Int J Heat Mass Tran*, 54:1527–1537, 2011.

[33] S. Mey-Cloutier, C. Caliot, A. Kribus, Y. Gray, and G. Flamant. Experimental study of ceramic foams used as high temperature volumetric solar absorber. *Sol Energy*, 136:226–235, 2016.

[34] S. Guévelou, B. Rousseau, G. Domingues, J. Vicente, and C. Caliot. Representative elementary volumes required to characterize the normal spectral emittance of silicon carbide foams used as volumetric solar absorbers. *Int J Heat Mass Tran*, 93:118–129, 2016.

[35] Q. Zhu and Y. Xuan. Pore scale numerical simulation of heat transfer and flow in porous volumetric solar receivers. *Appl Therm Eng*, 120:150–159, 2017.

[36] X. Chen, X.-L. Xia, X.-W. Yan, and C. Sun. Heat transfer analysis of a volumetric solar receiver with composite porous structure. *Energ Convers Manage*, 136: 262–269, 2017.

[37] H. Xu. Performance evaluation of multi-layered porous-medium micro heat exchangers with effects of slip condition and thermal non-equilibrium. *Appl Therm Eng*, 116:516–527, 2017.

[38] F. Zaversky, L. Aldaz, M. Sánchez, A. L. Ávila-marín, M. I. Roldán, J. Fernández-Reche, A. Füssel, W. Beckert, and J. Adler. Numerical and experimental evaluation and optimization of ceramic foam as solar absorber – Single-layer vs multi-layer configurations. *Appl Energ*, 210:351–375, 2018.

[39] M. F. Modest. *Radiative Heat Transfer*. Academic Press, New York, third edition, 2013.

[40] K. Vafai. *Handbook of porous media*. Taylor and Francis, New York, second edition, 2005.

[41] M. Cagnoli, L. Savoldi, R. Zanino, and F. Zaversky. Coupled optical and CFD parametric analysis of an open volumetric air receiver of honeycomb type for central tower CSP plants. *Sol Energy*, 155:523–536, 2017.

[42] S. Cunsolo, M. Oliviero, W. M. Harris, A. Andreozzi, N. Bianco, W. K. S. Chiu, and V. Naso. Monte Carlo determination of radiative properties of metal foams:

Comparison between idealized and real cell structures. *Int J Therm Sci*, 87: 94–102, 2015.

[43] L. G. Heney and J. L. Greenstein. Diffuse radiation in the Galaxy. *Astrophys*, J. 93:70–83, 1940.

[44] M. J. Blanco, J. M. Amieva, and A. Mancillas. The tonatiuh software development project: an open source approach to the simulation of solar concentrating systems. 157–164, 2005.

[45] D. Buie, A. G. Monger, and C. J. Dey. Sunshape distributions for terrestrial solar simulations. *Sol Energy*, 74:113–122, 2003.

[46] D. Buie, C. J. Dey, and S. Bosi. The effective size of the solar cone for solar concentrating systems. *Sol Energy*, 74:417–427, 2003.

Nomenclature

A	area (m^2)
$\mathbf{a}$	arbitrary vector (-)
b	optical thickness (-)
C	concentration factor (-)
d_f	distance between the front of the receiver and focal point (m)
d_p	pores diameter (m)
F	radiation flux at receiver front face (W m^{-2})
f	focus length (m) or fraction (-)
G_t	direct normal irradiance (W m^{-2})
g	asymmetry factor (-)
h	height (m)
L	fraction of energy lost (-)
l_β	path length of rays (m)
N	number of rays (-)
N_v	number of volume elements (cells) (-)

$\hat{\mathbf{n}}$	normal unit vector (-)
P	energy absorption in the volumetric receiver (W)
p	power per ray (W) or phase function (-)
r	radius (m)
$\mathbf{r}$	position vector (m)
S	energy absorption per unit of volume (W m^{-3})
$(\hat{\mathbf{s}}, \hat{\mathbf{v}}_{\mathbf{D}})$	unit vector direction (-)
V	volume (m^3)
W_f	fraction of energy absorbed in the wall (-)

Greek symbols

α	azimuthal angle of cylindrical coordinates system (rad)
β	extinction coefficient (m^{-1})
δ	difference
ε	emissivity (-)
η	efficiency (-)
Θ	angle of incidence (rad)
θ	polar angle (rad)
κ_a	absorption coefficient (m^{-1})
κ_s	scattering coefficient (m^{-1})
ξ	random number uniformly distributed between 0 and 1 (-)
ρ	reflectance of the parabolic dish (-)
ϕ	porosity (-)
ψ	azimuthal angle (rad)
ω	scattering albedo (-)

Subscripts

abs	absorption
cs	concentration system
dis	parabolic dish

i, j, k	indices of the volume elements (cells)
is	front face (inlet) of the receiver
os	back face (outlet) of the receiver
rec	volumetric receiver
T	total
w	receiver wall
1	initial position
2	final position

Superscripts

I	aperture area of the parabolic dish
is	front face (inlet) of the receiver
F	front face area of the volumetric receiver
os	back face (outlet) of the receiver
S	inside the receiver volume
w	receiver wall

Chapter 3

Three-dimensional CFD modelling and thermal performance analysis of porous volumetric receivers coupled to solar concentration systems[†]

Abstract

Porous volumetric receivers is a promising technology to improve the thermal performance of a new generation of concentrated solar power (CSP) plants. In this sense, this work addresses the Computational Fluid Dynamics (CFD) modelling and thermal performance analysis of porous volumetric receivers coupled to solar concentration systems. A cylindrical receiver element made of open-cell SiC ceramic foam was considered. The fluid flow and heat transfer processes in the porous media are modelled through volume averaged mass, momentum and energy conservation equations, considering the local thermal non-equilibrium (LTNE) approach, while the thermal radiation transfer is described by the P1 spherical harmonics method, using an open source software (OpenFOAM). An in-house algorithm based on the Monte Carlo Ray Tracing (MCRT) method was developed and coupled to the CFD mesh to model the propagation and absorption of solar radiation. The modelling of the receiver boundary conditions were improved, and a detailed analysis of a reference configuration of the receiver was conducted using a parabolic dish with a concentration ratio of 500 to generate the concentrated solar radiation field and a receiver element with diameter 5 cm, height 5 cm, pore size 3 mm and porosity 0.9. The thermal power output, thermal efficiency, mean fluid temperature at the outlet and pressure drop of this reference configuration are 628.92 W, 85.46%, 474.22 K and 103.10 Pa,

[†]Germilly Barreto[(1)], P. Canhoto[(1)], and M. Collares-Pereira[(1)]. Three-dimensional CFD modelling and thermal performance analysis of porous volumetric receivers coupled to solar concentration systems. *Applied Energy*, 252:113433, 2019.

[(1)] Institute of Earth Sciences, University of Évora.

respectively. The use of receivers with high porosity and pores size increases the thermal efficiency slightly and decreases the pressure drop substantially. The convergent incidence of solar rays on the inlet of the receiver leads to high peaks of temperature on the porous structure and fluid, and a way to decrease these peaks is to design the concentration system or place the receiver in such way to obtain lower incidence angles at the inlet.

Keywords: Porous volumetric receiver; Solar concentration; Fluid flow; Heat transfer; Radiative transfer.

3.1 Introduction

Over the last few years, increasing attention has been given to the use of porous structures as thermal receivers (porous volumetric receivers) in high-temperature concentrated solar power (CSP) plants technology [1]. This increased interest is mainly due to the capabilities of these type of receivers to achieve high temperatures and thermal efficiencies [1]. In this receivers air is usually used as the heat transfer fluid in open systems [2, 3], but other gases can be used in pressurized closed systems, as in the promising generation of CSP plants that use Brayton cycles with CO_2 at supercritical conditions [4].

The work of Ávila-Marín [5] presents a detailed description of the porous volumetric receivers and their main configurations, as well, the most commonly materials that are being used for their fabrication. The materials may be metal or ceramic [5], but ceramic materials are the best alternative because of their resistance to oxidising atmospheres, high melting point, low thermal expansion and high thermal shock resistance, which make them more suitable for high-temperature applications [5, 6]. The silicon carbide (SiC) foam, which is utilised in many industrial applications [6], is one of the most used ceramic materials, due to its good radiative and thermal properties [7]. There are two main configurations of porous structures of SiC ceramic foam, which are honeycomb and open-cell structures [7]. The honeycomb structures comprise parallel channels (usually with square cross-section) oriented in the fluid flow direction and arranged in a hexagonal shape [7], while the open-cell structures are formed by randomly packed open cells, which can have different sizes and shapes [7]. Most of the works on porous volumetric receivers available in the literature address the numerical and experimental investigation of these two structures, being the open-cell SiC ceramic foam the most addressed.

Significant advances are being made in the study of solar radiation propagation and absorption in porous media coupled to the fluid flow and heat transfer processes [7, 8], aiming at its application in CSP plants. There are two main approaches to model numerically these processes [9, 10]: the first one is the pore-scale approach [11], where the structure is modelled (explicitly using a detailed description of the

geometry of the pores); and the second one is continuous-scale approach [12], based on considering the porous media as a continuous semitransparent medium, and using the volume averaged concept of variables for the solid matrix structure (called solid phase) and heat transfer fluid (called fluid phase). In the pore-scale approach, the complexity of the pore geometry in the structure must be fully described, while in continuous-scale approach this complexity is not described in such detail [9]. In the field of solar thermal applications of porous volumetric receivers, research focuses mainly on what happen in a macroscopic scale, not in pore-scale, which makes the continuous-scale approach very suitable and the most used [13, 14], since it also requires much less computational effort in comparison to pore-scale approach.

The study of porous volumetric receivers can be divided into two parts [15]: the first one is the absorption of solar radiation in the porous structure [16, 17] and the second is the coupling of the solar radiation absorption with the fluid flow and heat transfer processes including the thermal radiation exchange in order to obtain its thermal performance [18, 19]. This coupling can be done using two different approaches: (i) modelling the solar radiation absorption separately, usually using the MCRT method [15], and then including it together with the net thermal radiation exchange as a heat source of the energy conservation equation [18]; or (ii) modelling the solar radiation absorption together with the thermal radiation by solving the broadband radiative transfer equation [20].

The transport and absorption of radiation in porous media is a complex problem [21], but its modelling is crucial for the study of the thermal performance of porous volumetric receivers. For this purpose, several works are being developed in order to describe in detail the geometry of porous structure and their optical and radiative properties [22, 23]. Li et al. [24] conducted a detailed analysis of radiative properties of irregular open-cell foams. They found that the extinction coefficient depends on the porosity, mean pores size and on the cross-section shape of the ligament of the porous structure, while the scattering albedo depends on the radiative properties and the shape of the porous structure. In the recent works of Xia et al. [25] and Li et al. [26], besides the two commonly used modelling approaches, they proposed a new method that consists in combining the continuous-scale approach with the exact description of the porous structure into a single computational domain, which they called scale-coupled approach. They assessed the performance of this method and found that it can be used to unite the advantages of the continuous-scale (less computational effort) and pore-scale (accurate prediction of local radiative quantities) approaches.

For the heat transfer modelling, Xu et al. [27] compared different numerical and analytical solutions to predict the thermal performance of porous volumetric collectors, and the pros and cons of each one are discussed. Regarding the heat

transfer between the solid and fluid phases, two different approximations can be used when the continuous-scale approach is considered [10, 12]. The first is the local thermal equilibrium (LTE), in which the temperatures of the solid and fluid phases are assumed to be the same, and thus only one energy equation is needed for modelling. The second is the local thermal non-equilibrium (LTNE), in which the temperature of the two phases are considered to be different, and thus two energy equations are needed, one for the solid and other for the fluid. In the LTNE approach, the heat transfer (convection) between the solid and fluid phases must be described, which makes it the most accurate approximation when significant differences of temperature between the two phases are expected. In this regard, several studies exist that aim to describe the convective heat transfer between the solid and fluid [28, 29]. For example, Wu et al. [30] developed a correlation for the local volumetric convective heat transfer coefficient between air and ceramic foams by modelling an idealised packed tetrakaidecahedron structure that represents the porous structure. In the work of Ávila-Marín et al. [31], a similar study was carried out, but considering porous materials made of metallic plain-weave wire meshes. Xia et al. [32] carried out an experimental study of the convective heat transfer coefficient in different foam structures, including SiC, and a new correlation was proposed. Also in the continuous-scale approach, the fluid flow through the porous structure is modelled by including a source term in the momentum conservation equation that represents the effect of the porous media [12]. This momentum source term depends on the geometry of the porous material and fluid flow conditions. In this regard, various studies report the pressure drop across the porous media as a function of these parameters [33, 34]. For example, Wu et al. [34] developed an empirical model that predicts the pressure drop in ceramic foams as a function of porosity, pores size and fluid flow conditions based on experimental results and a parametric numerical simulation of an idealised packed tetrakaidecahedron structure. Development of new correlations for the convective heat transfer coefficient and pressure drop in porous media still be object of interest, as for example, in the recent works of Nie et al. [33] and Kim and Kim [35], where more correlations based on numerical and experimental studies are proposed.

Thermal receiver models are also often used for its optimisation, and several works were developed to find ways to improve both thermal and hydrodynamic performances [36, 37]. Accordingly, studies on the optimisation of temperature distribution in the solid matrix are being made to avoid the occurrence of hot spots, which can damage the receiver materials during its life cycle. The recent work of Nimvari et al. [38] presents a new approach based on a non-uniform distribution of the air velocity at the inlet of the receiver to mitigates this problem. They compared the results with those for a uniform velocity distribution at the inlet and found that the new

approach can reduce the very high temperature spots in the solid. Other techniques to improve the distribution of temperature are designing receivers with gradually-varied porosity (porosity decreases gradually from the front surface to the rear surface) [39], and receivers constituted by different configurations of porous structures (composite porous structure) [40]. For example, the work of Chen et al. [40] presents a comparison of the temperature distribution in receivers with single and composite structures. They found that the composite structure reduces the temperature gradient in the solid matrix of the receiver. Multi-layer porous structures are being also proposed as a way to improve thermal performance, as it can be found in the recent works of Zaversky et al. [36], Zhu and Xuan [41] and Xu [42], where single, double, triple and more layers configurations were investigated.

In this work, a detailed three-dimensional modelling and thermal performance analysis of a porous volumetric receiver element made of open-cell SiC ceramic foam is presented. The fluid flow and heat transfer processes are modelled through volume averaged mass, momentum and energy conservation equations using the continuous-scale and LTNE approaches, while the thermal radiation transfer is described by the P1 spherical harmonics method, using an open source software (OpenFOAM). An in-house algorithm based on the MCRT method was developed and coupled to the Computational Fluid Dynamics (CFD) mesh to model the propagation and absorption of solar radiation, which is included as a source term in the energy conservation equation for the solid phase. A parabolic dish is used to generate the concentrated solar radiation flux at the receiver inlet.

A detailed study of the effect of geometric parameters of the porous structure (porosity and pores size) and different configurations of the concentration system on the temperature distribution in the solid and fluid phases, thermal efficiency and pressure drop across the receiver is presented. Another important contribution of this work is the prediction of the detailed location of hot spots in the solid and fluid phases when the different configurations or operation conditions are used, and then the discussion on the solutions to improve the thermal performance of the receiver. The modelling of the receiver boundary conditions were also improved, namely by considering different approaches for the adiabatic side wall and by accounting for the thermal radiation exchange with the surrounding medium both in the inlet and outlet planes. In that sense, this work also presents a detailed study on the effect of using different assumptions to describe the temperature profiles of the solid and fluid phases near a wall with prescribed heat flux and exchanging heat one to another. The numerical model and the results presented in this work are essential for improving the thermal and hydrodynamic performance of porous volumetric receivers coupled to concentration systems in CSP plants.

3.2 Porous volumetric receivers coupled to solar concentration systems

In this work, the thermal performance of porous volumetric receivers coupled to solar concentration systems is studied numerically, considering the following phenomena: concentration of solar radiation; propagation and absorption of the concentrated solar radiation in the porous structure; flow of the heat transfer fluid through the porous structure and heat transfer between the solid matrix structure and the fluid, including the thermal radiation exchange. Fig. 3.1 shows these phenomena schematically for the case of an open system with a cylindrical receiver element with height L and radius r_{rec}. A concentration system concentrates the solar radiation towards the inlet of the receiver, and then this radiation is absorbed along the volume of the receiver, which increases the temperature of the solid matrix. A heat transfer fluid is forced to flow through the porous media to collect this thermal energy. The complexity of modelling this kind of system is very high and, due to this, the following simplifications are assumed in this work: the porous media is homogeneous and isotropic; the pores are considered spherical; the radiative properties of the porous media (absorption and scattering coefficients and the emissivity) do not depend on the wavelength, the heat transfer fluid is considered to be a non-participating media of radiation exchange, and the natural convection is neglected due to the imposed forced convection (pressure forces dominate over the buoyancy forces). In addition, the thermal expansion of the solid matrix structure is neglected due to the low thermal expansion coefficient of the materials used in these type of receivers [6].

The absorbed solar radiation in the porous media is the source of energy for the heat transfer process. Once having the spatial distribution of absorbed solar radiation, the thermal performance of the receiver is modelled considering the mass, momentum and energy conservation equations and the P1 spherical harmonics method for describing the thermal radiation transport. This work is organized in such way that it focuses mainly in the fluid flow and heat transfer processes, while concentration of solar radiation in the inlet and its propagation and absorption are summarized in Section 3.2.4. Details on the propagation and absorption processes modelling in the porous receiver can be found in the recent work by Barreto et al. [15].

In this work, the porous media is modelled considering the continuous-scale approach, where the porous media is assimilated to a continuous semi-transparent medium [12], and the terminologies solid and fluid phases are used to refer to the solid matrix structure and the heat transfer fluid, respectively. Based on this approach, the macroscopic three-dimensional governing equations for steady state conditions are solved.

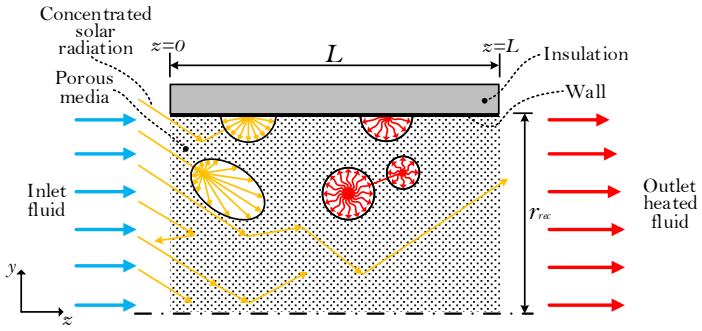

Fig. 3.1: Fluid flow and heat transfer processes in porous volumetric receiver.

3.2.1 Fluid flow modelling

According to the work of Vafai [12], for steady state conditions, the macroscopic continuity and momentum equations based on the three-dimensional superficial velocity vector $\vec{U}$ are given by Eqs. (3.1) and (3.2), respectively. The superficial velocity $\vec{U}$ with components U_x, U_y and U_z is related with the average pores velocity $\vec{u}$ through $\vec{U} = \phi\vec{u}$, in which ϕ is the porosity. In the following, the mass and momentum conservation equations are presented.

Continuity equation:

$$\nabla \cdot (\rho_f \vec{U}) = 0 \tag{3.1}$$

Momentum equation:

$$\frac{1}{\phi}\nabla\left(\rho_f \frac{\vec{U}\cdot\vec{U}}{\phi}\right) = -\nabla p + \nabla\cdot\left(\frac{\mu_f}{\phi}\nabla\vec{U}\right) + \vec{M}_s \tag{3.2}$$

in which ρ_f is the fluid density, p is pressure, μ_f is the dynamic viscosity and $\vec{M}_s$ is the momentum source due to the presence of the porous media. For the momentum source, in this work the following correlation is used [34]:

$$\vec{M}_s = -\frac{1039 - 1002\phi}{d_p^2}\mu_f\vec{U} - \frac{0.5138\phi^{-5.739}}{d_p}\rho_f|\vec{U}|\vec{U} \tag{3.3}$$

where d_p is the diameter of the pores and $|\vec{U}|$ is the magnitude of the superficial velocity. Many other models can be used to predict the pressure drop in ceramic foams [34]. However, according to the work of Wu et al. [34], this correlation presents good agreement with experimental data and it is more accurate than the other models, which is making it to be extensively used by many authors [14, 38]. The correlation is valid for a cross section of the pores that approaches to circle, $0.66 < \phi < 0.93$ and for $10 < \mathrm{Re} < 400$, where Re is the Reynolds number based on the diameter of the pores d_p and superficial velocity [34]:

$$\mathrm{Re} = \frac{\rho_f|\vec{U}|d_p}{\mu_f} \tag{3.4}$$

The heat transfer fluid, which in this work is considered to be air, is treated as an ideal gas, and its density is computed using the equation of state:

$$\rho_f = \frac{p}{RT_f} \tag{3.5}$$

where R is the gas constant ($R = 287$ J kg^{-1} K^{-1} [43]) and T_f is the fluid temperature obtained from the energy equations presented in Section 3.2.2. The dynamic viscosity is computed using the Sutherland's law [44], which is described as:

$$\mu_f = \mu_{ref}\left(\frac{T_f}{T_{ref}}\right)^{3/2}\frac{T_{ref} + S_f}{T_f + S_f} \tag{3.6}$$

in which T_{ref} is a reference temperature, μ_{ref} is the dynamic viscosity for T_{ref} and S_f is the Sutherland temperature. For air, it is used $T_{ref} = 273.15$ K, $\mu_{ref} = 1.716 \times 10^{-5}$ kg m^{-1} s^{-1} and $S_f = 110.4$ K [43].

3.2.2 Heat transfer modelling

The macroscopic energy equations for the local thermal non-equilibrium (LTNE) condition of the fluid and solid phases are [12]:

$$\nabla \cdot (\rho_f c_p \vec{U} T_f) = \nabla \cdot (\lambda_{fe} \nabla T_f) + h_v(T_s - T_f) \tag{3.7}$$

$$0 = \nabla \cdot (\lambda_{se} \nabla T_s) + h_v(T_f - T_s) + Q_{ir} + Q_{solar} \tag{3.8}$$

respectively, where c_p is the specific heat capacity of the fluid, λ_{fe} and λ_{se} are the effective thermal conductivity of the fluid and solid, respectively, h_v is the volumetric heat transfer coefficient, T_s is temperature of the solid phase, Q_{ir} is the radiative source term due to the thermal radiation exchanged inside the porous structure and Q_{solar} is the source term due to the absorbed solar radiation. The volumetric convective heat transfer coefficient, h_v, is computed using the correlation obtained by Wu et al. [30]:

$$\begin{aligned}\mathrm{Nu} = \frac{h_v d_p^2}{\lambda_f} = \big(&32.504\phi^{0.38} - 109.94\phi^{1.38} + 166.65\phi^{2.38} \\ &- 86.98\phi^{3.38}\big)\mathrm{Re}^{0.438}\end{aligned} \tag{3.9}$$

where Nu is the Nusselt number based on h_v, λ_f is the thermal conductivity of the fluid and the characteristic length d_p is the pore diameter. According to Wu et al. [30], this correlation agrees well with the experimental data from the work of Younis and Viskanta [28] and it is valid for $0.66 < \phi < 0.93$ and $70 < \mathrm{Re} < 800$. It predicts well the Nusselt number for a superficial velocity of 2.2 m s^{-1}, but it overestimates it for $|\vec{U}| < 2.2$ m s^{-1} and underestimates for $|\vec{U}| > 2.2$ m s^{-1}. This correlation is being used extensively in many others works [14, 38].

The effective thermal conductivity for the fluid, λ_{fe}, and solid phases, λ_{se}, are defined using the Schuetz and Glicksman model [45, 46] in the form:

$$\lambda_{fe} = \phi\lambda_f \tag{3.10}$$

$$\lambda_{se} = \frac{1}{3}(1-\phi)\lambda_s \tag{3.11}$$

respectively. According to the work of Kamiuto [46], this model is more accurate among the formula examined. The thermal conductivity, λ_f, and the specific heat capacity, c_p, of the fluid are defined as function of temperature by using correlations from the work of Wu et al. [20] in the form of polynomial curve fits to data for a temperature range reported in 100 to 1600 K from the work of Mulholland [47]:

$$\begin{aligned}\lambda_f = {} & 1.52\times10^{-11}T_f^3 - 4.86\times10^{-8}T_f^2 + 1.02\times10^{-4}T_f \\ & - 3.93\times10^{-3}\end{aligned} \tag{3.12}$$

$$\begin{aligned}c_p = {} & 1.93\times10^{-10}T_f^4 - 8\times10^{-7}T_f^3 + 1.14\times10^{-3}T_f^2 \\ & - 4.49\times10^{-1}T_f + 1.06\times10^{3}\end{aligned} \tag{3.13}$$

The thermal conductivity of the solid phase, λ_s, is considered to be constant and its value is given in Section 3.3.2.

3.2.3 Thermal radiation modelling

To compute the thermal radiation source term Q_{ir} in Eq. (3.8), it is necessary to solve the radiative transfer equation (RTE) [48]. In this work, the P1 approximation of the spherical harmonics method [48] is used, in the following form:

$$-\nabla\cdot\left(\frac{1}{3\beta}\nabla G\right) = \kappa_a\left(4\sigma T_s^4 - G\right) \tag{3.14}$$

in which G is the incident thermal irradiation (irradiance) in W m^{-2}, β is the extinction coefficient, κ_a is the absorption coefficient of the porous media and σ is the Stefan Boltzmann constant. The extinction coefficient β is defined as:

$$\beta = \kappa_a + \kappa_s \tag{3.15}$$

where κ_s is scattering coefficient. According to geometric optics approximations [49], κ_a and κ_s can be defined respectively as [12]:

$$\kappa_a = 1.5\varepsilon(1-\phi)/d_p \tag{3.16}$$

$$\kappa_s = 1.5(2-\varepsilon)(1-\phi)/d_p \tag{3.17}$$

where ε is the emissivity of the porous media solid material. Then, the thermal radiation source Q_{ir} is obtained through [48]:

$$Q_{ir} = -\kappa_a\big(4\sigma T_s^4 - G\big) \tag{3.18}$$

The emissivity of the solid material, ε, is considered to be constant and its value is given in Section 3.3.2. According to geometric optics approximations, the estimation of the absorption and scattering coefficients using Eqs. 3.16 and 3.17 can be considered a good approximation when the size of the ligament (bridges) of the porous structure, with which light interacts, is much larger than the wavelength of the incident radiation [49]. According to the work of Cunsolo et al. [50], the smallest ligament size is around 100 μm for foam structures, which allows this approach to be suitable for the visible and the higher energy infrared spectrum.

3.2.4 Modelling of solar radiation concentration, propagation and absorption in the porous media

In order to obtain the absorbed solar radiation Q_{solar}, which is the source term in the energy conservation equation (Eq. (3.8)), the in-house Monte Carlo Ray Tracing (MCRT) method developed in a previous work by Barreto et al. [15] is employed using as input the results from the ray tracing software Tonatiuh (2.2.2) [51]. This software, which also use MCRT method, was used to model the concentrated solar radiation flux at the inlet of the receiver, and then the in-house MCRT method was used to compute the propagation and absorption of solar radiation inside the receiver. In a general way, the MCRT method consists in splitting the solar irradiance into a high number of small equal amount of energy, called rays, and then compute the path of each one until they are absorbed (final position) or leave the system. In this work, an open porous volumetric receiver (without glass window) is considered and it is assumed that the radiation only propagates in the transparent working fluid (air). For this reason, it is considered that the refractive index of the porous media is equal to that of air, which means that there is no refractive-index mismatched between the porous media and environment. Then, when the rays from the concentration system hit the front surface of the receiver, they directly enter into the receiver without reflection and absorption [15, 16]. To compute the path l_β of each ray inside the receiver, the following expression is used [15, 48]:

$$l_\beta = -\frac{1}{\beta}\ln\xi \tag{3.19}$$

in which ξ is a random number between 0 and 1. To decide if the ray is absorbed or scattered another random number ξ is generated, and the following conditions are used:

$\xi \leqslant \omega$, scattering

$\xi > \omega$, absorption

in which $\omega = \kappa_s/\beta$ is the scattering albedo of the porous media. If scattering occurs, the Henyey-Greenstein phase function [52], which gives the probability of a given scattering angle, is used to compute the new direction of the ray:

$$\Phi(\theta) = \frac{1}{4\pi} \frac{1 - g^2}{(1 + g^2 - 2g\cos\theta)^{3/2}} \tag{3.20}$$

where Φ is the phase function, θ is the polar scattering angle and g is the asymmetry factor that can assume values between -1 (full backscattering) and 1 (full forward scattering), with 0 standing for uniform scattering. The side wall is treated as a perfect diffuse reflector with albedo ω_w, with the reflection angle also determined through a random number.

Once having the final positions of all the absorbed rays (for more details about the MCRT method, see ref. [15], which focuses only on this part), a statistical analysis is needed to obtain the spatial distribution of absorbed solar radiation:

$$Q_{solar} = \frac{N_{ev} e}{V_{ev}} \tag{3.21}$$

where V_{ev} and N_{ev} are, respectively, the volume and the number of rays absorbed in each small element of volume used in the meshing process described in Section 3.3.1, and e ($e = 7.854 \times 10^{-6}$ W) is the power per ray defined as the product between the aperture area of the concentration system and the direct normal irradiance (DNI) and then divided by the total number of rays used in the MCRT method, which are given in Section 3.3.2.

In this work, the concentrated solar radiation field is generated through a parabolic dish with the configuration shown in Fig. 2.6, used here mainly for the development and validation of the global thermal model of the receiver. Once validated, this global model can be used with other concentration systems, such as tower type concentrators [53], provided that the incident radiation is previously obtained via the Tonatiuh software, for example. The size of the parabolic dish is calculated as function of the concentration factor, using the following relation [15]:

$$r_{dis} = r_{rec}(C + 1)^{1/2} \tag{3.22}$$

where r_{dis} and r_{rec} are the radius of the parabolic dish and receiver respectively, and C is the concentration factor defined as the ratio between the aperture area of the parabolic dish irradiated by the sun and the area of the receiver aperture [15].

The main focus of this work is to investigate the thermal and hydrodynamic performances of the porous volumetric receiver. For this reason, some details of the

concentration system were not included, such as the tracking, slope, non-specular reflection and alignment errors.

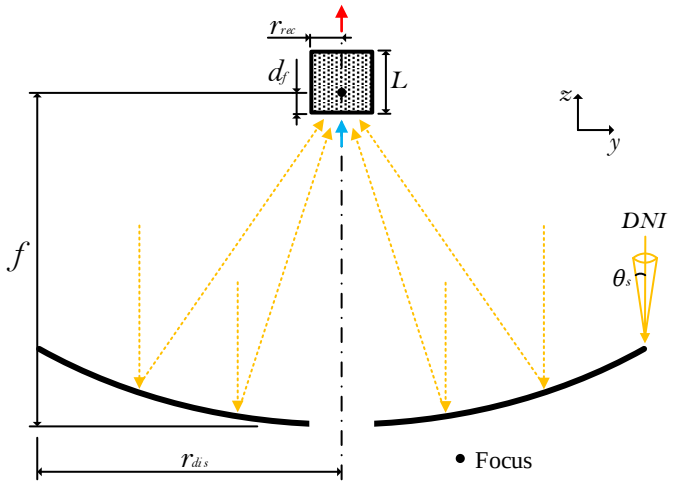

Fig. 3.2: Schematic of the concentration system.

3.2.5 Boundary conditions

Solving Eqs. (3.1), (3.2), (3.7), (3.8) and (3.14) requires setting appropriate boundary conditions. As shown in Fig. 3.1, there are three boundary patch: inlet ($z = 0$), outlet ($z = L$) and the side wall. For these boundaries, the conditions for the superficial velocity $\vec{U}$, pressure p, temperature of the fluid T_f, temperature of the solid T_s and thermal radiation exchange with the surrounding must be defined. Accordingly, the following conditions are used:

- Inlet ($z = 0$):
  At the inlet, in addition to the assumptions described in Section 3.2.4, one considers that there are no convective and conduction heat losses from the solid and fluid to the environment (the fluid is forced to enter into the receiver), the pressure gradient is zero, and the velocity and temperature of the fluid are specified:

$$\vec{U} = \vec{U}_{in}$$
$$\vec{n} \cdot \nabla p = 0$$
$$T_f = T_{in}$$
$$(1-\phi)\lambda_s(\vec{n} \cdot \nabla T_s) + (1-\phi)\varepsilon\sigma(T_s^4 - T_{in}^4) = 0$$

  where $\vec{U}_{in}$ and T_{in} are given values of superficial velocity and temperature of the fluid at the inlet (uniform values), respectively, $\vec{n}$ is the normal unit vector to inlet surface and pointing out the receiver and T_s is the temperature of the solid. For the

thermal radiation exchange, the Marshak boundary condition [48] is used assuming the emissivity of the surroundings equal to 1.0:

$$\frac{1}{2}\big(4\sigma T_{in}^4 - G\big) = \frac{1}{3\beta}\vec{n}\cdot\nabla G \tag{3.23}$$

It should be noted that the temperature of the surroundings and the fluid at inlet are considered to be the same (T_{in}).

- Outlet ($z = L$):
  At the outlet, fully developed conditions for the fluid temperature and velocity are considered, and the value of the pressure is specified:

  $$\vec{n}\cdot\nabla(\vec{U}\cdot\vec{n}) = 0$$
  $$p = p_{out}$$
  $$\vec{n}\cdot\nabla T_f = 0$$
  $$(1-\phi)\lambda_s(\vec{n}\cdot\nabla T_s) + (1-\phi)\varepsilon\sigma(T_s^4 - \overline{T}_f^4) = 0$$

  where p_{out} is a given value of pressure (uniform value), T_s is the temperature of the solid and $\overline{T}_f$ is the mean temperature of the fluid at the outlet. For the thermal radiation exchange, the same Marshak boundary condition used at inlet is considered with the temperature $\overline{T}_f$:

  $$\frac{1}{2}\big(4\sigma\overline{T}_f^4 - G\big) = \frac{1}{3\beta}\vec{n}\cdot\nabla G \tag{3.24}$$

- Wall:
  The side wall of the receiver is considered to be adiabatic and the no-slip condition of the fluid is used:

  $$\vec{U} = \vec{0}$$
  $$\vec{n}\cdot\nabla p = 0$$
  $$T_f = T_s$$
  $$(1-\phi)\lambda_s(\vec{n}\cdot\nabla T_s) + \phi\lambda_f(\vec{n}\cdot\nabla T_f) = 0$$

  in which $\vec{0}$ is a null vector. For the thermal radiation exchange, the following form of the Marshak boundary conditions is used [48]:

  $$\frac{\varepsilon_w}{2(2-\varepsilon_w)}\big(4\sigma T_s^4 - G\big) = \frac{1}{3\beta}\vec{n}\cdot\nabla G \tag{3.25}$$

  where ε_w is the emissivity of the wall and T_s is the temperature of the wall. Considering that the wall of the receiver is opaque and its absorptivity equals its emissivity according to the Kirchhoff's law [48], then its emissivity and its albedo are related through $\varepsilon_w = 1 - \omega_w$ [48].

3.3 Numerical method

The constitutive equations for mass, momentum and energy conservation were solved in Cartesian coordinates using finite volume method (FVM) in OpenFOAM (v3.0+) [54], a free open source Computational Fluid Dynamic (CFD) software. The pressure-velocity coupling is solved using the SIMPLE (Semi-Implicit Method for Pressure Linked Equations) algorithm [55, 56]. A new solver in OpenFOAM was programmed based on an existing solver and then the MCRT method, which was developed in Octave (3.6.0) [57], was coupled to this solver for the statistical analysis in the CFD mesh, as described in Section 3.3.1. The parameters used to simulate the system are described in Section 3.3.2.

3.3.1 CFD mesh and its coupling with the MCRT method

Different grid structures can be used to mesh a cylindrical geometry [58]. If a simple polar grid is used, it leads to a singularity problem in the centre of the receiver [59], which should be solved. A multi block-structure approach known as butterfly grid [58] is usually adopted to overcome this problem, which gives better results than the other types of meshes according to Hernandez-Perez et al. [58]. Fig. 3.3 shows a quarter of the circular section of the receiver according to this approach, divided into three zones: a central square (1); and two symmetrical areas (2 and 3) delimited by the boundary of the central square zone (1), the bisectrix CF and the receiver perimeter. The grid zones of remainder quarters of the receiver are symmetrical to those shown in Fig. 3.3. Simulations using different size of the central square were carried out, and using OpenFOAM functions it was found that using a central square zone with diagonal equal to half of the receiver radius leads to a better mesh quality. In this case, the worst irregularity of the mesh is near the point C.

Therefore, in order to increase as maximum as possible the mesh quality, a smoothing tecnique available in the OpenFOAM community [60] was also applied. It should be noted that after applying this technique some points of the mesh will move slightly, but the grid topology still be the same. Regarding the number of nodes, it is considered that all the lines shown in Fig. 3.3 (DA=CB=FE, AB=DC=GF and BE=CF=DG) have the same number of nodes, which will lead to a more uniform grid. A uniform distribution of nodes is used along the height of the receiver. The number of nodes used and the final structure of the mesh are presented and discussed in Section 3.3.3, where some grid-independence testes are also reported.

The CFD and MCRT models are coupled by counting the absorbed solar rays obtained as described in Section 3.2.4 in the CFD mesh. For each element of volume (cell), the number of rays that are inside it is counted using internal OpenFOAM functions, and then the spatial distribution of the absorbed solar radiation is computed

using Eq. (3.21), which is then included in the energy conservation equation of the solid phase (Eq. (3.8)).

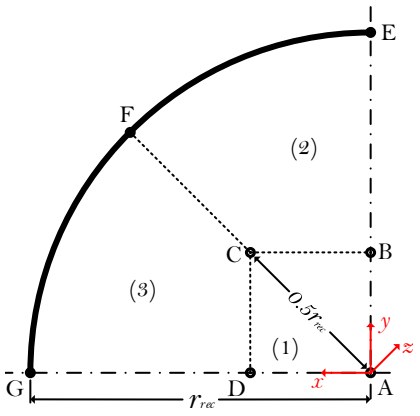

Fig. 3.3: Topology for the CFD mesh.

3.3.2 Parameters of the reference configuration

Table 3.1 presents the values of the radius r_{rec} and height L of the receiver, diameter of the pores d_p, porosity ϕ, emissivity of the ceramic foam ε and wall ε_w, asymmetry factor g of the phase function and thermal conductivity λ_s of the ceramic foam, used in this study. The material of the receiver is silicon carbide (SiC) foam with a constant value of thermal conductivity obtained from the work of Villafán-Vidales et al. [61] and Eom et al. [6].

Table 3.1: Geometric parameters of the porous volumetric receiver and transport properties of the solid material.

Parameter	Value
r_{rec} (cm)	2.5
L (cm)	5
d_p (mm)	3
ϕ	0.9
ε	0.92
ε_w	0.8
g	0
λ_s (W m^{-1} K^{-1})	80

The concentration of the solar radiation is modelled through the Tonatiuh software including the effect of the circumsolar radiation ratio (CSR) described by the Buie distribution [62, 63] for clear sky condition, which corresponds to model the sun as a dish (half angle of $\theta_s = 4.65$ mrad) together with the circumsolar aureole. Table 3.2

presents this value and the concentration ratio C, focal distance f of the parabolic dish, distance d_f (see Fig. 2.6), direct normal irradiance DNI and reflectivity ρ_{dis} of the parabolic dish, used to simulate the concentration system. A total number of rays of 1×10^8 is used in this simulation, which is enough to ensure that the error of the absorbed solar radiation distribution in the receiver is low [15].

Table 3.2: Simulation conditions of the solar concentration system.

Parameter	Value
C	500
f (cm)	70
d_f (cm)	2.25
DNI (W m^{-2})	800
ρ_{dis}	0.95
CSR	2%

For the fluid flow and heat transfer boundary conditions, the superficial velocity and the temperature of the air at the inlet are $\vec{U}_{in} = (0, 0, 1.5)$ m s^{-1} according to the coordinate system shown in Fig. 3.3 and $T_{in} = 300$ K, respectively. For the pressure at the outlet, it is used the normal atmospheric pressure $p_{out} = 1.013\,25 \times 10^5$ Pa. For the convergence criteria, a normalised residual error of 1×10^{-7} was used for the mass (continuity), momentum, fluid and solid phases and radiative transfer equations.

3.3.3 Grid-independence study

A grid-independence study was done to select the optimum size of the mesh considering the conditions presented in Section 3.3.2 and using the parabolic dish to generate the concentrated solar radiation field on the inlet of the receiver, as explained in Section 3.2.4. For this purpose, 40 nodes in the line segments shown in Fig. 3.3 of Section 3.3.1 and 100 nodes along the height of the receiver with a uniform distribution were used as a benchmark solution. A refinement of the mesh near the inlet and wall were tested, but the impact on the overall results are minimal, which do not justify the refinements. For this reason a uniform mesh was used.

Fig. 3.4 shows the temperature profiles of the solid and fluid phases along the axis and the radial distance at the outlet of the receiver for different mesh sizes, including the benchmark solution. These results show that using a mesh size of 20x70, where 20 is the number of nodes on the line segments explained in Section 3.3.1, and 70 is the number of nodes along the height of the receiver, the maximum difference of the temperature profile of the solid and fluid phases relative to the benchmark solution is less than 0.2%. For this reason, and due to a compromise with the computation

time, a grid size of 20x70 was selected for this study, as shown in Fig. 3.5 (a). Fig. 3.5 (b) shows the real cylinder receiver made of SiC ceramic foam considered in this study, which was provided by LANIK ceramic foam company [64].

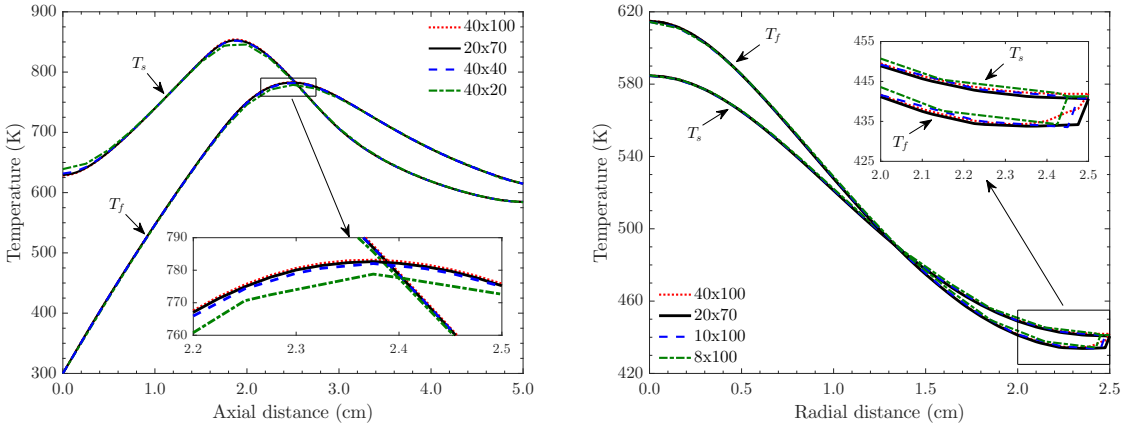

(a) (b)

Fig. 3.4: Temperature of the solid and fluid phases along the axis (a) and the radial distance at the outlet (b) of the receiver for different mesh sizes.

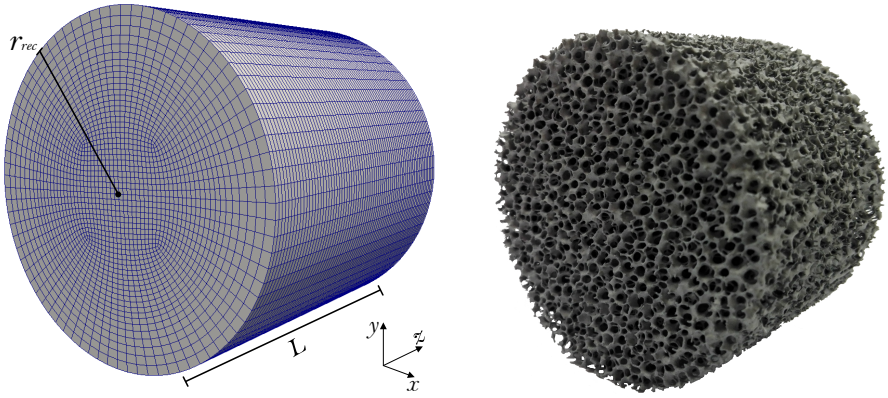

(a) (b)

Fig. 3.5: View of the selected mesh size with 20x70 nodes (a) and the real SiC ceramic foam provided by LANIK ceramic foam company [64] (b).

3.3.4 Comparison of the present model with previous works

The validation of the MCRT method is presented in the work of Barreto et al. [15], in which the results show excellent agreement (errors less than 0.41%) with the work of van de Hulst [65]. The validation of the CFD model (fluid flow and heat transfer processes) was done comparing the temperature of the fluid and solid phases along the axis of the receiver with that obtained by Wu et al. [20] for a test case. This test case is characterised by a diameter of the pores of $d_p = 1.5$ mm, a porosity $\phi = 0.8$,

an emissivity of the porous material and wall of $\varepsilon = 0.95$ and $\varepsilon_w = 1$, respectively, a uniform normal incident solar flux at the inlet of 600 kW m^{-2} and two different values of inlet superficial velocity of $\vec{U}_{in} = (0, 0, 2.16)$ m s^{-1} and $\vec{U}_{in} = (0, 0, 1.08)$ m s^{-1}. All the other parameters (boundary conditions and properties of the porous media) remain the same to those presented in Section 3.3.2. Fig. 3.6 shows the results of the test case, where the two models show an excellent agreement. The temperature of the solid has the highest deviation, but with differences less than 1.8% when $\vec{U}_{in} = (0, 0, 1.08)$ m s^{-1} and 1% for $\vec{U}_{in} = (0, 0, 2.16)$ m s^{-1}. It should be noted that their model was validated with experimental measurements obtained by testing a volumetric open air receiver made of open-cell SiC ceramic foam in a solar furnace at a laboratory scale. Model results agreed well with the experimental tests, with errors less than 10% in the temperature of the solid phase [20]. This shows that the present model also generate valid results, with errors in the same order of magnitude, and thus it is appropriate to model volumetric receivers successfully (Fig. 3.6).

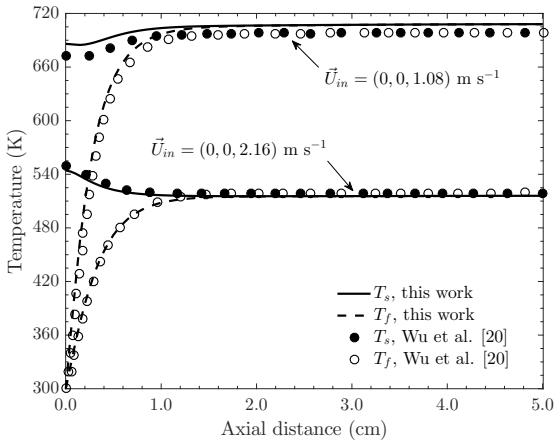

Fig. 3.6: Temperature of the solid and fluid phases along the axis of the receiver obtained in this work and from Wu et al. [20].

3.4 Results and discussion

The CFD and MCRT models are coupled together and used to simulate the performance of the reference configuration of the porous volumetric receiver, using a parabolic dish to generate the concentrated solar radiation field on the receiver aperture. The concentration system is designed for $2.3\theta_s$ (10.8 mrad of acceptance angle), but a receiver with a larger aperture area ($r_{rec} = 2.5$ cm) is placed below the focal point using $d_f = 2.25$ cm (see Fig. 2.6), because a smoother solar radiation flux and angle of incidence distributions are obtained for this case without decreasing the optical efficiency. Section 3.3.2 presents the simulation parameters for this reference configuration. Due to the symmetry of the problem when using a parabolic dish, only

the results for a cross section along the axial distance of the receiver are presented.

The simulation of the concentration system resulted in an efficiency of 93.71%, defined as the ratio between the total solar power available at the receiver inlet and the power available at the parabolic dish aperture (it includes the reflection loss of the concentrator). Fig. 3.7 shows the obtained radial distribution of the concentrated solar radiation and the mean angle of incidence on the receiver inlet. The solar radiation flux decreases from the centre to the border of the receiver inlet, and the mean angle of incidence has an inverse variation. The effect of the receiver shadow on the concentrator it is also observed, wherein the flux close to the centre decreases. Different values of the distance between the receiver inlet and the focal point (d_f) and of the focal length of the parabolic dish (f) result in different flux distributions.

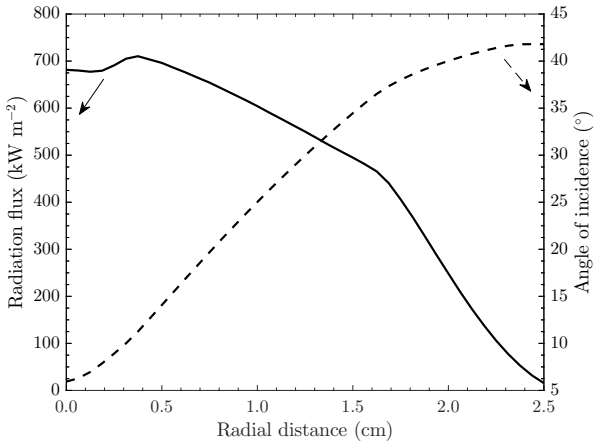

Fig. 3.7: Radial distribution of the perimetrically averaged concentrated solar radiation flux and angle of incidence on the receiver inlet.

3.4.1 Reference configuration of the porous volumetric receiver

Fig. 3.8 presents the spatial distribution of the absorbed solar radiation in the porous structure for the reference configuration of the receiver. A peak of absorption of 142 MW m^{-3} is observed in the porous structure, close to the focal point of the concentrator. This peak is caused by the convergent angles of incidence of solar radiation and the high porosity and pores size of the porous material used.

Fig. 3.9 shows the spatial distributions of the solid and fluid phases temperature. There is a hot spot of 853 K in the porous structure, in the same region of the maximum absorption of solar radiation, while the fluid phase has its highest temperature of 783 K slightly downstream in the direction of the flow due to the convection. Different inlet fluid velocity, porosity, pores size, thermal properties of the porous media and design of concentration system result in different temperature distributions.

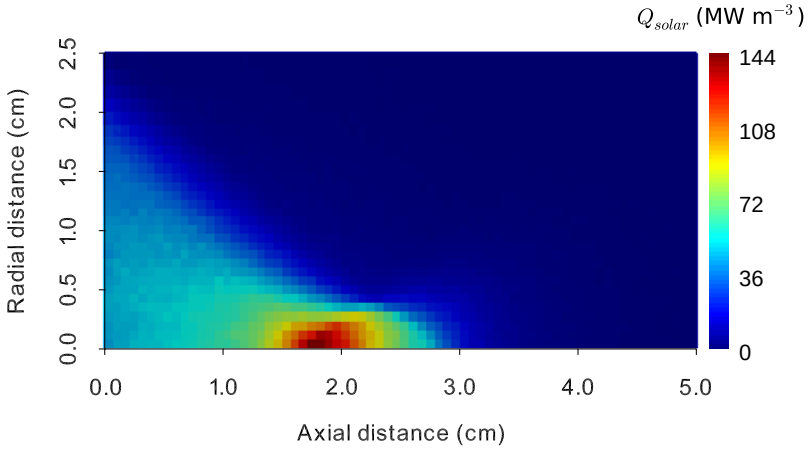

Fig. 3.8: Distribution of absorbed solar radiation in the porous structure.

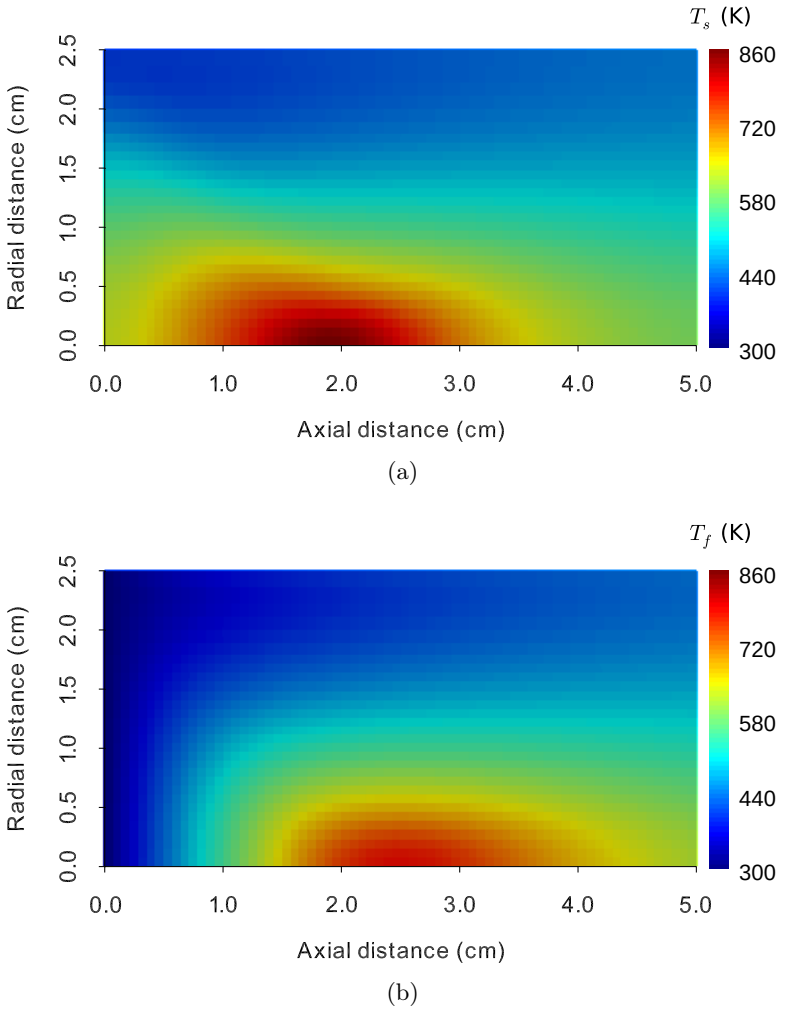

Fig. 3.9: Spatial distribution of the temperature of solid (a) and fluid (b) phases.

Fig. 3.10 and Fig. 3.11 present the convective heat transfer between the solid and fluid phases ($h_v(T_s - T_f)$) and the magnitude of the fluid velocity, respectively. Fig. 3.10 shows that the temperature of the fluid is slightly higher than the temperature

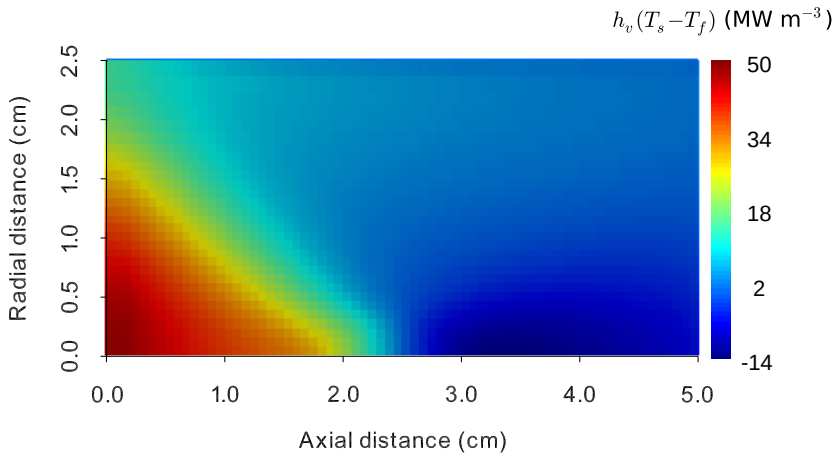

Fig. 3.10: Spatial distribution of the convective heat transfer between the solid and the fluid.

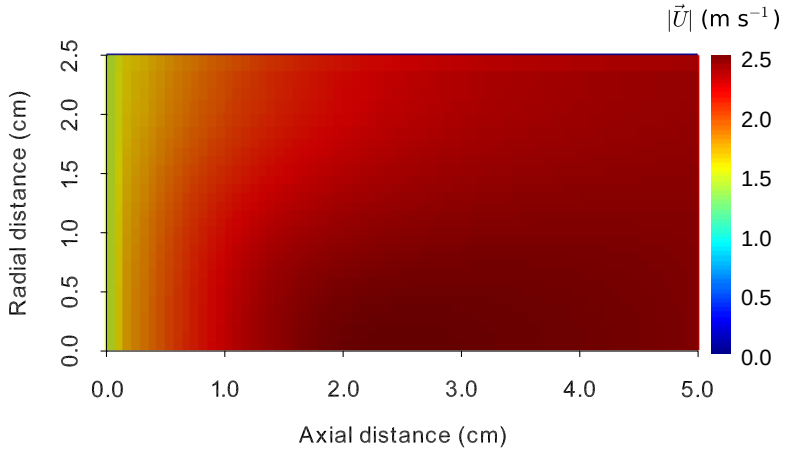

Fig. 3.11: Spatial distribution of the magnitude of the fluid velocity.

of the porous structure in the flow core region close to outlet, which means that heat transfers from the fluid to the solid matrix by convection (negative values). The same inversion on the temperature difference can also be found, for example, in the works of Chen et al. [18], Chen et al. [40] and Nimvari et al. [38]. This effect is mainly due to the lower absorption of solar radiation in that region, as shown in Fig. 3.8, and thus a lower temperature of the porous material. However, the most of this heat is transferred by conduction and thermal radiation to the colder regions of the solid matrix, namely in the outer annular region of the receiver, and then transferred back to the fluid. A small part is lost by thermal radiation through the outlet plane according to the imposed boundary condition. Regarding the magnitude of the fluid velocity, it is higher in the region of highest temperatures due to the variation of the fluid density.

The simulation of the reference configuration resulted in 628.92 W of thermal power output, 85.46% of thermal efficiency, 474.22 K of mean fluid temperature at

the outlet and a pressure drop across the receiver of 103.10 Pa. The thermal efficiency is defined as the ratio between the thermal power output and the total solar power available at the receiver inlet, while the pressure drop is the difference between the mean pressures at the receiver inlet and outlet. The final global efficiency of the concentrator and receiver is the product between the efficiency of the concentration system and thermal efficiency, which is 80.08%.

The losses of the receiver are divided in two parts: (i) optical losses, which are due to the propagation and absorption of solar radiation in the porous media; and (ii) thermal radiation losses, which are caused by the increasing temperature differences between the porous structure and the environment. The main losses are in the propagation and absorption of solar radiation (accounted in the thermal efficiency), in which a fraction of the incoming energy is lost through the inlet plane due to the backscattering.

Regarding to reference values of performance of porous volumetric receiver available in the literature, an example is the work of Zhu et al. [66], where an experimental analysis of a new design of a pressurised porous volumetric receiver coupled to a parabolic dish with a concentration ratio of 1750 is presented. Their receiver is made of 65 mm-tick nickel foam with 75 PPI (pores per inch), which means that the pore diameter is about 0.34 mm, and air is used as the heat transfer fluid. For the test conditions, it was found global efficiencies above 55%, with a maximum value of 87%, and mean fluid temperatures at the outlet between 673 K and 748 K. Other studies, including some for different designs of porous structure and other type of receivers, are described in the recent work of Sedighi et al. [67]. In this work, the mean fluid temperature can be increased, for example, increasing the concentration ratio and decreasing the inlet fluid velocity. Fig. 3.9 (b) of the present work shows that the radial profile of the fluid temperature at the outlet is not uniform, since the temperature in the core region is higher than that of the peripheral annular region. A smoother profile can be obtained, for example, by imposing a non-uniform distribution of the fluid velocity at the inlet, as is discussed in the work of Nimvari et al. [38], or having different porosities and pores sizes in the core and peripheral annular regions of the receiver. A lower fluid velocity at the inlet of the annular region of the present configuration will increase and smooth the radial profile of the fluid temperature at the outlet.

3.4.1.1 Study on the effect of different approaches for adiabatic boundary condition on the wall

Since the wall of the receiver is in contact with both solid matrix and fluid, makes its modelling as adiabatic more difficult. For this purpose, two approaches are typically considered, as described in the work of Yang et al. [68]. The first one (Model A) is

the used in this work as presented in Section 3.2.5. This model considers that there is a heat flux separation at the wall with different temperature gradients in the solid and fluid phases, and it can be implemented considering that the temperature of the film of fluid in contact with the wall is equal to the temperature of the solid (no-slip condition) and that the sum of the conduction heat fluxes in the two phases is zero. The second approach (Model B) considers that the temperature gradient at the wall is zero for both solid and fluid phases ($\vec{n} \cdot \nabla T_s = 0$ and $\vec{n} \cdot \nabla T_f = 0$). This approach leads to a problem since the temperature of the fluid at wall is not necessarily equal to the temperature of the solid, and thus it does not respect a consequence of the no-slip condition. To show the differences between these two approaches, Fig. 3.12 presents the temperature of the solid and fluid phases along the radial distance at the height $L/10$, and Table 3.3 presents the thermal efficiency (η_{th}), mean fluid temperature at the outlet ($\overline{T}_f$) and pressure drop (Δp), for these two approximations. The impact on the overall results are minimal but the main difference is in the temperatures close to the wall, where the two temperatures are different in the case of Model B. This bias increases near the receiver inlet because this is the region where the two temperatures are most different in the core flow region.

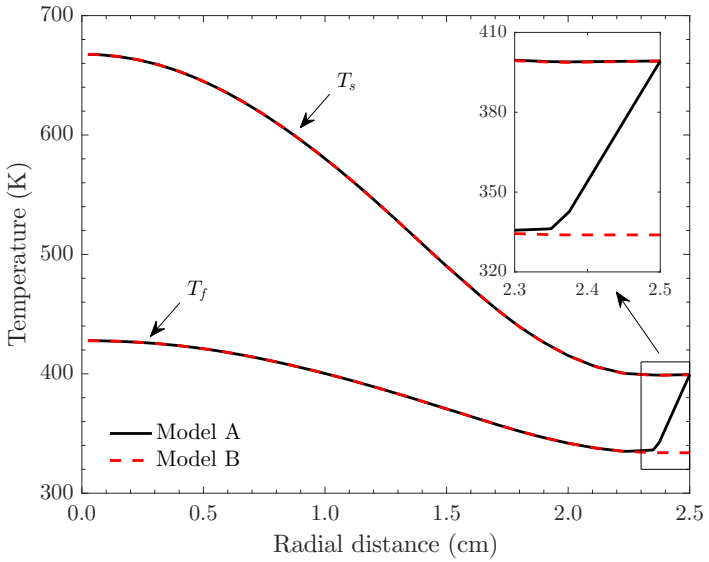

Fig. 3.12: Temperature profile of the solid and fluid phases for different adiabatic boundary conditions approaches.

Table 3.3: Thermal and hydrodynamic performance of the thermal receiver for different adiabatic boundary conditions approaches.

Model	η_{th} (%)	$\overline{T}_f$ (K)	Δp (Pa)
A	85.46	474.22	103.10
B	84.71	472.88	102.75

3.4.2 Study on the effect of the geometric parameters of the receiver element

The temperature of the solid and fluid phases strongly depends on the receiver porosity and pores size, which are the two main parameters of porous media. To better understand the effect of these parameters on the receiver performance, this section presents the temperature distribution in the solid and fluid phases, the thermal efficiency and the pressure drop across the receiver for two different values of porosity and pores size. All the other parameters of the reference configuration are kept equal to those presented in Section 3.3.2.

Fig. 3.13 and Fig. 3.14 show the temperature of the solid and fluid phases, respectively, for porosity values of 0.8 and 0.7. Fig. 3.15 presents the temperature profiles along the axis of the receiver for these two cases. Receiver elements with higher porosity allow the solar radiation to be absorbed more in-depth in the solid matrix, which makes the higher temperatures to occur in that core region (Fig. 3.13 (a), Fig. 3.14 (a) and Fig. 3.15). In the opposite, in receiver elements with lower porosity (Fig. 3.13 (b), Fig. 3.14 (b) and Fig. 3.15), the peaks of absorbed solar radiation and temperature are closer to the inlet.

Fig. 3.16 and Fig. 3.17 show the temperature of the solid and fluid, respectively, for pores sizes of 2 mm and 1 mm. Fig. 3.18 presents the temperature profiles along the axis of the receiver for these two cases. The pores size has a similar effect as porosity on the temperature distributions in the receiver element. A larger pores size results in higher values of temperature more in-depth in the solid matrix (Fig. 3.16 (a), Fig. 3.17 (a) and Fig. 3.18), while a smaller pores size results in lower peak temperatures closer to the receiver element inlet (Fig. 3.16 (b), Fig. 3.17 (b) and Fig. 3.18).

Table 3.4: Thermal and hydrodynamic performance for thermal receiver elements with different values of porosity.

ϕ	η_{th} (%)	$\overline{T}_f$ (K)	Δp (Pa)
0.8	85.52	471.35	198.98
0.7	85.28	470.24	374.81

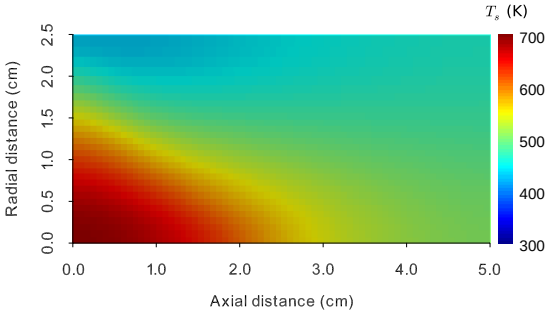

(a) $\phi = 0.8$

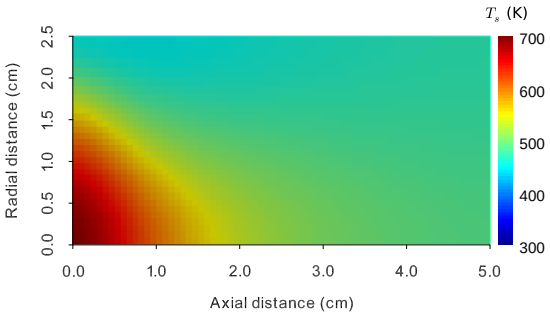

(b) $\phi = 0.7$

Fig. 3.13: Spatial distribution of temperature in the porous structure for receiver elements with different porosity.

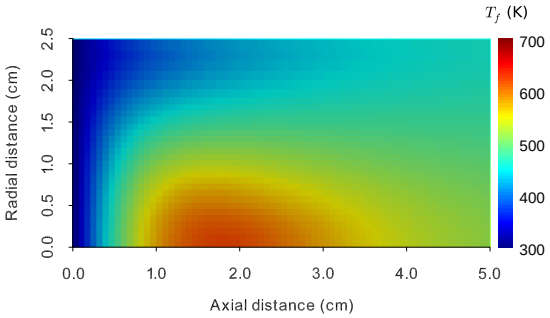

(a) $\phi = 0.8$

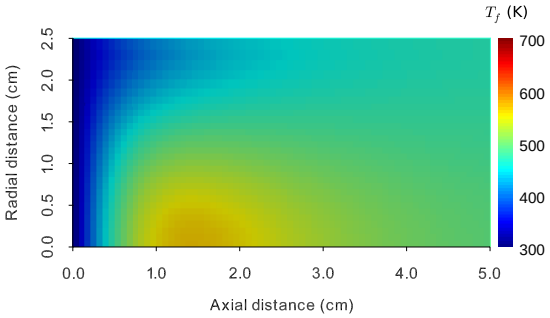

(b) $\phi = 0.7$

Fig. 3.14: Spatial distribution of fluid temperature for receiver elements with different porosity.

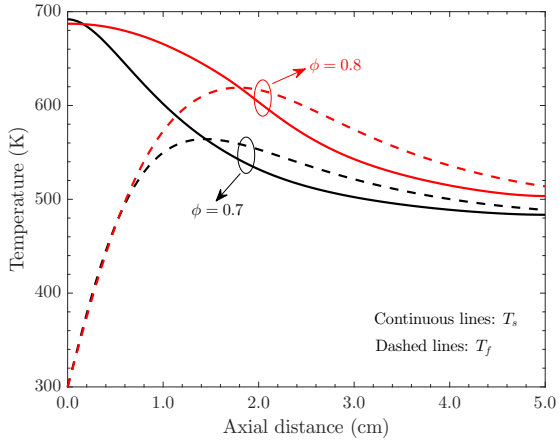

Fig. 3.15: Temperature of the solid and fluid phases along the axis of the receiver for different values of porosity.

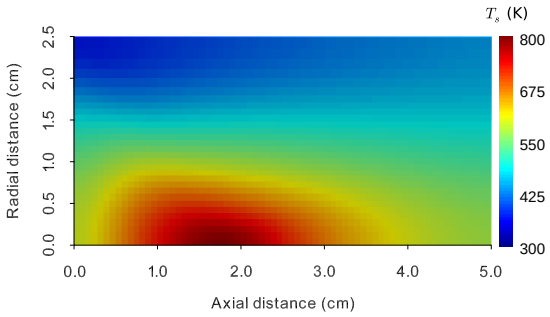

(a) $d_p = 2$ mm

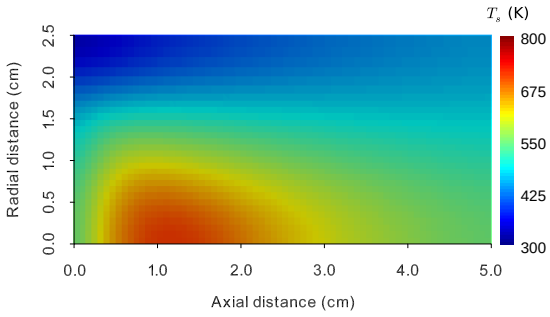

(b) $d_p = 1$ mm

Fig. 3.16: Spatial distribution of temperature in the porous structure for receiver elements with different pores size.

Table 3.5: Thermal and hydrodynamic performance for thermal receiver elements with different pores sizes.

d_p (mm)	η_{th} (%)	$\overline{T}_f$ (K)	Δp (Pa)
2	85.46	473.83	190.55
1	85.13	471.67	592.55

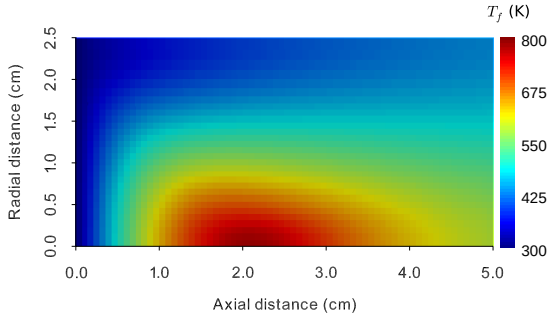

(a) $d_p = 2$ mm

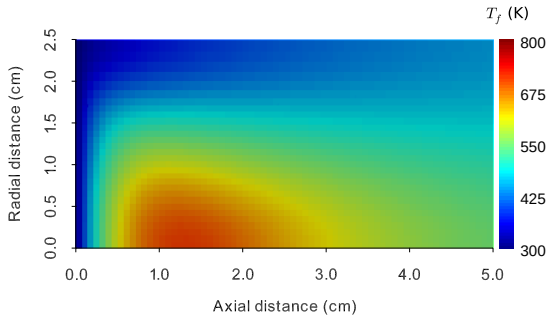

(b) $d_p = 1$ mm

Fig. 3.17: Spatial distribution of fluid temperature for receiver elements with different pores size.

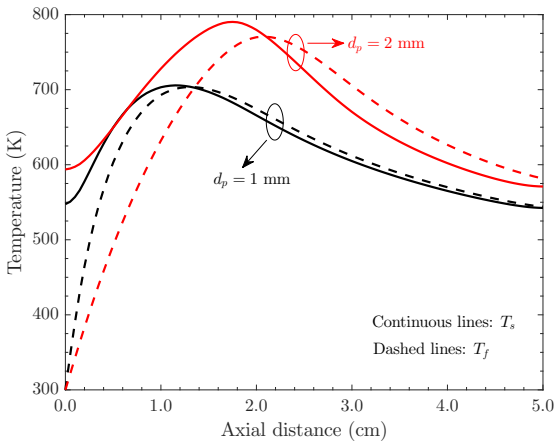

Fig. 3.18: Temperature of the solid and fluid phases along the axis of the thermal receiver for different pores sizes.

Fig. 3.18 shows that the decreasing of the pores size decreases the temperature difference between the fluid and solid. The reason is that lower pores size means higher volumetric convective heat transfer coefficient and heat transfer area, which increases the heat transfer between the solid and fluid and reducing the temperature difference. This is an example when the local thermal equilibrium (LTE) approach can be a good approximation to study porous volumetric receivers.

Table 3.4 and Table 3.5 show the thermal efficiency, mean fluid temperature at the outlet and pressure drop, respectively, for the two porosities and pores sizes. Receivers with lower porosity or pores size cause a higher pressure drop, which means that more power is needed to pump the fluid through the receiver. The thermal efficiency and the mean fluid temperature do not vary significantly for the used range of porosities and pores sizes, but receiver elements with higher porosity and pores size have slightly higher thermal efficiencies and mean fluid temperatures.

It worth to mention that if the internal geometry of the receiver is changed the spatial distribution of the absorbed solar radiation, fluid velocity and heat transfer conditions are all modified. Therefore, the optimisation of the receiver should consider the distribution of the absorbed solar radiation to avoid peaks of temperature, which can damage the receiver material, but also keeping good heat transfer and fluid flow conditions.

3.4.3 Study on the effect of convergent and divergent incidence of solar rays

The results presented in previous sections are for the case of convergent incidence angles of solar rays on the receiver inlet using $d_f = 2.25$ cm. This section presents the temperature distributions in the solid and fluid phases for convergent and divergent incidence angles at the inlet. The convergent or divergent incidence is obtained by placing the receiver inlet plane below ($d_f > 0$) or above ($d_f < 0$) the focal point, respectively (see Fig. 2.6).

Fig. 3.19 and Fig. 3.20 present the temperature distribution in the solid and fluid phases, respectively, for convergent ($d_f = 1.5$ cm) and divergent ($d_f = -1.5$ cm) incidence of solar rays. Fig. 3.21 presents the temperature profiles along the axis of the receiver for these two cases. The main difference between these two configurations, is that for divergent incidence, the temperature distribution in the solid (Fig. 3.19 (b)) and in the fluid (Fig. 3.20 (b)) are more uniform than in the case of convergent incidence (Fig. 3.19 (a) and Fig. 3.20 (a)). For convergent incidence, a temperature peak of 1220 K occurs in the region near the focal point, while for divergent incidence angles a much lower peak of 675 K is observed. In this case, the wall absorbs a larger amount of solar radiation, which increases the temperature close to the wall. Table 3.6 shows the efficiency of the concentration system (η_{cs}), thermal efficiency, mean fluid temperature at the outlet and pressure drop, respectively, for the two values of the distance d_f. The receiver is more efficient for the case of divergent angles of incidence than for convergent incidence due to the high temperatures obtained in this last case, which cause higher thermal losses.

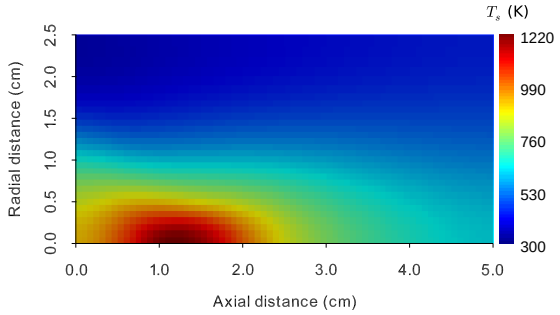

(a) $d_f = 1.5$ cm

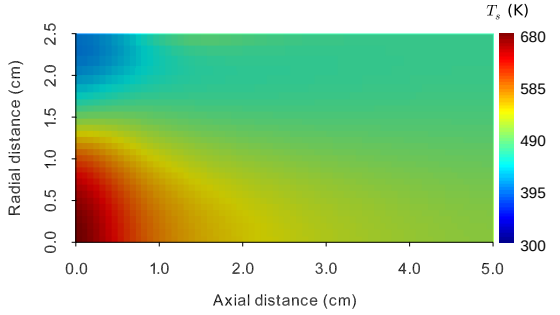

(b) $d_f = -1.5$ cm

Fig. 3.19: Spatial distribution of temperature in the porous structure for different configurations of the concentration system.

Table 3.6: Thermal and hydrodynamic performance of the thermal receiver for different configurations of the concentration system.

d_f (cm)	η_{cs} (%)	η_{th} (%)	$\overline{T}_f$ (K)	Δp (Pa)
1.5	94.04	84.29	474.95	102.51
−1.5	94.02	86.85	474.43	104.48

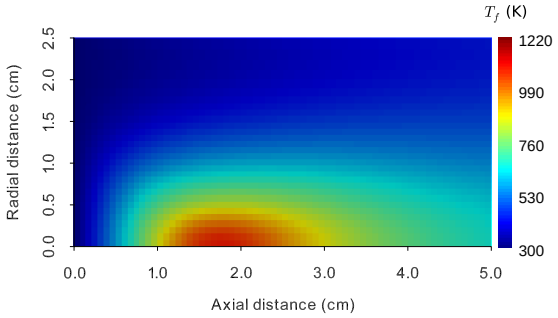

(a) $d_f = 1.5$ cm

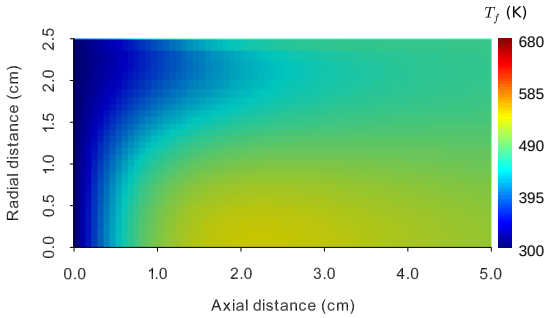

(b) $d_f = -1.5$ cm

Fig. 3.20: Spatial distribution of fluid temperature for different configurations of the concentration system.

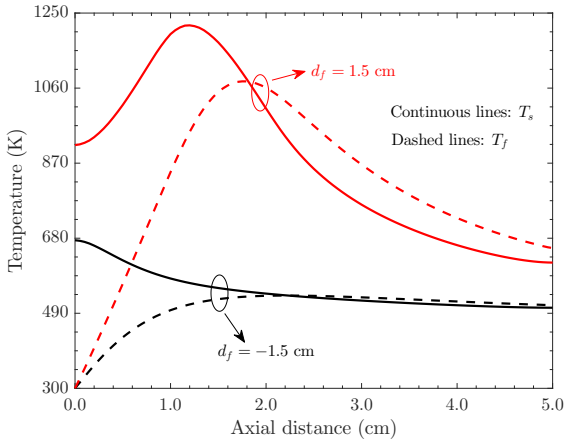

Fig. 3.21: Temperature of the solid and fluid phases along the axis of the thermal receiver element for different configurations of the concentration system.

3.5 Conclusions

In this work, a detailed three-dimensional modelling and thermal performance analysis of porous volumetric receivers coupled to solar concentration systems are presented. A cylindrical receiver element made of open-cell SiC ceramic foam was considered as reference configuration, with the concentrated solar radiation generated by a parabolic dish.

A detailed study on the effect of using different assumptions to describe the temperature profiles near the wall when adiabatic boundary condition is assumed is also presented. It was found that using heat flux separation for the solid and fluid at the side wall leads to more accurate results.

Results show that receivers with high porosity and pores size and convergent incidence of solar rays at the inlet plane generate a hot spot in the solid material in the region close to the focal point of the concentration system, while the highest temperature and velocity of the fluid are slightly downstream in direction of the flow due to the convection. It was also found that in the core flow region close to the outlet the fluid is hotter than the solid, which means that there is heat transfer from the fluid to the porous structure.

The use of receivers with high porosity and pores size increases the thermal efficiency and decreases the pressure drop substantially. The convergent incidence of solar rays leads to peaks of temperature in the solid and fluid. A way to minimise these peaks is to design the concentration system or place the receiver in such way to obtain lower incidence angles at the inlet, which also leads to an increases of the thermal efficiency because slightly lower temperatures are obtained for this configuration.

The receiver performance and durability can be improved by finding the porosity, pores size and fluid flow conditions that increase its thermal efficiency while not increasing too much the pressure drop and temperature peaks. In the future, this global model will be used to carry out several optimisations also taking into account different concentration systems, as tower type concentrators, with and without second stage concentration.

References

[1] C. K. Ho and B. D. Iverson. Review of high-temperature central receiver designs for concentrating solar power. *Renew Sust Energ Rev*, 29:835–846, 2014.

[2] F. Bai. One dimensional thermal analysis of silicon carbide ceramic foam used for solar air receiver. *Int J Therm Sci*, 49:2400–2404, 2010.

[3] J.-F. P. P. de la Beaujardiere and H. C. R. Reuter. A review of performance

modelling studies associated with open volumetric receiver CSP plant technology. *Renew Sust Energ Rev*, 82:3848–3862, 2018.

[4] M. A. Silva-Pérez. Solar power towers using supercritical CO_2 and supercritical steam cycles, and decoupled combined cycles. *Adv Conc Sol Therm Res Techno*, 383–402, 2017.

[5] A. L. Ávila-Marín. Volumetric receivers in Solar Thermal Power Plants with Central Receiver System technology: A review. *Sol Energy*, 85:891–910, 2011.

[6] J.-H. Eom, Y.-W. Kim, and S. Raju. Processing and properties of macroporous silicon carbide ceramics: A review. *J Asian Ceram Soc*, 1:220–242, 2013.

[7] F. Gomez-Garcia, J. González-Aguilar, G. Olalde, and M. Romero. Thermal and hydrodynamic behavior of ceramic volumetric absorbers for central receiver solar power plants: A review. *Renew Sust Energ Rev*, 57:648–658, 2016.

[8] R. Capuano, T. Fend, P. Schwarzbözl, O. Smirnova, H. Stadler, B. Hoffschmidt, and R. Pitz-Paal. Numerical models of advanced ceramic absorbers for volumetric solar receivers. *Renew Sust Energ Rev*, 58:656–665, 2016.

[9] C. Soulaine and M. Quintard. On the use of a Darcy–Forchheimer like model for a macro-scale description of turbulence in porous media and its application to structured packings. *Int J Heat Mass Tran*, 74:88–100, 2014.

[10] A. L. Ávila-Marín, J. Fernandez-Reche, and A. Martinez-Tarifa. Modelling strategies for porous structures as solar receivers in central receiver systems: A review. *Renew Sust Energ Rev*, 111:15–33, 2019.

[11] S. Du, M.-J. Li, Q. Ren, Q. Liang, and Y.-L. He. Pore-scale numerical simulation of fully coupled heat transfer process in porous volumetric solar receiver. *Energy*, 140:1267–1275, 2017.

[12] K. Vafai. *Handbook of porous media.* Taylor and Francis, New York, third edition, 2015.

[13] X. Chen, F. Wang, X. Yan, Y. Han, Z. Cheng, and C. Jie. Thermochemical performance of solar driven CO_2 reforming of methane in volumetric reactor with gradual foam structure. *Energy*, 151:545–555, 2018.

[14] S. Du, Y.-L. He, W.-W. Yang, and Z.-B. Liu. Optimization method for the porous volumetric solar receiver coupling genetic algorithm and heat transfer analysis. *J Heat Transf*, 122:383–390, 2018.

[15] G. Barreto, P. Canhoto, and M. Collares-Pereira. Three-dimensional modelling and analysis of solar radiation absorption in porous volumetric receivers. *Appl Energy*, 215:602–614, 2018.

[16] X. Chen, X.-L. Xia, X.-H. Dong, and G.-L. Dai. Integrated analysis on the volumetric absorption characteristics and optical performance for a porous media receiver. *Energ Convers Manage*, 105:562–569, 2015.

[17] F. Q. Cui, Y. L. He, Z. D. Cheng, D. Li, and Y. B. Tao. Numerical simulations of the solar transmission process for a pressurized volumetric receiver. *Energy*, 46:618–628, 2012.

[18] X. Chen, X.-L. Xia, H. Liu, Y. Li, and B. Liu. Heat transfer analysis of a volumetric solar receiver by coupling the solar radiation transport and internal heat transfer. *Energ Convers Manage*, 114:20–27, 2016.

[19] F. Wang, Y. Shuai, H. Tan, and C. Yu. Thermal performance analysis of porous media receiver with concentrated solar irradiation. *Int J Heat Mass Tran*, 62: 247–254, 2013.

[20] Z. Wu, C. Caliot, G. Flamant, and Z. Wang. Coupled radiation and flow modeling in ceramic foam volumetric solar air receivers. *Sol Energy*, 85:2374–2385, 2011.

[21] Y. Li, X.-L. Xia, C. Sun, Q. Ai, and H.-P. Tan. Radiative characteristics of Voronoi open-cell foams made from semitransparent media. *Int J Heat Mass Tran*, 133:1008–1018, 2019.

[22] Y. Li, X.-L. Xia, C. Sun, J. Wang, and H.-P. Tan. Tomography-based radiative transfer analysis of an open-cell foam made of semitransparent alumina ceramics. *Sol Energ Mat Sol C*, 188:164–176, 2018.

[23] Y. Li, X.-L. Xia, C. Sun, Q. Ai, B. Liu, and H.-P. Tan. Tomography-based analysis of apparent directional spectral emissivity of high-porosity nickel foams. *Int J Heat Mass Tran*, 118:402–415, 2018.

[24] Y. Li, X.-L. Xia, C. Sun, S.-D. Zhang, and H.-P. Tan. Volumetric radiative properties of irregular open-cell foams made from semitransparent absorbing-scattering media. *J Quant Spectrosc Ra*, 224:325–342, 2019.

[25] X.-L. Xia, Y. Li, C. Sun, Q. Ai, and H.-P. Tan. Integrated simulation of continuous-scale and discrete-scale radiative transfer in metal foams. *J Quant Spectrosc Ra*, 212:128–138, 2018.

[26] Y. Li, X.-L. Xia, C. Sun, S.-D. Zhang, and H.-P. Tan. Integrated simulation of continuous-scale and discrete scale radiative transfer in an open-cell foam made

of semitransparent absorbing scattering ceramics. *J Quant Spectrosc Ra*, 225: 156–165, 2019.

[27] H. Xu, L. Gong, S. Huang, and M. Xu. Non-equilibrium heat transfer in metal-foam solar collector with no-slip boundary condition. *Int J Heat Mass Tran*, 76: 357–365, 2014.

[28] L. B. Younis and R. Viskanta. Experimental determination of the volumetric heat transfer coefficient between stream of air and ceramic foam. *Int J Heat Mass Tran*, 36:1425–1434, 1993.

[29] S. Du, Z.-X. Tong, H.-H. Zhang, and Y.-L. He. Tomography-based determination of Nusselt number correlation for the porous volumetric solar receiver with different geometrical parameters. *Renew Energ*, 135:711–718, 2019.

[30] Z. Wu, C. Caliot, G. Flamant, and Z. Wang. Numerical simulation of convective heat transfer between air flow and ceramic foams to optimise volumetric solar air receiver performances. *Int J Heat Mass Tran*, 54:1527–1537, 2011.

[31] A. L. Ávila-Marín, C. Caliot, G. Flamant, M. A. de Lara, and J. Fernandez-Reche. Numerical determination of the heat transfer coefficient for volumetric air receivers with wire meshes. *Sol Energy*, 162:317–329, 2018.

[32] X.-l. Xia, X. Chen, C. Sun, Z.-h. Li, and B. Liu. Experiment on the convective heat transfer from airflow to skeleton in open-cell porous foams. *Int J Heat Mass Tran*, 106:83–90, 2017.

[33] Z. Nie, Y. Lin, and Q. Tong. Numerical investigation of pressure drop and heat transfer through open cell foams with 3D Laguerre-Voronoi model. *Int J Heat Mass Tran*, 113:819–839, 2017.

[34] Z. Wu, C. Caliot, F. Bai, G. Flamant, Z. Wang, J. Zhang, and C. Tian. Experimental and numerical studies of the pressure drop in ceramic foams for volumetric solar receiver applications. *Appl Energy*, 87:504–513, 2010.

[35] D. Y. Kim and K. C. Kim. An experimental study on the thermal and hydraulic characteristics of open-cell nickel and copper foams for compact heat exchangers. *Int J Heat Mass Tran*, 130:162–174, 2019.

[36] F. Zaversky, L. Aldaz, M. Sánchez, A. L. Ávila-marín, M. I. Roldán, J. Fernández-Reche, A. Füssel, W. Beckert, and J. Adler. Numerical and experimental evaluation and optimization of ceramic foam as solar absorber – Single-layer vs multi-layer configurations. *Appl Energ*, 210:351–375, 2018.

[37] O. Smirnova, T. Fend, R. Capuano, G. Feckler, P. Schwarzbözl, and F. Sutter. Determination of critical thermal loads in ceramic high concentration solar receivers. *Sol Energ Mat Sol C*, 176:196–203, 2018.

[38] M. E. Nimvari, N. F. Jouybari, and Q. Esmaili. A new approach to mitigate intense temperature gradients in ceramic foam solar receivers. *Renew Energ*, 122:206–215, 2018.

[39] S. Du, Q. Ren, and Y.-L. He. Optical and radiative properties analysis and optimization study of the gradually-varied volumetric solar receiver. *Appl Energy*, 207:27–35, 2017.

[40] X. Chen, X.-L. Xia, X.-W. Yan, and C. Sun. Heat transfer analysis of a volumetric solar receiver with composite porous structure. *Energ Convers Manage*, 136: 262–269, 2017.

[41] Q. Zhu and Y. Xuan. Performance analysis of a volumetric receiver composed of packed shaped particles with spectrally dependent emissivity. *Int J Heat Mass Tran*, 122:421–431, 2018.

[42] H. Xu. Performance evaluation of multi-layered porous-medium micro heat exchangers with effects of slip condition and thermal non-equilibrium. *Appl Therm Eng*, 116:516–527, 2017.

[43] R. W. Fox, A. T. McDonald, and P. J. Pritchard. *Introduction to Fluid Mechanics*. Wiley, United State of America, sixth edition, 2004.

[44] W. Sutherland. Lii. the viscosity of gases and molecular force. *The London, Edinburgh, and Dublin Philosophical Magazine and Journal of Science*, 36: 507–531, 1893.

[45] M. A. Schuetz and L. R. Glicksman. A basic study of heat transfer through foam insulation. *J Cell Plast*, 20:114–121, 1984.

[46] K. Kamiuto. *Modeling of Composite Heat Transfer in Open-Cellular Porous Materials at High Temperatures*, 165–198. Wiley-Blackwell, 2008.

[47] G. W. Mulholland. *Smoke production and properties, SFPE Handbook of Fire Protection Engineering*. National Fire Protection Associationss, Quincy, MA, 1995.

[48] M. F. Modest. *Radiative Heat Transfer*. Academic Press, New York, third edition, 2013.

[49] C.-L. Tien and B. L. Drolen. Thermal radiation in particulate media with dependent and independent scattering. *Annu Rev Heat Transf*, 1:1–32, 1987.

[50] S. Cunsolo, M. Oliviero, W. M. Harris, A. Andreozzi, N. Bianco, W. K. S. Chiu, and V. Naso. Monte Carlo determination of radiative properties of metal foams: Comparison between idealized and real cell structures. *Int J Therm Sci*, 87: 94–102, 2015.

[51] M. J. Blanco, J. M. Amieva, and A. Mancillas. The tonatiuh software development project: an open source approach to the simulation of solar concentrating systems. 157–164, 2005.

[52] L. G. Heney and J. L. Greenstein. Diffuse radiation in the Galaxy. *Astrophys*, J. 93:70–83, 1940.

[53] Y.-L. He, F.-Q. Cui, Z.-D. Cheng, Z.-Y. Li, and W.-Q. Tao. Numerical simulation of solar radiation transmission process for the solar tower power plant: From the heliostat field to the pressurized volumetric receiver. *Appl Therm Eng*, 61: 583–595, 2013.

[54] www.openfoam.com/, 2017.

[55] J. H. Ferziger and M. Peric. *Computational Methods for Fluid Dynamics*. Springer, New York, third edition, 2002.

[56] H. K. Versteeg and W. Malalasekera. *An Introduction to Computational Fluid Dynamics*. Pearson Education, England, second edition, 2007.

[57] www.gnu.org/software/octave/, 2017.

[58] V. Hernandez-Perez, M. Abdulkadir, and B. J. Azzopardi. Grid Generation Issues in the CFD Modelling of Two-Phase Flow in a Pipe. *The Journal of Computational Multiphase Flows*, 3:13–26, 2011.

[59] L. Ma, D. B. Ingham, and X. Wen. A finite volume method for fluid flow in polar cylindrical grids. *International Journal for Numerical Methods in Fluids*, 28:663–677, 1998.

[60] Nathanaël. extblockmesh. www.github.com/Etudes-NG, 2014.

[61] H. I. Villafán-Vidales, S. Abanades, C. Caliot, and H. Romero-Paredes. Heat transfer simulation in a thermochemical solar reactor based on a volumetric porous receiver. *Appl Therm Eng*, 31:3377–3386, 2011.

[62] D. Buie, A. G. Monger, and C. J. Dey. Sunshape distributions for terrestrial solar simulations. *Sol Energy*, 74:113–122, 2003.

[63] D. Buie, C. J. Dey, and S. Bosi. The effective size of the solar cone for solar concentrating systems. *Sol Energy*, 74:417–427, 2003.

[64] LANIK foam ceramics. www.lanik.eu/en, 2018.

[65] H. C. van de Hulst. *Multiple Light Scattering*, volume II. Academic Press, New York, 1980.

[66] J. Zhu, K. Wang, G. Li, H. Wu, Z. Jiang, F. Lin, and Y. Li. Experimental study of the energy and exergy performance for a pressurized volumetric solar receiver. *Appl Therm Eng*, 104:212–221, 2016.

[67] M. Sedighi, R. V. Padilla, R. A. Taylor, M. Lake, I. Izadgoshasb, and A. Rose. High-temperature , point-focus , pressurised gas-phase solar receivers : A comprehensive review. *Energ Convers Manage*, 185:678–717, 2019.

[68] K. Yang, X. You, J. Wang, and K. Vafai. Analysis of two approaches for an adiabatic boundary condition in porous media. *Int J Number Method H*, 26: 977–998, 2016.

Nomenclature

C	concentration ratio (-)
c_p	specific heat capacity (J kg^{-1} K^{-1})
CSR	circumsolar ratio (-)
d_f	distance between the front face of the receiver and the focal point (m)
DNI	direct normal irradiance (W m^{-2})
d_p	mean pore (void) diameter (m)
e	power per ray (W)
f	focus length of the parabolic dish (m)
g	asymmetry factor of the phase function (-)
G	incident irradiance (W m^{-2})
h_v	volumetric convective heat transfer coefficient (W m^{-3} K^{-1})
L	height of the receiver (m)
l_β	path length of rays (m)
$\vec{M}_s$	momentum source vector (Pa m^{-1})
N	number of rays (-)
Nu	Nusselt number (-)
$\vec{n}$	unit normal vector (-)
p	pressure (Pa)

Q	heat source density (W m^{-3})
r	radius (m)
R	specific gas constant (J kg^{-1} K^{-1})
Re	Reynolds number (-)
S	Sutherland temperature (K)
T	temperature (K)
$\vec{u}$	average velocity (m s^{-1})
$\vec{U}$	superficial velocity ($\vec{U} = \phi\vec{u}$) (m s^{-1})
V	volume (m^3)

Greek symbols

β	extinction coefficient (m^{-1})
Δ	variation (-)
ε	emissivity (-)
η	efficiency (-)
θ	scattering angle (rad)
θ_s	half solar cone angle (rad)
κ_a	absorption coefficient (m^{-1})
κ_s	scattering coefficient (m^{-1})
λ	thermal conductivity (W m^{-1} K^{-1})
μ	dynamic viscosity (kg m^{-1} s^{-1})
ξ	random number uniformly distributed between 0 and 1 (-)
ρ	density (kg m^{-3}) or reflectivity of the parabolic dish (-)
σ	Stefan Boltzmann constant ($5.670\,367 \times 10^{-8}$ W m^{-2} K^{-4})
ϕ	porosity (-)
Φ	phase function (-)
ω	scattering albedo (-)

Subscripts

cs	concentration system
dis	parabolic dish
e	effective

ev	element of volume
f	heat transfer fluid (fluid phase)
in	inlet
ir	thermal radiation (infrared)
out	outlet
rec	volumetric receiver
ref	reference
s	solid matrix structure (solid phase)
$solar$	solar radiation
th	thermal
x, y, z	three-dimensional spatial coordinates
w	wall of the receiver

Chapter 4

Combined experimental and numerical determination of the asymmetry factor of scattering phase functions in porous volumetric solar receivers[†]

Abstract

Modelling of solar radiation propagation and absorption in porous media is a crucial part in the modelling of porous volumetric receivers in concentrated solar power (CSP) plants. The radiative properties of the porous media should be known in detail for accurate receiver modelling. In this work, an experimental study and a numerical model are combined aiming to estimate the asymmetry factor of Henyey-Greenstein (HG) scattering phase function in the visible spectral range for porous volumetric receivers made of open-cell silicon carbide (SiC) ceramic foam. For the experimental, the hemispherical diffuse reflectance of five different samples is measured using a collimated light source and an integrating sphere. For the numerical modelling, an algorithm based on a three-dimensional Monte Carlo Ray Tracing (MCRT) method was developed to simulate radiation propagation and absorption in porous media for the same conditions of the experimental apparatus. The asymmetry factor is determined by adjusting its value in the numerical model in order to minimize the difference between measured and simulated values. Results show that the solar radiation scattering in open-cell SiC ceramic foams is slightly backwards, being the optimum asymmetry factor of the Henyey-Greenstein phase function approximately -0.25, with a mean bias error of 0.0045% and a root mean square difference of 0.2926% between modelled and measured values of diffuse reflectance.

[†]Germilly Barreto[(1)], P. Canhoto[(1)], and M. Collares-Pereira[(1)]. Combined experimental and numerical determination of the asymmetry factor of scattering phase functions in porous volumetric solar receivers. *Solar Energy Materials and Solar Cells*, 206:110327, 2020.

[(1)] Institute of Earth Sciences, University of Évora.

Experimental results were also compared with the phase function for packing of spheres and with the isotropic scattering phase function. The first overpredicts the diffuse reflectance, while the second function underpredicts it.

Keywords: Solar energy; Volumetric receiver; Porous media; Open-cell ceramic foam; Diffuse reflectance; Scattering phase function.

4.1 Introduction

High temperature solar thermal volumetric receivers combined with advanced power cycles, such as the supercritical CO_2 closed-loop Brayton cycle [1], is a promising technology to improve the efficiency of concentrated solar power (CSP) plants [2]. Sedighi et al. [3] presented an in-depth look at the recent progresses in the high temperature central receiver designs, and they pointed out that there are needs for more proof-of-concept tests, since few studies have been carried out with real prototypes operating under real weather conditions. Among these type of receivers, the porous volumetric receivers are drawing the attention of researchers due to their capabilities to achieve high temperatures and high thermal efficiencies [4]. The working principle of the porous volumetric receivers consists on the absorption of the concentrated solar radiation in a volume that is occupied by a porous structure, through which also flows a heat transfer fluid that is heated, thus converting solar radiation into thermal energy [5]. These receivers are normally made of metal or ceramic materials, with ceramic materials being the most used due to their high melting point, low thermal expansion and resistance to oxidizing atmospheres [4, 6], which make them more suitable for the high temperature applications. The most used ceramic material is the silicon carbide (SiC) because of its radiative and thermal properties [6]. Regarding to geometry of the porous structure, there are two main configurations, which are the open-cell foams and the honeycomb structures [7]. The open-cell ceramic foams are the most investigated due to their good flow mixing capability and high heat transfer area [8], and are also used in many other thermal engineering applications, such as, porous burners [9, 10], heat exchangers [11, 12] or molten metal filters [13, 14].

The numerical modelling of porous volumetric receivers encompasses three main fields of study, which are: (i) propagation and absorption of solar radiation in the porous media [15]; (ii) fluid flow and heat transfer modelling in order to obtain the thermal and hydrodinamic performances [5] and (iii) prediction of radiative and transport properties of the porous media [16]. Other studies, such as determination of critical thermal loads [17], are also being conducted to improve the durability and stability of materials. There are two main approaches in the numerical modelling

of porous volumetric receivers. The first is the continuous-scale approach (CSA) [15], where the porous structure is assimilated to a continuous semi-transparent medium and the volume-averaged concept is used; and the other is the discrete-scale approach (DSA) [18], where the porous structure is modelled explicitly using a detailed description of the pores geometry. Recently, a new method known as scale-coupled approach (SCA) was proposed by Xia et al. [19] and Li et al. [20]. This approach consists in the combination of the CSA and DSA into a single computational domain, which allows to unite the advantages of both methods, that is, less computational effort (CSA) and accurate prediction of local radiative properties (DSA). The recent work of Avila-Marin et al. [21] presents a comprehensive review of the main strategies adopted to evaluate the performance of porous volumetric receivers in solar concentration systems. They concluded that the CSA combined with numerical Computational Fluid Dynamics (CFD) techniques, namely the local thermal non-equilibrium (LTNE) approach for the heat transfer modelling between the fluid and the solid matrix structure, is the most widely used strategy, as for example in the recent work of Barreto et al. [5].

The propagation and absorption of solar radiation and the thermal radiation exchange in porous media play an important role in the efficiency of porous volumetric receivers. Therefore, an accurate modelling of such phenomena is essential and thus it is important to know in detail the radiative properties of the porous media. These properties are the extinction coefficient (sum of the scattering and absortption coefficients), scattering albedo (ratio between the scattering and extinction coefficients) and scattering phase function [16]. Several studies have been conducted on the estimation of these properties, which can be divided in two main approaches. The first is the combination of experimental measurements with numerical modelling [22] (normally using the CSA) to predict the equivalent volumetric radiative properties of the porous media. The other approach consists in modelling an idealized structure of the porous media (DSA) obtained through a computational algorithm [16], or modelling the real structure obtained through tomography techniques [23, 24], which allows an accurate prediction of the local radiative properties. For both approaches, the Monte Carlo tracing (MCRT) method [15] is used to model the radiation propagation in the porous media.

In the work of Li et al. [16], a detailed analysis of the radiative properties of irregular open-cell foams is presented. They developed a MCRT method for a 3D foam structure generated thought Voronoi tessellation technique to extract the radiative properties. It was found that the extinction coefficient depends on the porosity, mean pores size and the shape of the ligaments of the porous structure; the scattering albedo depends on the radiative properties of the solid structure material; and that the scattering phase function does not depend on the reflectivity of the solid

structure surface, but on the combination of the surface reflection, interface refraction and volumetric radiation propagation inside the solid structure. Similar results are presented in the work of Parthasarathy et al. [23], where they concluded that the extinction coefficient increases with decreasing porosity for the same pore density and that the scattering phase function is independent of the structural properties of the porous media (porosity and pores density). Cunsolo et al. [25] conducted a similar study, but they focused only on the extinction coefficient, where a new correlation for the extinction coefficient is proposed. Regarding to experimental studies, a commonly used method is measuring separately the hemispherical total reflectance and hemispherical diffuse reflectance (specular reflection is not accounted) [26], or even measurement of both reflectance and transmittance [27]. For example, in the work of Baillis et al. [27] the spectral radiative properties of polyurethane foam are estimated through measurements of hemispherical and bi-directional reflectance and transmittance using integrating spheres. They found that combining the hemispherical and bi-directional measurements is better to predict radiative parameters than only bi-directional measurements. Another important radiative property of porous media is the emissivity of the material of the solid structure. Experimental techniques have been used to obtain this property, as for example the one described in the work of Ravindra et al. [28], where an overview of spectral emissivity measurements is presented, and in the work of Balat-Pichelin and Bousquet [29], where measurements of directional and hemispherical emissivity are reported.

The scattering phase function is one of the most important radiative properties that affects the propagation and absorption of solar radiation in porous media. For example, the recent work of Zhao et al. [30] presents the effect of using different phase functions on the determination of thermal and radiative properties of ceramic foams made of Al_2O_3 through an inverse numerical method combined with experimental measurements. They showed that all the studied phase functions can be successfuly used to estimate the thermal properties, but the linear anisotropic scattering phase functions are more accurate for the prediction of radiative properties. Regarding the determination of scattering phase functions, the effect of different function forms on the modelling of near ultraviolet radiation propagation and absorption in photocatalytic reactors using the MCRT method is reported in the work of Hou et al. [31]. They compared numerical results against experimental measurements in order to determine which phase function presents the best fit. Among the investigated functions, best results were obtained using the Henyey–Greenstein (HG) phase function [32] with an asymmetry factor in the range of 0.5 to 0.7. The work of Petrasch et al. [33] presents the determination of the scattering phase function by modelling a 3D ceramic foam structure through a MCRT method. They found that scattering in the ceramic foam is more backwards, with a weaker forward component

than for the case of a large spherical particles packaging. The spectral dependence of the radiative properties was studied by Hendricks and Howell [22] through an inverse analysis technique, in which a radiative transfer model is combined with measurements of spectral hemispherical reflectance and transmittance of different samples of open-cell ceramic foams. They estimated the spectral absorption and scattering coefficients and scattering phase function in the range of 0.4 to 5.0μm. They also investigated the effect of using different phase functions in the estimation of the radiative properties, with the Henyey-Greenstein phase function showing better results. Other phase functions have been studied, as for example, in the work of Tseng et al. [34], which presents the radiative properties of open-cell SiC foam in the infra-red spectrum based on the Mie scattering theory, and where it was found that the forward scattering is predominant in this spectral range.

Previous works show that the phase function plays a crucial role in the modelling of radiation propagation in porous media and that it is one of the most difficult radiative properties to estimate. Among all the commonly investigated phase functions, the Heney-Greentein phase function is one of the most extensively studied because it is easily parameterised to simulate different scattering conditions by adjusting only one parameter, the asymmetry factor. However, the literature shows a gap in the determination of the asymmetry factor of the Heney-Greentein phase function when it is used for modelling solar radiation propagarion and absorption in porous volumetric receivers [15]. To contribute to fill this gap, in this work an experimental study and a numerical model are combined aiming to estimate the asymmetry factor of the Heney-Greentein scattering phase function for modelling porous volumetric receivers coupled to solar concentration systems. To that end, the hemispherical diffuse reflectance of different samples of open-cell SiC ceramic foam is measured and then the asymmetry factor in the numerical model was adjusted to minimize the difference between measured and simulated values of reflectance. For the numerical model, an in-house three-dimensional Monte Carlo Ray Tracing method was used to model the radiation propagation in porous media for the same experimental conditions, and considering the continuous-scale approach of the porous media.

4.2 Experimental apparatus and procedure

In the following, the experimental apparatus and procedures to obtain the porosity, pores size and diffuse reflectance of five samples of open-cell ceramic foam with different pores densities are presented. The samples used in this work (Fig. 4.1) were provided by LANIK ceramic foam company [35], which manufactures these pieces as filters of molten metal for metallurgical industry. The samples are cylindrical with a height of $H = 5$ cm, a diameter of $D_s = 6.35$ cm and pores densities of 20, 25,

30, 40 and 60 PPI (pores per inch). The chemical composition of the solid matrix structure is $65 \pm 6.5\%$ of silicon carbide (SiC), $15 \pm 1.5\%$ of aluminium oxide (Al_2O_3) and $20 \pm 2.0\%$ of silicon dioxide (SiO_2).

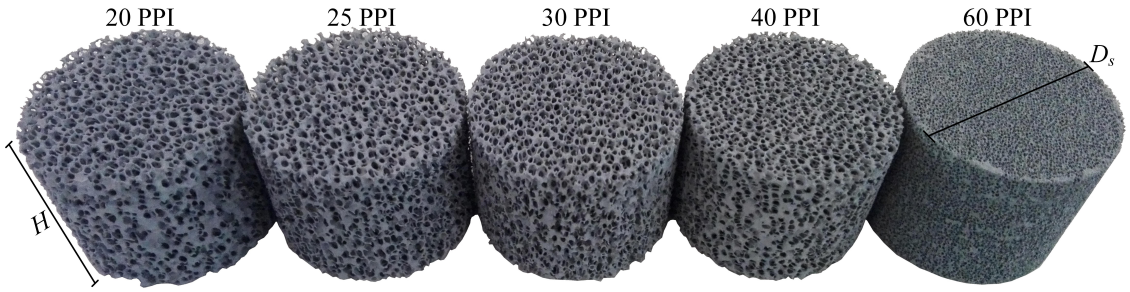

Fig. 4.1: Open-cell SiC ceramic foam used in the experimental measurements.

4.2.1 Porosity

In this study, it is more useful to have the porosity ϕ in terms of fraction of void space in relation to the external volume of the sample, instead of having pores density in PPI. For this purpose, the following relation is used to obtain the porosity:

$$\phi = 1 - \frac{m}{\rho V} \tag{4.1}$$

where m is the mass of the sample, V is the (total) volume based on the external dimensions of the sample and ρ is the apparent density (bulk density) of the ceramic body. The density is provided by the manufacturer, which is $\rho = 2.35 \pm 0.118$ g cm^{-3}. The mass of each sample was measured using a high precision scale (errors less than 0.01 g). The obtained porosities and respective uncertainties are presented in Table 4.1.

Table 4.1: Porosity of the samples.

PPI	ϕ (%)
20	85.63±0.73
25	83.44±0.84
30	85.48±0.74
40	85.60±0.73
60	88.18±0.60

It should be noted that the material itself is also porous, with a porosity around 21% (having a very small pore scale compared to the foam pore size), which was neglected when determining density ρ and porosity ϕ, since almost all micropores are closed (not contributing to radiation propagation).

4.2.2 Pores size

Other two important parameters of porous media are the pores size and pores geometry. The pores can have different shapes and sizes, which becomes difficult to characterize. Fig. 4.2 shows an example of how the pores can slightly change in size and geometry in one of the faces of a 20 PPI sample. There are some pores non-homogeneity near the sample surface, which effect is discussed in Section 4.2.4. According to the data provided by the manufacturer, depending on the pores density, the pore sizes (cross-section at the middle of the pores (cells)) may vary between a minimum (d_p^-) and a maximum (d_p^+) value. These values are presented in Table 4.2 for the five samples used.

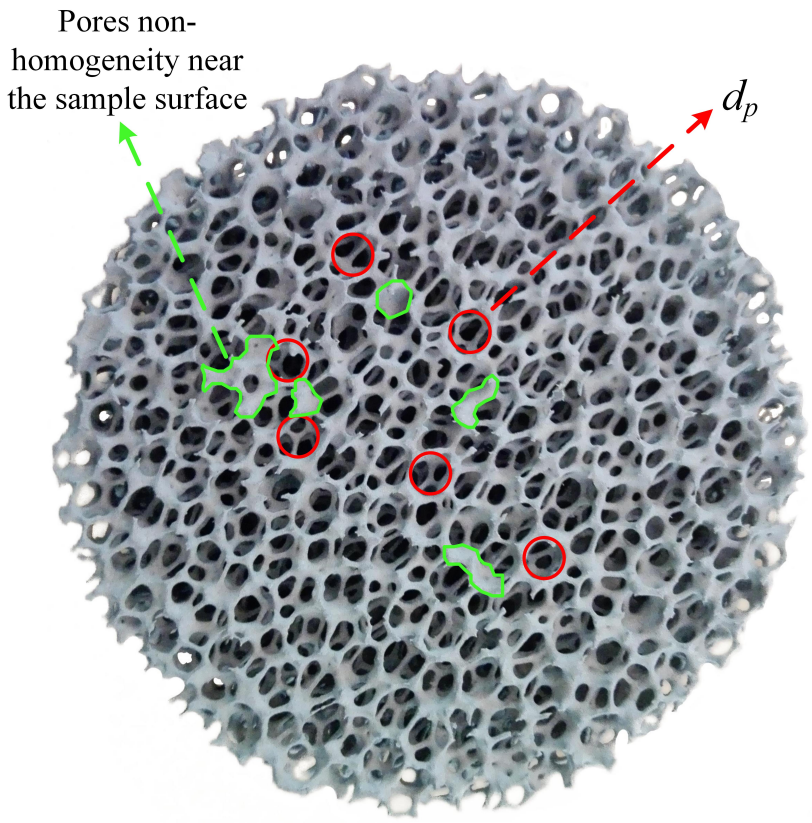

Fig. 4.2: Pores size, geometry and non-homogeneity near the face of the 20 PPI sample.

In this work, it is considered that the pores are spherical, and a mean pores diameter d_p is used. The mean pores diameter is calculated from the minimum and maximum pores size shown in Table 4.2. To obtain the uncertainty of the mean pores diameter, it is considered that the pores size in the samples follow a normal distribution, and then the uncertainty is assumed as being the standard deviation of that distribution. To calculate the standard deviation, it is considered an interval of confidence of four times the standard deviation, in which 99.994% of the pores sizes are included in the interval between the minimum and maximum values of

Table 4.2: Minimum, maximum and mean pores size of the samples.

PPI	d_p^- (mm)	d_p^+ (mm)	d_p (mm)
20	2.890	3.893	3.391±0.125
25	2.496	3.376	2.936±0.110
30	2.200	2.948	2.574±0.094
40	1.699	2.201	1.950±0.063
60	1.046	1.236	1.141±0.024

pores diameter. Therefore, the standard deviation is calculated by dividing half of that interval by four. The values of mean pores diameter and the corresponding uncertainties obtained through this assumption are also presented in Table 4.2.

Beyond spherical geometry, other approaches, such as, tetrakaidecahedral [36] and dodecahedral [37] geometries are being considered. To have an equivalent representation of the geometry of the pores when the diffent approaches are used, a correction factor is normally applied to the mean pores size aiming to represent the same fixed volume of the pores [16]. For example, in the work of Li et al. [16] a correction factor of 1.08 was applied to a diameter of spherical pores in order to represent dodecahedral pores. Considering the pores as spherical and using the approach described above to calculate the mean pores diameter and the uncertainties is a good approximation to characterise the geometry of the pores.

4.2.3 Diffuse reflectance

If a light beam hits on one of the faces of the porous media it can be immediately reflected or absorbed or it can enter the porous media and then either scattered or absorbed. Also, some amount of the light scattered inside the porous media will exit through the irradiated face of the sample, with the diffuse reflectance R_s being defined as the ratio between the intensity coming out from that face and the total incident light intensity. In this work, an integrating sphere is used to meassure the diffuse reflectance. There are two main methods to measure diffuse reflectance with integrating spheres, which are the comparison method and substitution method [38]. In both methods, a calibrated reference with a known diffuse reflectance R_r is needed. The substitution method has been adopted due to its higher accuracy for the integrating sphere configuration of the present experimental apparatus. Fig. 4.3(a) shows the schematic of the integrating sphere setup. Two measurements are needed, one using the calibrated reference and the other using the sample instead of the reference. It should be noted that the cross-section area of the samples are higher than the area of the port of the integrating sphere. For this reason, what it is really measured is a diffuse reflectance R_s^* different of the total diffuse reflectance R_s because

not all the scattered light coming out from the sample enters into the integrating sphere and is detected by the detector (Fig. 4.3(b)). The diffuse reflectance of the sample is obtained through the simplified form of the equation from the work of Hwang et al. [38] as follow:

$$\frac{L_s - L_0}{L_r - L_0} = \frac{R_s^*}{R_r}\left(\frac{1 - \overline{R_r}}{1 - \overline{R_s^*}}\right) \tag{4.2}$$

where L_s and L_r are the intensities measured by the detector when the sample and reference are placed in the port of the integrating sphere, respectively. L_0 is the intensity measured with the light source switched on and placing a light trap in the sample/reference port. $\overline{R_r}$ and $\overline{R_s^*}$ are average reflectances of the surface of the integrating sphere when the reference and the sample are used, respectively. These average values are calculated as follow:

$$\overline{R_r} = \frac{R_i A_i + A_p(R_r + R_d + R_l)}{A_i + 3A_p} \tag{4.3}$$

$$\overline{R_s^*} = \frac{R_i A_i + A_p(R_s^* + R_d + R_l)}{A_i + 3A_p} \tag{4.4}$$

where A_i is the area of the inner surface of the integrating sphere excluding the ports, and A_p is the area of each port. All the three ports (light source, detector and sample/reference) have the same area. R_i, R_d and R_l are the diffuse reflectances of the surface of the integrating sphere, detector and light source, respectively. These reflectance values and the diameters of the integrating sphere, D_i, and ports, D_p, are presented in Table 4.3. The only unknown in Eq. (4.2) to (4.4) is the reflectance of the sample, R_s^*, which is obtained by solving Eq. (4.2).

Fig. 4.4 shows the experimental apparatus used to meassure the diffuse reflectance (total hemispherical reflectance), where the main components are identified. A stabilised light source with a quartz halogen lamp with a color temperature of 3200 K is used with a fiber optic illuminator and a light guide coupled to a focusing lens, which produces a collimated light beam with a divergence angle lower than 4.5°. For the detector, a high precision silicon photodetector with a spectral response between 200 and 1100 nm is used. The reference diffuse reflectances are calibrated materials from SphereOptics [39] (detailed information is provided in Section 4.2.5).

It is also possible to measure diffuse transmittance with the integrating sphere, but for the ranges of height, porosity and mean pores size of the samples, the diffuse transmittance is approximately zero.

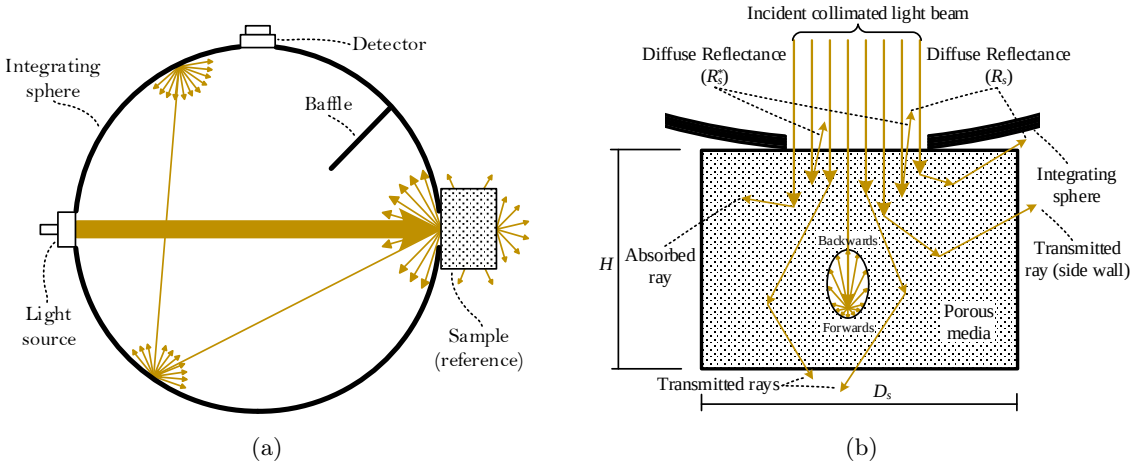

Fig. 4.3: Diffuse reflectane measurement: (a) Substitution method with integrating sphere; (b) Propagation of light in porous sample and fraction of diffuse light captured by the sphere.

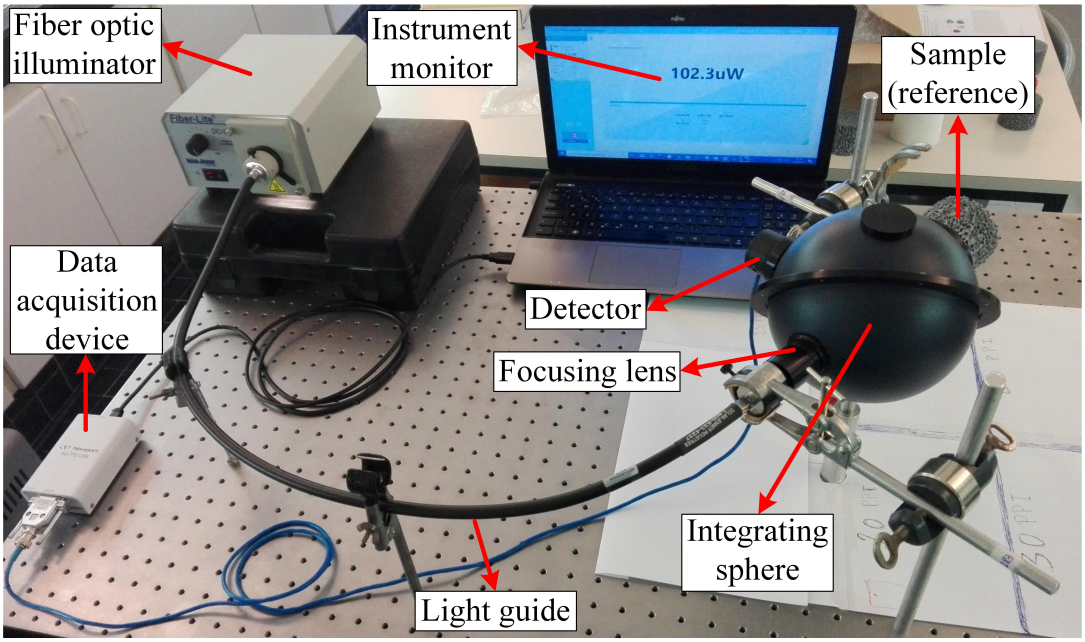

Fig. 4.4: Experimental apparatus used to measure the diffuse reflectance of SiC samples.

Table 4.3: Geometric and optical properties of the integrating sphere.

Parameter	Value
R_i	97%
R_d	0.0%
R_l	0.0%
D_i (cm)	15.24
D_p (cm)	2.54

4.2.4 Main sources of error in measurements

There are different sources of error in the present experimental study, which can be divided in two types. The first type of errors are associated with measurements of the geometric parameters of the porous structure (porosity and pores size) and the other are errors associated with the diffuse reflectance measurements. Regarding the geometric parameters, the main source of error is in the determination of pores size because the porous media is not homogeneous, thus making difficult to quantify a mean pores size. Therefore, the main source of error is the assumption that pores are spherical with a mean pores diameter that characterize them.

Regarding the diffuse reflectance measurements, the main source of error is in the faces of the samples, where the pores size can be slightly smaller than the pores size inside the sample, which causes a local non-homogeneity of the porous structure near these surfaces that results from the fabrication process. This type of non-homogeneities, which is identified in Fig. 4.2 in the 20 PPI sample, can make the measured diffuse reflectance to be slightly higher than the reflectance of a homogeneous sample. To minimise this problem, several measurements were taken for each sample, turning or slightly shifting the sample laterally from its previous position on the port of the sphere between each measurement. The mean value of measurements is then used for subsequent calculations. The uncertainties associated to the equipments and procedure also affect the measurements, however these errors are minimal, as is discussed in Section 4.2.5. The experiment was performed under dark conditions to minimize any possible error due to external radiation.

4.2.5 Validation and optimisation of the experimental procedure

The reflectance of the samples are measured using two calibrated diffuse reflectance standards from SphereOptics company [39]. These references are calibrated in the wavelength range between 250 and 2450 nm in steps of 1 nm, with a nearly constant spectral response in that range. Although the variation of the reflectance of references is small in the spectral range of solar radiation, a validation and optimization process of the experimental procedure was done by using the calibrated reference A to measure the reflectance of the calibrated reference B and vice versa. In this process, it was found that the difference between measured and calibration mean values of reflectance of both the references is less than 0.03% in the spectral range of 400 to 1049 nm, which is close to the spectrum of the lamp used in the illuminator (not considering the infrared radiation, which is not measured by the detector) and is centred in the solar spectral range. The obtained mean values of reflectance are 12.83% and 25.99% for the references A and B, respectively, which are the values used in the determination of the diffuse reflectance of the porous samples. With this

error magnitude found in the cross-validation between the two references, it can be considered that the experimental apparatus and procedure allow measuring the diffuse reflectance with high accuracy. These references were chosen because their diffuse reflectances are close to the expected reflectance of the porous samples.

4.3 Numerical modelling

The propagation of radiation in the porous structure of the solar receiver element (sample) was numerically modelled to simulate the experimental conditions and, with that, to validate and tune the model by determining the optimal asymmetry factor of the phase function for which the numerical results fit better to the measurements. The model is based in the work of Barreto et al. [15], which was validated with results from the work of van de Hulst [40]. The MCRT method consists in dividing the incident collimated light beam into a large number of small equal amounts of energy, called rays, and then trace their paths until they are absorbed or leave the porous media [15]. The rays interact with the structure either by absorption or scattering processes. If absorbed, the location of absorption will be the final position of the rays, and if scattered a new direction is determined through a scattering phase function. More details on the propagation and absorption processes modelling can be found in the work of Barreto et al. [15]. Fig. 4.3(b) schematically shows several possible ray paths that can be obtained from the MCRT method for the experimental setup conditions. The porous media is characterized by the absorption coefficient κ_a, scattering coefficient κ_s and extinction coefficient β, which can be expressed as follow [41]:

$$\kappa_a = 1.5\varepsilon(1-\phi)/d_p \tag{4.5}$$

$$\kappa_s = 1.5(2-\varepsilon)(1-\phi)/d_p \tag{4.6}$$

$$\beta = \kappa_a + \kappa_s = 3(1-\phi)/d_p \tag{4.7}$$

where ε is the emissivity of the material, ϕ is the porosity and d_p is the mean pores diameter. When the rays enter in the receiver, their path lengths l_β are computed using [42]:

$$l_\beta = -\frac{1}{\beta}\ln\xi \tag{4.8}$$

where ξ is a random number evenly distributed between 0 and 1. To decide if a given ray is absorbed or scattered, another random number ξ is generated and the following condition is used:

$\xi \leqslant \omega$, scattering

$\xi > \omega$, absorption

where ω is the scattering albedo defined as:

$$\omega = \frac{\kappa_s}{\beta} = \frac{2-\varepsilon}{2} \tag{4.9}$$

According to the geometric optics approximations used [43] and the work of Cunsolo et al. [44], the estimation of the absorption and scattering coefficients through Eq. (4.5) and Eq. (4.6) is a good approximation because the size of the ligaments (bridges) in the porous structure is much larger than the wavelengths of the incident light.

4.3.1 Scattering phase function

When rays are scattered in the porous media, a phase function is needed to compute the new direction of travelling of each ray. Several scattering phase functions have been proposed in the literature. The Henyey-Greenstein (HG) phase function [32] is used in this work because it can be easily adjusted to simulate different scattering conditions. This phase function (Φ_{HG}) is defined as:

$$\Phi_{HG}(\theta) = \frac{1}{4\pi}\frac{1-g^2}{(1+g^2-2g\cos\theta)^{3/2}} \tag{4.10}$$

where θ is the polar angle of scattering and g is the asymmetry factor, which is defined as the mean cosine of the polar angles of scattering. The asymmetry factor varies between -1 and 1, with -1 being used in the case of full backscattering, 1 is for full forward scattering and 0 for a uniform distribution [32].

Another example of phase function is from the work of Howell et al. [45], which is used in this work for comparison only. This phase function (Φ_H), which has an asymmetry $g = -0.444$ (mean cosine of the scattering angles), was obtained by modelling a packing of spheres with diffuse reflection surface, and it is described as:

$$\Phi_H(\theta) = \frac{8}{3\pi}(\sin\theta - \theta\cos\theta) \tag{4.11}$$

4.3.2 Diffuse reflectance

In the MCRT method, the diffuse reflectance R_s is defined as the ratio between the number of rays that leave the porous media through the front face (N_{of}) and the total number of incident rays (N_T) on that face. However, to adjust the numerical model to the experimental setup, a diffuse reflectance R_s^* should be considered, defined as the ratio between the number of rays that leave the porous media through the area that corresponds to port aperture of the integrating sphere (N_{of}^*), and the total number of incident rays (Fig. 4.3(b)). These two quantities are given respectively by:

$$R_s = \frac{N_{of}}{N_T} \tag{4.12}$$

$$R_s^* = \frac{N_{of}^*}{N_T} \tag{4.13}$$

It is also possible to compute the diffuse transmittance by counting the number of rays that leave the porous media through the back face, however, because of the relation between the height of the samples, pores size and porosities, this value is minimal, and thus it was not compared against measurements in the present experimental setup.

4.4 Results and discussion

The main purpose of this work is to validate the MCRT method and estimate the asymmetry factor of the Henyey-Greenstein phase function by comparing experimental measurements with numerical results. To do that, the numerical model is adjusted to simulate the same experimental conditions. The only unknown is the asymmetry factor, which is determined here by tuning its value in the numerical model to minimize the difference between measured and simulated diffuse reflectances (R_s^*).

For the simulations, it is considered an incident collimated light beam (parallel rays) perpendicular to the front face of the sample, and that the side wall has an absorptivity equal to 1, which reproduce the experimental boundary condition when the light scapes to the environment through that wall. The emissivity of the foam material is $\varepsilon = 0.84$ [46], which corresponds to have a scattering albedo of $\omega = 0.58$, according to Eq. (4.9). A total number of rays of $N_T = 10^8$ is used in the MCRT method, which is enough to guarantee an accurate prediction of the diffuse reflectance [15].

Fig. 4.5 shows the measured and modelled diffuse reflectances for optical thicknesses ($b = H\beta$, with β being calculated according to Eq. (2.3)) of the five samples when different phase functions and asymmetry factors are used. The optical thickness is used here to represent the reflectance results because it accounts for all the geometric parameters of the porous media (height, porosity and pores size). The higher uncertainties in optical thickness (calculated through propagation of uncertainty theory) are mainly due to the uncertainties associated with the mean pores size (diameter). The asymmetry factor of the Henyey-Greenstein phase function that minimizes the differences between experimental and numerical results is $g = -0.25$ (backward scattering), with a mean bias error of MBE = 0.0045% and a root mean square error of RMSE=0.2926%. The phase function of Howell et al. (H) [45], Eq. (4.11), overpredicts the diffuse reflectance. In the literature, it is also used an isotropic scattering phase function (HG ($g = 0$)), however, in this work it was found that this function underpredicts the diffuse reflectance of open-cell ceramic foam, as shown in Fig. 4.5. Even in the case of the phase functions HG with $g = -0.444$ and H (also

with $g = -0.444$) having the same asymmetry, the respective diffuse reflectances are slightly different because the probability distributions of the scattering angle are also different. These probability distributions are presented in the polar plot of Fig. 4.6, which also includes the other scattering phase functions shown in Fig. 4.5.

Fig. 4.7 shows the two modelled diffuse reflectances, R_s and R_s^*, for different asymmetry factors of the HG function and optical thicknesses of the samples. The difference between the two reflectances is higher for lower values of optical thickness (higher porosities and pores size) because light propagates more deeply in the porous media and thus more light scapes from the samples outside the area of the port aperture of the integrating sphere.

Results show that the scattering of radiation in the visible spectrum in open-cell ceramic foam is slightly backwards, with an asymmetry when the Henyey-Greenstein phase function is used of $g = -0.25$. It should be noted that these results were obtained based on the integrated values of directional and spectral reflectance. To obtain a detailed description of the scattering phase function of open-cell ceramic foams, directional and spectral measurements of the diffuse reflectance are needed, which will allow to obtain the accurate probability distribution of the polar scattering angles.

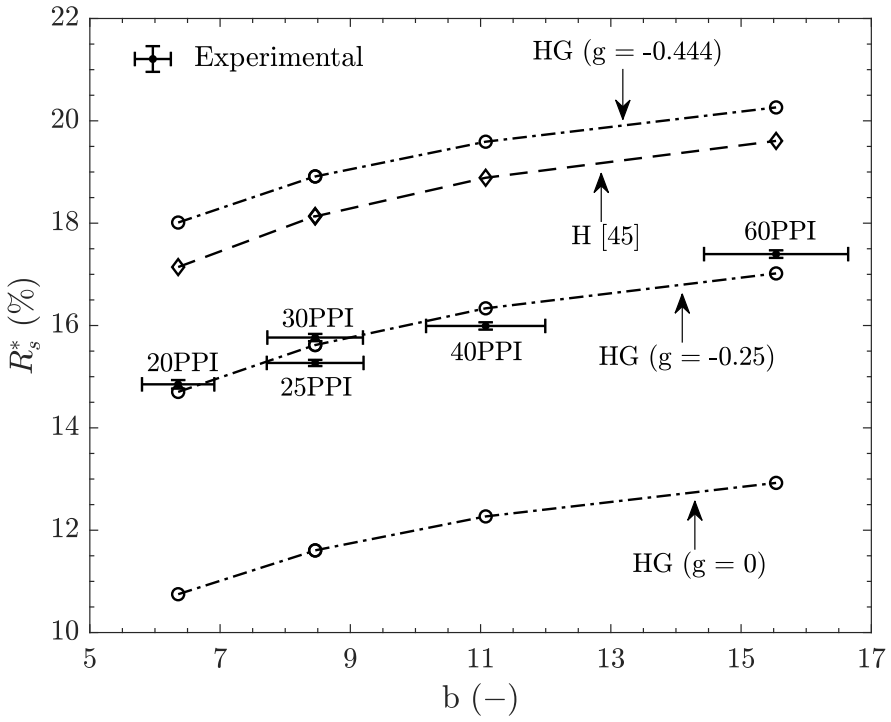

Fig. 4.5: Comparison between numerical and experimental results and determination of the asymmetry factor.

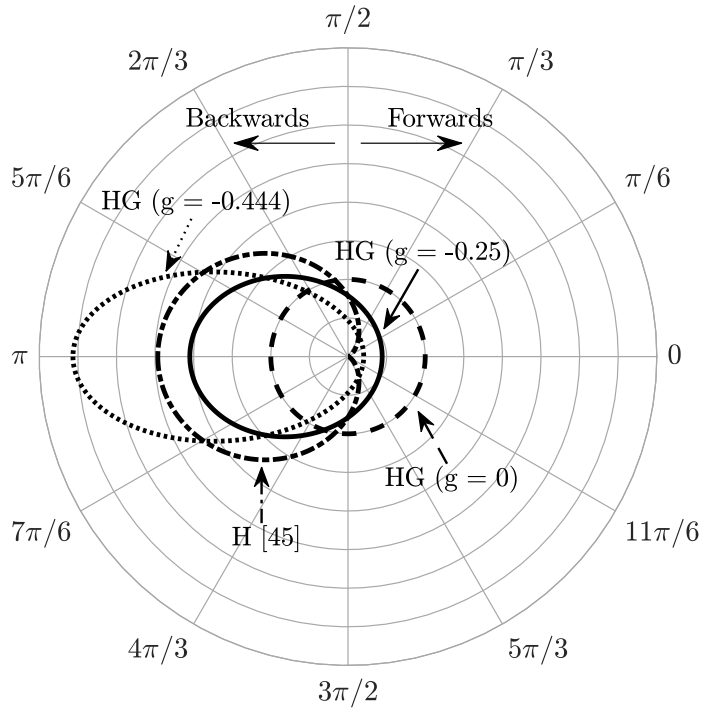

Fig. 4.6: Polar plot of the scattering phase functions.

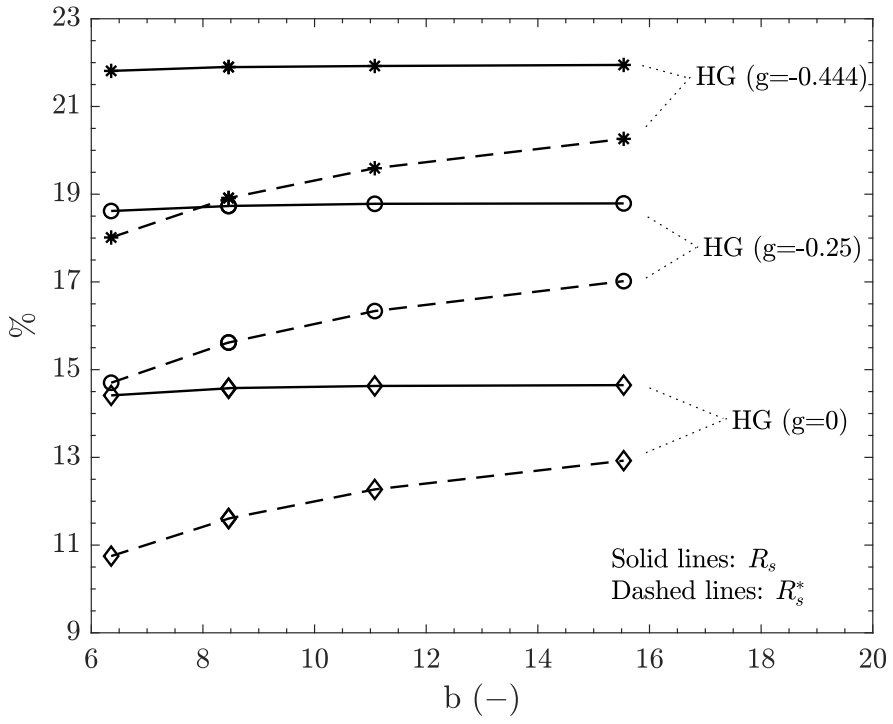

Fig. 4.7: Modelled diffuse reflectance (R_s and R_s^*) for different phase functions.

4.5 Conclusions

In this work, an experimental study and a numerical model are used aiming to determine the asymmetry factor of the Henyey-Greenstein (HG) scattering phase function of open-cell SiC ceramic foam in the visible spectral range. The hemispherical diffuse reflectance of five different samples with optical thicknesses ranging from approximately 6 to 16 was both measured and numerically modelled. Measurements were obtained through an experimental setup and procedure that include an integrating sphere and reference reflectances, while the numerical modelling was done through an in-house algorithm based on the three-dimensional Monte Carlo Ray Tracing (MCRT) method.

Results show that the radiation scattering in the visible spectrum in open-cell SiC ceramic foam is slightly backwards, with an asymmetry factor when the Henyey-Greenstein phase function is used of approximately -0.25. To obtain a detailed description of the scattering phase function of open-cell ceramic foams, directional and spectral measurements of the diffuse reflectance are needed. It was also found that the isotropic phase function underestimates the diffuse reflectance, while the phase function obtained through modelling of packing of spheres overpredicts the diffuse reflectance of open-cell SiC foams. The diffuse reflectance of open-cell SiC ceramic foam is about 16%, which directly affects the efficiency of porous volumetric receivers. Lower reflectances can be achieved by using or designing porous structures that provide more forward scattering, which can be obtained by changing the pores geometry and orientation, and by improving the optical properties of the porous material. Another method is to design the receiver inlet as a cavity for example, aiming at to absorb and redirect to the receiver some amount of the backscattered solar radiation.

This work contribute to fill the gap of knowledge in the asymmetry factor of Henyey-Greenstein phase function when it is used to model scattering of solar radiation in porous volumetric receivers coupled to concentration systems.

References

[1] M. A. Silva-Pérez. Solar power towers using supercritical CO_2 and supercritical steam cycles, and decoupled combined cycles. *Adv Conc Sol Therm Res Techno*, 383–402, 2017.

[2] C. K. Ho and B. D. Iverson. Review of high-temperature central receiver designs for concentrating solar power. *Renew Sust Energ Rev*, 29:835–846, 2014.

[3] M. Sedighi, R. V. Padilla, R. A. Taylor, M. Lake, I. Izadgoshasb, and A. Rose.

High-temperature, point-focus , pressurised gas-phase solar receivers: A comprehensive review. *Energ Convers Manage*, 185:678–717, 2019.

[4] A. L. Ávila-Marín. Volumetric receivers in Solar Thermal Power Plants with Central Receiver System technology: A review. *Sol Energy*, 85:891–910, 2011.

[5] G. Barreto, P. Canhoto, and M. Collares-Pereira. Three-dimensional CFD modelling and thermal performance analysis of porous volumetric receivers coupled to solar concentration systems. *Appl Energy*, 252:113433, 2019.

[6] J.-H. Eom, Y.-W. Kim, and S. Raju. Processing and properties of macroporous silicon carbide ceramics: A review. *J Asian Ceram Soc*, 1:220–242, 2013.

[7] F. Gomez-Garcia, J. González-Aguilar, G. Olalde, and M. Romero. Thermal and hydrodynamic behavior of ceramic volumetric absorbers for central receiver solar power plants: A review. *Renew Sust Energ Rev*, 57:648–658, 2016.

[8] Y. Li, X.-L. Xia, C. Sun, H.-P. Tan, and J. Wang. Pore-level numerical analysis of the infrared surface temperature of metallic foam. *J Quant Spectrosc Ra*, 200: 59–69, 2017.

[9] M. Samoilenko, P. Seers, P. Terriault, and V. Brailovski. Design, manufacture and testing of porous materials with ordered and random porosity: Application to porous medium burners. *Appl Therm En*, 158:113724, 2019.

[10] X. Liang, Y. Li, Z. He, Q. Wang, Y. Chen, X. Xu, B. Li, and C. G. Aneziris. Design of three-layered struts in SiC reticulated porous ceramics for porous burner. *Ceram Int*, 45:8571–8576, 2019.

[11] A. Sommers, Q. Wang, X. Han, C. T'Joen, Y. Park, and A. Jacobi. Ceramics and ceramic matrix composites for heat exchangers in advanced thermal systems–A review. *Appl Therm En*, 30:1277–1291, 2010.

[12] X. Chen, C. Sun, X. Xia, R. Liu, and F. Wang. Conjugated heat transfer analysis of a foam filled double pipe heat exchanger for high-temperature application. *Int J Heat Mass Tran*, 134:1003–1013, 2019.

[13] M. Emmel and C. G. Aneziris. Development of novel carbon bonded filter compositions for steel melt filtration. *Ceram Int*, 38:5165–5173, 2012.

[14] O. Dávila-Maldonado, A. Adams, L. Oliveira, B. Alquist, and R. D. Morales. Simulation of Fluid and Inclusions Dynamics during Filtration Operations of Ductile Iron Melts Using Foam Filters. *Metall Mater Tran B*, 39:818–839, 2008.

[15] G. Barreto, P. Canhoto, and M. Collares-Pereira. Three-dimensional modelling and analysis of solar radiation absorption in porous volumetric receivers. *Appl Energy*, 215:602–614, 2018.

[16] Y. Li, X.-L. Xia, C. Sun, S.-D. Zhang, and H.-P. Tan. Volumetric radiative properties of irregular open-cell foams made from semitransparent absorbing-scattering media. *J Quant Spectrosc Ra*, 224:325–342, 2019.

[17] O. Smirnova, T. Fend, R. Capuano, G. Feckler, P. Schwarzbözl, and F. Sutter. Determination of critical thermal loads in ceramic high concentration solar receivers. *Sol Energ Mat Sol C*, 176:196–203, 2018.

[18] S. Du, M.-J. Li, Q. Ren, Q. Liang, and Y.-L. He. Pore-scale numerical simulation of fully coupled heat transfer process in porous volumetric solar receiver. *Energy*, 140:1267–1275, 2017.

[19] X.-L. Xia, Y. Li, C. Sun, Q. Ai, and H.-P. Tan. Integrated simulation of continuous-scale and discrete-scale radiative transfer in metal foams. *J Quant Spectrosc Ra*, 212:128–138, 2018.

[20] Y. Li, X.-L. Xia, C. Sun, S.-D. Zhang, and H.-P. Tan. Integrated simulation of continuous-scale and discrete scale radiative transfer in an open-cell foam made of semitransparent absorbing scattering ceramics. *J Quant Spectrosc Ra*, 225: 156–165, 2019.

[21] A. L. Avila-Marin, J. Fernandez-Reche, and A. Martinez-Tarifa. Modelling strategies for porous structures as solar receivers in central receiver systems: A review. *Renew Sust Energ Rev*, 111:15–33, 2019.

[22] T. J. Hendricks and J. R. Howell. Absorption/Scattering Coefficients and Scattering Phase Functions in Reticulated Porous Ceramics. *J Heat Transfer*, 118:79–87, 1996.

[23] P. Parthasarathy, P. Habisreuther, and N. Zarzalis. Identification of radiative properties of reticulated ceramic porous inert media using ray tracing technique. *J Quant Spectrosc Ra*, 113:1961–1969, 2012.

[24] Y. Li, X.-L. Xia, C. Sun, J. Wang, and H.-P. Tan. Tomography-based radiative transfer analysis of an open-cell foam made of semitransparent alumina ceramics. *Sol Energ Mat Sol C*, 188:164–176, 2018.

[25] S. Cunsolo, R. Coquard, D. Baillis, W. K. S. Chiu, and N. Bianco. Radiative properties of irregular open cell solid foams. *Int J Therm Sci*, 117:77–89, 2017.

[26] T. Fend, G. Jorgensen, and H. Küster. Applicability of highly reflective aluminium coil for solar concentrators. *Sol Energy*, 68:361–370, 2000.

[27] D. Baillis, M. Arduini-Schuster, and J. F. Sacadura. Identification of spectral radiative properties of polyurethane foam from hemispherical and bi-directional transmittance and reflectance measurements. *J Quant Spectrosc Ra*, 73:361–370, 2002.

[28] N. M. Ravindra, B. Sopori, O. H. Gokce, S. X. Cheng, A. Shenoy, L. Jin, S. Abedrabbo, W. Chen, and Y. Zhang. Emissivity Measurements and Modeling of Silicon-Related Materials: An Overview. *Int J Thermophys*, 22:1593–1611, 2001.

[29] M. Balat-Pichelin and A. Bousquet. Total hemispherical emissivity of sintered SiC up to 1850 K in high vacuum and in air at different pressures. *J Eur Ceram Soc*, 38:3447–3456, 2018.

[30] S. Zhao, X. Sun, Q. Que, and W. Zhang. Influence of Scattering Phase Function on Estimated Thermal Properties of Al_2O_3 Ceramic Foams. *Int J Thermophys*, 40:11, 2019.

[31] J. Hou, Q. Wei, Y. Yang, and L. Zhao. Experimental evaluation of scattering phase function and optimization of radiation absorption in solar photocatalytic reactors. *Appl Therm En*, 127:302–311, 2017.

[32] L. G. Heney and J. L. Greenstein. Diffuse radiation in the Galaxy. *Astrophys*, J. 93:70–83, 1940.

[33] J. Petrasch, P. Wyss, and A. Steinfeld. Tomography-based Monte Carlo determination of radiative properties of reticulate porous ceramics. *J Quant Spectrosc Ra*, 105:180–197, 2007.

[34] C. C. Tseng, A. D. Swanson, R. Viskanta, R. L. Sikorski, and M. Chen. Effect of foam properties on radiative properties of open cell silicon carbide foams. *J Quant Spectrosc Ra*, 113:1503–1507, 2012.

[35] LANIK foam ceramics. www.lanik.eu/en, 2019.

[36] Z. Wu, C. Caliot, G. Flamant, and Z. Wang. Numerical simulation of convective heat transfer between air flow and ceramic foams to optimise volumetric solar air receiver performances. *Int J Heat Mass Tran*, 54:1527–1537, 2011.

[37] D. Baillis, R. Coquard, J. Randrianalisoa, L. Dombrovsky, and R. Viskanta. Thermal radiation properties of highly porous cellular foams. *Spec Top and Rev Porous Media: An Int J*, 4:111–136, 2013.

[38] J. Hwang, D.-J. Shin, and K. R. Jeong. Integrating sphere-based relative methods for reflection measurements. *Metrologia*, 53:1231–1242, 2016.

[39] SphereOptics. sphereoptics.de/, 2019.

[40] H. C. van de Hulst. *Multiple Light Scattering*, volume II. Academic Press, New York, 1980.

[41] K. Vafai. *Handbook of porous media*. Taylor and Francis, New York, second edition, 2005.

[42] M. F. Modest. *Radiative Heat Transfer*. Academic Press, New York, third edition, 2013.

[43] C.-L. Tien and B. L. Drolen. Thermal radiation in particulate media with dependent and independent scattering. *Annu Rev Heat Transf*, 1:1–32, 1987.

[44] S. Cunsolo, M. Oliviero, W. M. Harris, A. Andreozzi, N. Bianco, W. K. S. Chiu, and V. Naso. Monte Carlo determination of radiative properties of metal foams: Comparison between idealized and real cell structures. *Int J Therm Sci*, 87: 94–102, 2015.

[45] J. R. Howell, R. Siegel, and M. P. Menguc. *Thermal radiation heat transfer*. Taylor and Francis, New York, fifth edition, 2002.

[46] J. M. Jones, P. E. Mason, and A. Williams. A compilation of data on the radiant emissivity of some materials at high temperatures. *J Energy Inst*, 92:523–534, 2019.

Nomenclature

A	area (m^2)
b	optical thickness ($-$)
d_p	mean pores diameter (m)
D	diameter (m)
g	asymmetry factor of phase function ($-$)
H	height (m)
N	number of rays ($-$)
l_β	path length of rays (m)

L	power (W)
m	mass (kg)
R	diffuse reflectance $(-)$
V	volume (m^3)

Greek symbols

β	extinction coefficient (m^{-1})
ε	emissivity $(-)$
θ	scattering angle (rad)
κ_a	absorption coefficient (m^{-1})
κ_s	scattering coefficient (m^{-1})
ξ	random number uniformly distributed between 0 and 1 $(-)$
ρ	density (kg m^{-3})
ϕ	porosity $(-)$
Φ	phase function $(-)$
ω	scattering albedo $(-)$

Subscripts

0	offset
d	detector
HG	Henyey-Greenstein
i	integrating sphere
l	light source
of	front face
r	reference
s	sample
T	total

Chapter 5

Parametric analysis and optimisation of porous volumetric solar receivers made of open-cell SiC ceramic foam[†]

Abstract

In recent years, research on the usage of porous materials as volumetric thermal receivers in concentrated solar power (CSP) plants is growing significantly. This interest is due to their capabilities to improve the efficiency of solar radiation conversion into thermal energy. In this work, detailed parametric analysis and optimisation of the thermal and hydrodynamic performance of porous volumetric receivers are performed using a detailed numerical model. The transport and absorption of solar radiation is modelled through a Monte Carlo Ray Tracing algorithm, while the governing equations of fluid flow and heat transfer are solved using a Computational Fluid Dynamics model. The mean temperature of the fluid at the outlet, thermal efficiency and pressure drop across the receiver are investigated through a parametric analysis and optimisation for different values of porosity, pores size and inlet fluid velocity. The receiver of choice should have high thermal efficiency without greatly increasing the pressure drop and not decreasing the mean fluid temperature at the outlet. Results show that these conditions are achieved for receivers with high porosity $(0.8 - 0.9)$ and pores size $(4.5 - 3$ mm$)$. For a given receiver porosity, there is a pores size value that maximises thermal efficiency, being this value lower for high porosity.

Keywords: Solar energy; Volumetric receiver; Porous media; Thermal efficiency; Pressure drop; Optimisation.

[†]Germilly Barreto[(1)], P. Canhoto[(1)], and M. Collares-Pereira[(1)]. Parametric analysis and optimisation of porous volumetric solar receivers made of open-cell SiC ceramic foam. *Energy*, 200:117476, 2020.

[(1)] Institute of Earth Sciences, University of Évora.

5.1 Introduction

Concentrated solar power (CSP) plants are among the promising technologies to replace the conventional power plants based on fossil fuels, which are a source of greenhouse gases emission [1, 2]. For this reason, CSP systems are intensively studied nowadays, namely in terms of power plant design [3, 4], including the aspects concerning the energy storage [5]. In this context, the thermal receiver design and optimisation is drawing great attention since it is a crucial component of the system in which solar radiation is converted into thermal energy. Porous volumetric receivers are being proposed as a solution to improve the performance of CSP systems due to their capability to achieve high values of temperature and thermal efficiency [6, 7]. These receivers consist in a solid matrix structure where the concentrated solar radiation is absorbed, and where at the same time a heat transfer fluid (usually a gas) is forced to flow to be heated and subsequently used in a power cycle [8].

Porous volumetric receivers in CSP plants can be studied experimentally and numerically, with the numerical modelling approach being used more often for receiver design and optimisation [9]. Regarding receiver modelling, the following physical mechanisms should be considered: transport and absorption of solar radiation in the porous media, fluid flow and heat transfer phenomena [8]. Due to the complexity of these mechanisms, the porous media is usually modelled as a continuous semi-transparent medium, known as continuum-scale approach (CSA), and then the volume-averaged governing equations for local thermal non-equilibrium (LTNE) between the fluid and the solid matrix structure are solved [8]. Avila-Marin et al. [9] present a detailed description of modelling approaches used to study porous volumetric receivers in CSP plants. Their main conclusion was that the combination of CSA and numerical Computational Fluid Dynamics (CFD) techniques and the LTNE assumption is the most used approach. Barreto et al. [8] also used this strategy to develop a detailed three-dimensional model for a cylindrical receiver element made of silicon carbide (SiC) ceramic foam coupled to a parabolic dish. This model was then used to evaluate the receiver performance. Barreto et al. [10] developed a Monte Carlo Ray Tracing (MCRT) method to model the transport and absorption of solar radiation in the porous media, which is the most widely used technique to simulate these physical phenomena. Regarding experimental research on porous volumetric receivers, it is mainly related to the combination of theoretical models with experimental measurements in order to estimate radiative properties (extinction coefficient [11], scattering phase function [12] and emissivity [13]) and hydrodynamic properties (pressure drop) [14] of the porous media. Other works, such as measuring of temperature and thermal efficiency were also conducted aiming to validate numerical models, as presented by Wu et al. [15] and Wang et al. [16], for example.

The effect of geometric parameters (porosity and pores size) and working conditions on the absorbed solar radiation and temperature distribution is well established in literature [10, 8]. The work by Barreto et al. [10] presents a detailed parametric analysis of the distribution of absorbed solar radiation in porous volumetric receivers. They studied the effect of the extinction coefficient and of different concentration system configuration on the distribution of absorbed solar radiation, as well as the effect of optical thickness on the absorption efficiency. It was found that this distribution strongly depends on the geometric parameters, and that convergent incidence angles of solar radiation at the inlet of the receiver leads to high peaks of absorbed solar radiation. Regarding temperature distribution, the work by Barreto et al. [8] reports the effect of porosity, pores size and concentration system configuration on the distribution of fluid and solid phases temperature. Results show that hot spots are more often in receivers with high values of porosity and pores size and with convergent incidence angles of solar radiation at the receiver aperture.

Numerical models allow to find the optimal internal geometry (porosity and pores size) and working conditions (mass flow rate of heat transfer fluid and pressure drop) that maximise the receiver performance. Receivers optimisation is focused mainly on: (i) improvement of temperature distribution in the receiver in order to avoid hot spots [17, 18], which can damage the receiver material; and (ii) maximisation of thermal efficiency while keeping low fluid flow resistance [19, 20]. Different techniques can be used to optimise temperature distribution, such as, receivers with composite porous structure (different porosities) [17], receivers with gradual variation of porosity and pores size [18, 21], or even optimising the distribution of the concentrated solar radiation flux at the receiver inlet [8, 22]. For example, in the work of Chen et al. [17], a receiver with different porous structures is proposed and studied numerically. It was found that using materials with low porosity and small pores size close to the inlet at the side wall can reduce temperature gradient in the solid and increase the fluid temperature at the outlet. Another solution to avoid high-temperature gradients is, for example, that reported by Nimvari et al. [23], where non-uniform fluid velocity is imposed at the receiver inlet. This approach was compared with the case of uniform fluid velocity, and it was found that the proposed solution can reduce hot-spots in the solid.

Tao et al. [24] studied the effect of pores size and porosity distribution in the distribution of absorbed radiation and thermal performance of porous volumetric receivers. It was found that porous structure with pore-size-decreased and porosity-gradually-increased distributions have the best thermal performance. In the work of Zaversky et al. [20], a 1-D numerical and experimental evaluation of single-layer and multi-layer configurations of a porous volumetric receiver are investigated. A parametric analysis was conducted, and then the thermal efficiency was optimised.

They found that increasing the receiver porosity leads to higher thermal efficiency. The literature shows that the higher energy losses of the receiver are through diffuse reflectance at the front face [12, 25], which directly affects the thermal efficiency. To decrease the reflectance, Zhu and Xuan [25] proposed and investigated a receiver with three different layers of porous structure aiming to increase the radiation depth. They found that the proposed configuration can increase the thermal efficiency up to 87%. Regarding works focused only on the optimisation of thermal and hydrodynamic performances, in the work by Du et al. [19] a genetic algorithm was coupled to a numerical model of a porous volumetric receiver in order to find receiver configurations that maximise the thermal efficiency and keep low fluid flow resistance. Their numerical model is based on the volume averaging and local thermal non-equilibrium approaches, and they found that larger porosity and higher inlet velocity improve the thermal efficiency of the receiver. It was also found that the optimum pores size increases with increasing receiver thickness and decreasing fluid velocity at the inlet.

The study of thermal performance of porous volumetric receivers is mainly focused on the temperature distribution in the receiver. However, few works with a detailed parametric analysis and optimisation of the thermal (efficiency and fluid temperature at the outlet) and hydrodynamic (pressure drop) performances are found in literature. Improving temperature distribution in the receiver is important to prevent the existence of hot spots, which will increase the durability and stability of the materials. However, the thermal efficiency, mean fluid temperature and pressure drop across the receiver are also important parameters that quantify the receiver performance. In this work, a detailed three-dimensional model is used to study the effect of geometric parameters (porosity and pores size) and fluid flow conditions (fluid velocity at the receiver inlet) on the thermal efficiency, mean fluid temperature and pressure drop. The numerical model is based on previous validated works, and it consists in coupling a MCRT method, which models the propagation and absorption of solar radiation in the receiver, and a CFD model using the CSA and LTNE approaches to simulate fluid flow and heat transfer processes. The effect of varying only one or a combination of different geometric parameters and fluid flow conditions is investigated. Then, a discussion on the receiver optimisation is presented in order to maximise the thermal performance while keeping a low resistance to the fluid flow.

5.2 Numerical modelling

In this work, a cylindrical porous volumetric receiver using open-cell silicon carbide (SiC) ceramic foam as absorber is considered, with a radius r_{rec} and height L. The receiver element is shown in Fig. 5.1(a), while Fig. 5.1(b) shows schematically

the physical phenomena that occur during its operation [8]. A parabolic dish was considered to generate the concentrated solar radiation flux at the receiver aperture using the ray tracing software Tonatiuh [10, 26]. The concentration factor, focal distance and reflectivity were set to $C = 500$, $f = 70$ cm and $\rho_{dis} = 0.95$, respectively, while the distance between the receiver aperture and the focal point of the dish was set to $d_f = 2.25$ cm [10]. The concentrated solar flux was simulated for a direct normal irradiance of $DNI = 800$ W m^{-2} and a circumsolar ratio of $CSR = 2\%$, which is a representative value of clear sky conditions [27, 28]. The circumsolar ratio (CSR) is defined as the ratio between the integrated sky radiance in the circumsolar region (solid angle between sun radius and an aperture half-angle of 2.5°) and the integrated sky radiance between the sun axis and the aperture angle, that is, the direct normal irradiance which includes the direct beam from the sun disk and the circumsolar irradiance [27].

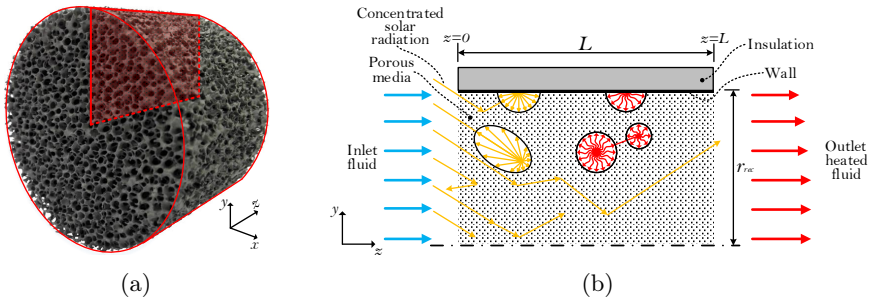

Fig. 5.1: Single element of porous volumetric receiver: (a) open-cell SiC ceramic foam (b) solar radiation propagation and absorption, fluid flow and heat transfer mechanisms [8].

5.2.1 *Transport and absorption of solar radiation in the receiver element*

The heat source of the thermal receiver is the absorbed solar radiation in the solid matrix. In this work, the transport process due to the scattering of solar radiation and its absorption is modelled using the Monte Carlo Ray Tracing (MCRT) method [10]. The algorithm is based on the continuum-scale approach (CSA) of the porous media and consists in tracing the path of a large number of solar rays until they are absorbed or leave the receiver. The path length, l_β, is calculated using [29]:

$$l_\beta = -\frac{1}{\beta} \ln \xi \tag{5.1}$$

where ξ is a random number uniformly distributed between 0 and 1 and β is the extinction coefficient. Then, to sort the rays that will be absorbed or scattered, a new random number ξ is generated. If this random number is higher than the scattering albedo $\omega = \kappa_s/\beta$ it means that the ray is absorbed. If the ray is scattered ($\xi \leqslant \omega$),

the Heney-Greenstein phase function $\Phi_{HG}(\theta)$ [30] is used to determine the scattering angle θ:

$$\Phi_{HG}(\theta) = \frac{1}{4\pi} \frac{1 - g^2}{(1 + g^2 - 2g\cos\theta)^{3/2}} \tag{5.2}$$

in which g is the asymmetry factor. This parameter can be adjusted to simulate different scattering patterns.

The extinction coefficient is determined as a function of the absorption κ_a and scattering κ_s coefficients, porosity ϕ and pores diameter d_p, in the following way [10]:

$$\kappa_a = 1.5\varepsilon(1 - \phi)/d_p \tag{5.3}$$

$$\kappa_s = 1.5(2 - \varepsilon)(1 - \phi)/d_p \tag{5.4}$$

$$\beta = \kappa_a + \kappa_s = 3(1 - \phi)/d_p \tag{5.5}$$

where ε is the emissivity of the solid structure.

The absorbed solar radiation distribution $Q_{solar} = N_{ev}e/V_{ev}$ is then obtained though a ray counting process in the mesh of the CFD model [8], in which N_{ev} and V_{ev} are the total number of rays and volume of each cell, respectively, and e is power per ray [8].

5.2.2 Fluid flow and heat transfer in the porous media

The steady-state macroscopic three-dimensional continuity and momentum equations are solved to model fluid flow and heat transfer, which can be expressed, respectively, as [8]
Continuity equation:

$$\nabla \cdot (\rho_f \vec{U}) = 0 \tag{5.6}$$

Momentum equation:

$$\frac{1}{\phi}\nabla\left(\rho_f \frac{\vec{U} \cdot \vec{U}}{\phi}\right) = -\nabla p + \nabla \cdot \left(\frac{\mu_f}{\phi}\nabla\vec{U}\right) + \vec{M}_s \tag{5.7}$$

$\vec{U}$ stands for the superficial velocity ($\vec{U} = \phi\vec{u}$, with $\vec{u}$ representing the mean fluid velocity in the pores), ρ_f and μ_f are the density and dynamic viscosity of the fluid, respectively, and p stands for pressure. To account for the effect of the porous media on the fluid flow, a momentum source term $\vec{M}_s$ is used through a correlation following the Darcy–Forchheimer model [14]. The working gas (air) is assumed as ideal, with its density being calculated through the equation of state and the viscosity through the Sutherland law [31].

The local thermal non-equilibrium (LTNE) approach, is used to model heat transfer, which results in the following energy equations for the solid matrix structure and heat transfer fluid, respectively:
Solid matrix structure:

$$0 = \nabla \cdot (\lambda_{se} \nabla T_s) + h_v (T_f - T_s) + Q_{ir} + Q_{solar} \tag{5.8}$$

Heat transfer fluid:

$$\nabla \cdot (\rho_f c_p \vec{U} T_f) = \nabla \cdot (\lambda_{fe} \nabla T_f) + h_v (T_s - T_f) \tag{5.9}$$

λ_{se} and λ_{fe} stand for the solid and fluid thermal conductivities [32, 33], respectively. h_v is the volumetric heat transfer coefficient [34], T_s and T_f are the temperature of the solid and fluid phases, respectively, and Q_{ir} and Q_{solar} are the heat source terms due to the thermal radiation exchange and solar radiation absorption in the solid, respectively. The specific heat capacity of the fluid c_p is calculated using a polynomial form available in the literature [15].

Thermal radiation exchange is modelled through the P1 approximation of the spherical harmonics method as follows [29]:

$$-\nabla \cdot \left(\frac{1}{3\beta} \nabla G \right) = \kappa_a \left(4\sigma T_s^4 - G \right) \tag{5.10}$$

where G is the (thermal) irrandiance and σ is the constant of Stefan Boltzmann, and with the heat source term due to the thermal radiation exchange being calculated through $Q_{ir} = -\kappa_a \left(4\sigma T_s^4 - G \right)$.

5.2.3 Boundary conditions

There are three boundary patches in the receiver element, which are inlet, outlet and the side wall. For the inlet, the fluid velocity $\vec{U}_{in}$ and temperature T_{in} are specified and a zero pressure gradient is imposed. The thermal radiation exchange between the solid surface and the environment is also considered, while the diffuse reflection losses of solar radiation (backscattering) are accounted in the MCRT method. For the outlet, the fully developed conditions for the fluid velocity and temperature are used, and a pressure value p_{out} is specified. The thermal radiation exchange between the solid surface and the environment at outlet is also considered, while the losses due to the solar radiation transmission are accounted in the MCRT method [10]. The wall is considered as adiabatic and ideal diffuse reflecting surface, and the no-slip condition for the fluid is used [8].

5.2.4 Thermal and hydrodynamic performance of the receiver

The developed numerical model can be used to study thermal and hydrodynamic performances of the porous volumetric receiver element with different internal geometries and for different working conditions. Thermal and hydrodynamic performances can be assessed through the heat extracted by the fluid P_f, thermal efficiency η_{th}, bulk fluid temperature at the outlet $\overline{T}_f$ and pressure drop Δp. These quantities are expressed, respectively, as follow:

$$\begin{aligned} P_f &= \dot{m} \int_{T_{in}}^{\overline{T}_f} c_p dT \\ &\approx \overbrace{\int_A \rho_f |\vec{U}| c_p T_f dA}^{outlet} - \overbrace{\int_A \rho_f |\vec{U}| c_p T_{in} dA}^{inlet} \end{aligned} \tag{5.11}$$

$$\eta_{th} = \frac{P_f}{P_{in}} \tag{5.12}$$

$$\overline{T}_f = \frac{\int_A \rho_f |\vec{U}| \langle c_p^{T_f} \rangle T_f dA}{\int_A \rho_f |\vec{U}| \langle c_p^{\overline{T}_f} \rangle dA} \approx \frac{\int_A \rho_f |\vec{U}| c_p T_f dA}{\int_A \rho_f |\vec{U}| c_p dA} \tag{5.13}$$

$$\Delta p = \frac{\int_{A_{in}} p dA}{\pi r_{rec}^2} - p_{out} \tag{5.14}$$

where $\dot{m} = \int_A \rho_f |\vec{U}| dA$ (either at inlet or outlet areas) is the mass flow rate through the receiver, P_{in} is the incident concentrated solar radiation, which is obtained through the MCRT method of the Tonatiuh software. $\langle c_p^{T_f} \rangle = \int_{T_{in}}^{T_f} c_p dT / (T_f - T_{in})$ and $\langle c_p^{\overline{T}_f} \rangle = \int_{T_{in}}^{\overline{T}_f} c_p dT / (\overline{T}_f - T_{in})$ are the mean specific heat capacities between T_{in} and T_f and between T_{in} and $\overline{T}_f$, respectively. The extracted heat (thermal power) P_f and bulk temperature $\overline{T}_f$ are calculated using the approximations shown in Eq. (5.11) and (5.13), respectively, for simplicity, which are enough for their prediction. Since fluid velocity and temperature are imposed at the receiver inlet, the only dependent variable in the integral of the second term of Eq. (5.11) is the density ρ_f, which is a function of the pressure at the inlet through the equation of state.

5.2.5 Receiver characteristics for the reference simulation

In the following, the geometric parameters and properties of the receiver are given, which were used for the reference simulation. Regarding the porous volumetric receiver element, the radius and height are $r_{rec} = 2.5$ cm and $L = 5$ cm, respectively, while the mean pores diameter and porosity are $d_p = 3$ mm and $\phi = 0.9$, respectively. The emissivity and thermal conductivity of the ceramic body are $\varepsilon = 0.84$ [35] and

$\lambda_s = 80$ W m^{-1} K^{-1} [8], respectively, while the emissivity of the side wall material is $\varepsilon_w = 0.8$ [10]. An asymmetry factor of the scattering phase function of $g = -0.25$ was used, which was very recently determined experimentally for the SiC ceramic foam [12] . It should be noted that the asymmetry factor g is one of the most important parameters in the modelling of radiation propagation and absorption in porous media. The value used was obtained through a combination of the MCRT method and experimental measurements of hemispherical diffuse reflectance of different samples of open-cell SiC ceramic foams [12]. The inlet boundary conditions for fluid velocity and temperature are $\vec{U}_{in} = (0, 0, 1.5)$ m s^{-1}, considering the same coordinate system of Fig. 5.1, and $T_{in} = 300$ K, respectively, and the pressure at the receiver outlet is $p_{out} = 1.013\,25 \times 10^5$ Pa.

5.3 Results and discussion

The governing equations were solved using finite volume method (FVM) in OpenFOAM [36], which is an open source CFD software. The validation of the global model (MCRT and CFD) is presented in the work by Barreto et al. [8], in which a very good agreement with other model results and experimental measurements was found. In the following, a detailed parametric analysis and optimisation procedure are presented, where the effect of porosity, pores size and inlet fluid velocity on the thermal and hydrodynamic performances are investigated. It should be noted that all the other parameters are fixed in this parametric analysis with the values presented in Section 5.2.5 for the selected reference configuration. It should also be noted that the mass flow rate $\dot{m}$ in the receiver changes when the internal structure (porosity and pores size) is modified because a pressure value is imposed at the outlet and velocity is specified at the inlet. Thus, when the internal structure is changed, the pressure drop also changes as a result of pressure and density variation at the inlet.

5.3.1 Effect of fluid velocity at inlet

The fluid velocity only affects the fluid flow and heat transfer conditions, with the spatial distribution of absorbed solar radiation remaining unchanged. Fig. 5.2 presents the effect of varying the fluid velocity on the thermal efficiency (η_{th}), mean fluid temperature at the outlet ($\overline{T}_f$) and pressure drop across the receiver (Δp). It should be noted that $|\vec{U}_{in}|$ represents the axial component of fluid inlet velocity, which according to the coordinates from Fig. 5.1 is the z direction (the velocity components in x and y directions are zero). Higher values of velocity decreases mean temperature and increase thermal efficiency and pressure drop. For lower values of velocity, the receiver is dealing with higher temperatures, which makes the thermal efficiency to decrease because of higher thermal losses.

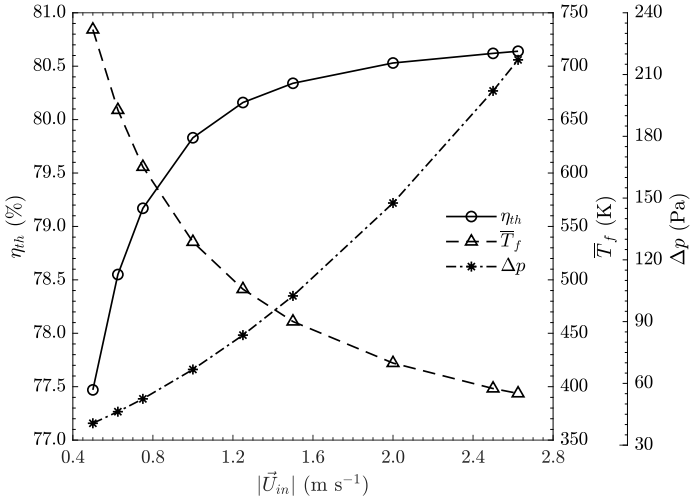

Fig. 5.2: Variation of thermal and hydrodynamic performances of the receiver element with the fluid inlet velocity.

5.3.2 Effect of porosity

The porosity of the receiver affects the spatial distribution of absorbed solar radiation, fluid flow and heat transfer conditions. Fig. 5.3 presents the effect of porosity on the thermal efficiency, mean fluid temperature at the outlet and pressure drop. The thermal performance is less affected than the hydrodynamic performance (pressure drop) when the porosity is changed. For a porosity range from 0.7 to 0.93, results show that there is a maximum of thermal efficiency and mean temperature at $\phi = 0.875$. The pressure drop is lower for receivers with higher values of porosity.

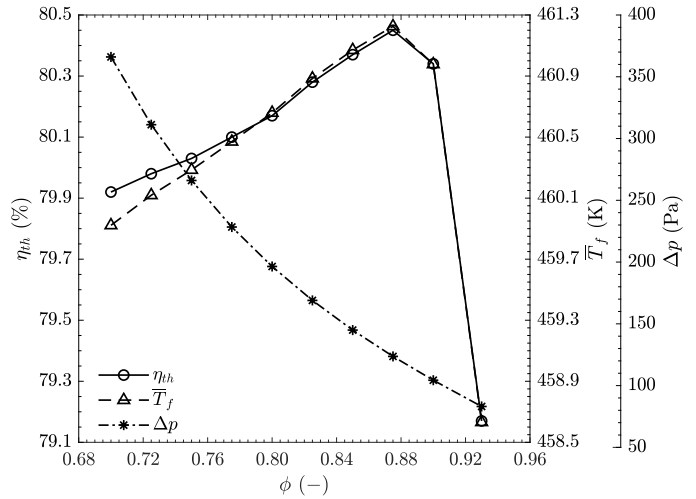

Fig. 5.3: Variation of thermal and hydrodynamic performances of the receiver element with porosity.

5.3.3 Effect of pores size

The pores size also affects the spatial distribution of absorbed solar radiation, fluid flow and heat transfer conditions. Fig. 5.4 presents the effect of pores size on the thermal efficiency, mean fluid temperature at the outlet and pressure drop. Results show that a mean pores size of $d_p = 3$ mm maximise both thermal efficiency and fluid temperature. The pressure drop is lower for larger pores, and there is a sharp increase for smaller pores. The different shape of the lines for thermal efficiency and temperature are due to the change in the total mass flow when different pores size are used.

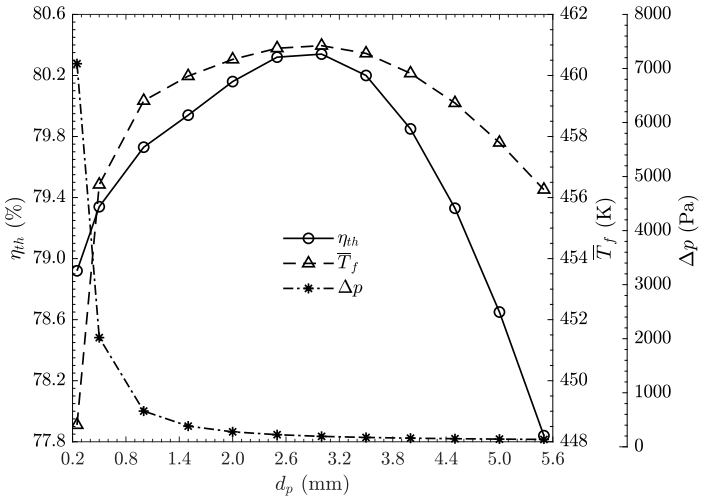

Fig. 5.4: Variation of thermal and hydrodynamic performances of the receiver element with pores size.

5.3.4 Effect of the combined variation of different parameters

In the following, the thermal and hydrodynamic performances are studied for receiver elements with different combinations of geometric parameters and fluid flow conditions. Fig. 5.5 presents the thermal efficiency for different values of pores size, porosity and fluid inlet velocity. In general, higher values of pores size and porosity increase the thermal efficiency of the receiver. However, since the porosity represents the amount of solid material in the receiver porous structure, it can be considered as a constraint for the receiver manufacturing process. Thus, if the porosity is considered as fixed (constrained), there is a mean pores size that maximise the thermal efficiency. The optimum pores size decreases with increasing porosity and, for example, for a porosity of $\phi = 0.85$, the value of pores size that maximise the thermal efficiency is $d_p = 4.5$ mm for both the fluid inlet velocity simulated, while for a porosity of $\phi = 0.9$ this value is $d_p = 3$ mm.

Fig. 5.6 shows the mean fluid temperature at the outlet for different values of pores

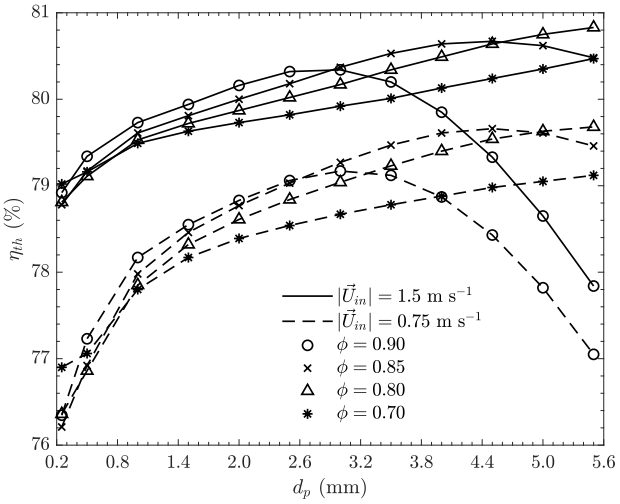

Fig. 5.5: Variation of the thermal efficiency of the receiver element with pores size, porosity and fluid inlet velocity.

size, porosity and fluid velocity. The effect of these parameters on this temperature is similar to that of thermal efficiency. The main difference is for lower values of pores size, where the temperature increases steepest than the thermal efficiency (Fig. 5.5 and Fig. 5.6). This difference is explained by the sharp decrease of pressure drop for increasing pores size (Fig. 5.7), which also causes a sharp decrease of the mass flow rate.

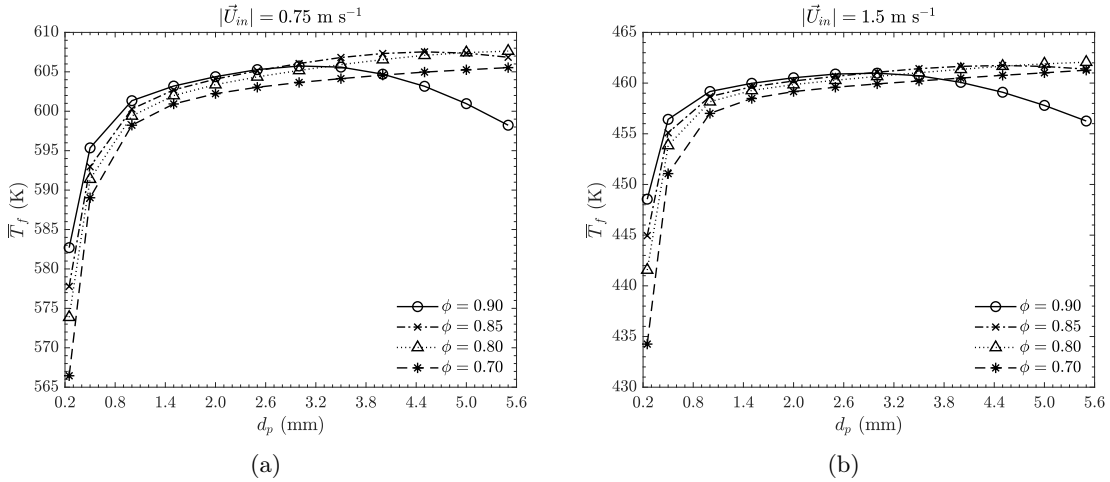

Fig. 5.6: Mean fluid temperature at the outlet of the receiver element with different pores size and porosity for a fluid inlet velocity of: (a) $|\vec{U}_{in}| = 0.75$ m s^{-1}; (b) $|\vec{U}_{in}| = 1.5$ m s^{-1}.

The pressure drop is directly related with the pumping power needed to force the fluid to flow through the receiver. Higher pressure drop means that more power are needed to pump the fluid. Fig. 5.7 shows the variation of pressure drop across the receiver element with pores size, porosity and fluid velocity. The pressure drop

is lower for receivers with higher values of pores size and porosity and lower fluid velocity, and it is more affected by the variation of pores size than porosity. For the configurations and flow conditions of Fig. 5.7, the required pumping power is approximately linearly related to the pressure drop, with values between 0.03 and 57 W.

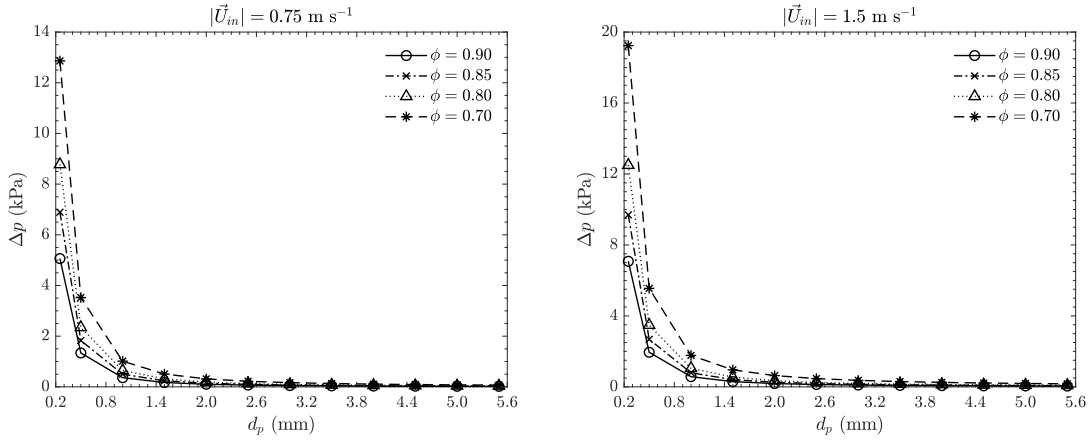

Fig. 5.7: Pressure drop across the receiver element with different pores size and porosity for a fluid inlet velocity of: (a) $|\vec{U}_{in}| = 0.75$ m s^{-1}; (b) $|\vec{U}_{in}| = 1.5$ m s^{-1}.

5.3.5 Discussion on the receiver optimisation

The receiver of choice should have good thermal and hydrodynamic performances, that is, high thermal efficiency while keeping low pressure drop and pumping power. Regarding the geometric parameters of the receiver (porosity and pores size), higher values are the choice in most cases to increase the thermal efficiency and to decrease the pressure drop. Since the porosity affects the thermal efficiency slightly, but significantly the pressure drop (Fig. 5.3), values of porosity between 0.8 and 0.9 are recommend because low pressure drop is achieved. Once the porosity is chosen, considering also the structural constraint of the porous media manufacturing, the pores size of the receiver should be selected in order to maximise the thermal efficiency while not increasing much the pressure drop. For receivers with porosity values between 0.7 and 0.8, larger pores size are the choice to improve both thermal and hydrodynamic performances. Considering the porosity that is being used in practical applications ($\phi \approx 0.85$) [12], the pores size of the receiver element should be $d_p \approx 4.5$ mm. As for receiver height, small receivers (thicknesses lower than approximately 5 cm) decrease the pressure drop and pumping power, but may increase the losses due to the solar radiation transmission. Therefore, in order to maximise the absorbed solar radiation in the receiver (source of heat), the height

should be selected such that the losses due to the solar radiation transmission are negligible. For example, for receiver thickness of 5 cm, the transmission loss is 0.61% for 0.85 and 4.5 mm of porosity and pores size, respectively.

Regarding the fluid inlet velocity, higher values increase the thermal efficiency and pressure drop and decrease the mean fluid temperature at outlet. For velocities of 0.75 m s^{-1} and 1.5 m s^{-1}, the geometric parameters that maximise the performance of the receiver are approximately the same. Therefore, for a given geometrically optimised receiver, the velocity of the fluid should be selected as a function of the desired fluid temperature at the receiver outlet, which can be determined by the system where the receiver is used, with an upper limit imposed by the available energy.

5.4 Conclusions

In this work, a detailed parametric analysis and optimisation of thermal and hydrodynamic performances of a porous volumetric receiver made of SiC open-cell foam in a solar concentration system is performed using a detailed three-dimensional numerical model. The model is based on the Monte Carlo Ray Tracing (MCRT) method to simulate the solar radiation transport and absorption in the porous media, and a Computational Fluid Dynamics (CFD) model to simulate the fluid flow and heat transfer phenomena. Mean fluid temperature at the outlet, thermal efficiency and pressure drop are investigated for different values of porosity, pores size and fluid velocity.

Results show that thermal and hydrodynamic performances of porous volumetric receivers are more affected by the variation of pores size than porosity. Higher values of porosity and pores size are the choice to decrease the pressure drop, but for thermal efficiency and mean fluid temperature at the receiver outlet there are optimum working conditions. The optimum geometric and operation conditions to achieve high thermal efficiency while not increasing pressure drop and not decreasing the mean fluid temperature correspond in most cases to a receiver with high porosity and pores size. For a fixed value of porosity, there is a mean pores size that maximise the thermal efficiency, being this value lower for increasing porosity. Two optimum configurations are highlighted here, which are a receiver with porosity $\phi = 0.85$ and a pores size that maximise the thermal efficiency of $d_p = 4.5$ mm, and a receiver with porosity $\phi = 0.9$ and an optimum value of pores size of $d_p = 3$ mm, with a height of 5 cm.

Higher values of fluid velocity at the receiver inlet increase the thermal efficiency and pressure drop and decrease the mean fluid temperature at the outlet. For velocities of 0.75 m s^{-1} and 1.5 m s^{-1}, the geometrically optimised receivers are

approximately the same. Then, the velocity of the fluid should be selected as function of the target fluid temperature at the outlet.

References

[1] O. Behar, A. Khellaf, and K. Mohammedi. A review of studies on central receiver solar thermal power plants. *Renew Sust Energ Rev*, 23:12–39, 2013.

[2] L. Teng and Y. Xuan. Design of a composite receiver for solar-driven supercritical CO2 Brayton cycle. *J CO2 Util*, 32:290–298, 2019.

[3] B. Coelho, S. Varga, A. Oliveira, and A. Mendes. Optimization of an atmospheric air volumetric central receiver system: Impact of solar multiple, storage capacity and control strategy. *Renew Energ*, 63:392–401, 2014.

[4] H. Yağlı, C. Karakuş, Y. Koç, M. Çevik, İ. Uğurlu, and A. Koç. Designing and exergetic analysis of a solar power tower system for Iskenderun region. *Int J Exergy*, 28:96–112, 2019.

[5] E. Casati, F. Casella, and P. Colonna. Design of CSP plants with optimally operated thermal storage. *Sol Energy*, 116:371–387, 2015.

[6] T. Fend, B. Hoffschmidt, R. Pitz-Paal, O. Reutter, and P. Rietbrock. Porous materials as open volumetric solar receivers: Experimental determination of thermophysical and heat transfer properties. *Energy*, 29:823–833, 2004.

[7] C. K. Ho and B. D. Iverson. Review of high-temperature central receiver designs for concentrating solar power. *Renew Sust Energ Rev*, 29:835–846, 2014.

[8] G. Barreto, P. Canhoto, and M. Collares-Pereira. Three-dimensional CFD modelling and thermal performance analysis of porous volumetric receivers coupled to solar concentration systems. *Appl Energy*, 252:113433, 2019.

[9] A. L. Avila-Marin, J. Fernandez-Reche, and A. Martinez-Tarifa. Modelling strategies for porous structures as solar receivers in central receiver systems: A review. *Renew Sust Energ Rev*, 111:15–33, 2019.

[10] G. Barreto, P. Canhoto, and M. Collares-Pereira. Three-dimensional modelling and analysis of solar radiation absorption in porous volumetric receivers. *Appl Energy*, 215:602–614, 2018.

[11] T. J. Hendricks and J. R. Howell. Absorption/Scattering Coefficients and Scattering Phase Functions in Reticulated Porous Ceramics. *J Heat Transfer*, 118:79–87, 1996.

[12] G. Barreto, P. Canhoto, and M. Collares-Pereira. Combined experimental and numerical determination of the asymmetry factor of scattering phase functions in porous volumetric solar receivers. *Sol Energ Mat Sol C*, 206:110327, 2020.

[13] M. Balat-Pichelin and A. Bousquet. Total hemispherical emissivity of sintered SiC up to 1850 K in high vacuum and in air at different pressures. *J Eur Ceram Soc*, 38:3447–3456, 2018.

[14] Z. Wu, C. Caliot, F. Bai, G. Flamant, Z. Wang, J. Zhang, and C. Tian. Experimental and numerical studies of the pressure drop in ceramic foams for volumetric solar receiver applications. *Appl Energy*, 87:504–513, 2010.

[15] Z. Wu, C. Caliot, G. Flamant, and Z. Wang. Coupled radiation and flow modeling in ceramic foam volumetric solar air receivers. *Sol Energy*, 85:2374–2385, 2011.

[16] P. Wang, J. B. Li, F. Bai, D. Y. Liu, C. Xu, L. Zhao, and Z. F. Wang. Experimental and theoretical evaluation on the thermal performance of a windowed volumetric solar receiver. *Energy*, 119:652–661, 2017.

[17] X. Chen, X.-L. Xia, X.-W. Yan, and C. Sun. Heat transfer analysis of a volumetric solar receiver with composite porous structure. *Energ Convers Manage*, 136: 262–269, 2017.

[18] S. Du, Q. Ren, and Y.-L. He. Optical and radiative properties analysis and optimization study of the gradually-varied volumetric solar receiver. *Appl Energy*, 207:27–35, 2017.

[19] S. Du, Y.-L. He, W.-W. Yang, and Z.-B. Liu. Optimization method for the porous volumetric solar receiver coupling genetic algorithm and heat transfer analysis. *J Heat Transf*, 122:383–390, 2018.

[20] F. Zaversky, L. Aldaz, M. Sánchez, A. L. Ávila-marín, M. I. Roldán, J. Fernández-Reche, A. Füssel, W. Beckert, and J. Adler. Numerical and experimental evaluation and optimization of ceramic foam as solar absorber – Single-layer vs multi-layer configurations. *Appl Energ*, 210:351–375, 2018.

[21] B. Wang, Y. Hong, L. Wang, X. Fang, P. Wang, and Z. Xu. Development and numerical investigation of novel gradient-porous heat sinks. *Energ Convers Manage*, 106:1370–1378, 2015.

[22] S. M. Besarati, D. Y. Goswami, and E. K. Stefanakos. Optimal heliostat aiming strategy for uniform distribution of heat flux on the receiver of a solar power tower plant. *Energ Convers Manage*, 84:234–243, 2014.

[23] M. E. Nimvari, N. F. Jouybari, and Q. Esmaili. A new approach to mitigate intense temperature gradients in ceramic foam solar receivers. *Renew Energ*, 122:206–215, 2018.

[24] X. Tao, X. KaiDi, Y. BoLun, and H. YaLing. Effect of pore size and porosity distribution on radiation absorption and thermal performance of porous solar energy absorber. *Sci China Tech Sci*, 62:1674–7321, 2019.

[25] Q. Zhu and Y. Xuan. Improving the performance of volumetric solar receivers with a spectrally selective gradual structure and swirling characteristics. *Energy*, 172:467–476, 2019.

[26] M. J. Blanco, J. M. Amieva, and A. Mancillas. The tonatiuh software development project: an open source approach to the simulation of solar concentrating systems. 157–164, 2005.

[27] D. Buie, A. G. Monger, and C. J. Dey. Sunshape distributions for terrestrial solar simulations. *Sol Energy*, 74:113–122, 2003.

[28] D. Buie, C. J. Dey, and S. Bosi. The effective size of the solar cone for solar concentrating systems. *Sol Energy*, 74:417–427, 2003.

[29] M. F. Modest. *Radiative Heat Transfer*. Academic Press, New York, third edition, 2013.

[30] L. G. Heney and J. L. Greenstein. Diffuse radiation in the Galaxy. *Astrophys*, J. 93:70–83, 1940.

[31] W. Sutherland. Lii. the viscosity of gases and molecular force. *The London, Edinburgh, and Dublin Philosophical Magazine and Journal of Science*, 36: 507–531, 1893.

[32] M. A. Schuetz and L. R. Glicksman. A basic study of heat transfer through foam insulation. *J Cell Plast*, 20:114–121, 1984.

[33] K. Kamiuto. *Modeling of Composite Heat Transfer in Open-Cellular Porous Materials at High Temperatures*, 165–198. Wiley-Blackwell, 2008.

[34] Z. Wu, C. Caliot, G. Flamant, and Z. Wang. Numerical simulation of convective heat transfer between air flow and ceramic foams to optimise volumetric solar air receiver performances. *Int J Heat Mass Tran*, 54:1527–1537, 2011.

[35] J. M. Jones, P. E. Mason, and A. Williams. A compilation of data on the radiant emissivity of some materials at high temperatures. *J Energy Inst*, 92:523–534, 2019.

[36] https://www.openfoam.com/, 2019.

Chapter 6

Conclusions

In this thesis, a detailed three-dimensional numerical model of porous volumetric receivers coupled to point-focus solar concentration systems was developed and validated, including the solar radiation propagation and absorption, fluid flow and heat transfer processes. An experimental investigation was also conducted in order to validate the solar radiation transfer model and to estimate the radiative properties of the porous media, which were then included in the global model. The model was used to conduct a comprehensive and complete parametric analysis of a cylindrical porous volumetric receiver element made of open-cell SiC (silicon carbide) ceramic foam aiming to find the geometric parameters and fluid flow conditions that maximise the receiver performance. The concentrated solar radiation flux at the receiver aperture was generated by modelling a parabolic dish concentrator, with radiation propagation and absorption in the porous media being modelled though an in-house developed Monte Carlo Ray Tracing (MCRT) method. The fluid flow and heat transfer processes are modelled solving the governing equations using an open-source Computational Fluid Dynamics (CFD) software (OpenFOAM). The global model is validated comparing the results with those from previous numerical models and experimental measurements available in literature. The main conclusions are presented in the following.

6.1 Development of the detailed numerical model

The global model is designed to use as input the concentrated solar radiation field at the receiver inlet. This makes it easily adjustable to simulate the performance of porous volumetric receivers when coupled to different concentration systems, such as heliostats in tower CSP plants, provided that the incident radiation is previously obtained, for example, via a ray tracing software. Moreover, the developed model considers not only the solar radiation intensity, but also the incidence angle, which is essential to accurately model the radiation propagation inside the receiver (in the case a heliostat field, for example). Results were compared with reference solutions available in the literature and good agreement was found. Regarding the fluid flow

and heat transfer, the LTNE approach is used and good agreement was also found with other solutions in the literature. Additionally, a detailed study of the effect of using different assumptions to describe the temperature profiles of fluid and solid near the side wall when adiabatic boundary condition is assumed is also presented in this thesis. It was found that using heat flux separation for the solid and fluid leads to more accurate results.

6.2 Radiative properties of the receiver

Regarding the radiative properties of porous volumetric receivers, the asymmetry factor of scattering phase function has been determined through the combination of the numerical model (MCRT) and experimental measurements. For this purpose, the total hemispherical reflectance of five different samples with optical thicknesses ranging from approximately 6 to 16 was both measured and numerically modelled. It was found that radiation scattering in the visible spectrum in open-cell SiC ceramic foam is slightly backwards, with an asymmetry factor when the Henyey-Greenstein phase function is used of approximately -0.25. It was also found that the isotropic scattering phase function underestimates the diffuse reflectance, while the phase function obtained through modelling of packing of spheres with diffuse reflection surface overpredicts the diffuse reflectance of open-cell SiC foams.

6.3 Thermal and hydrodynamic performance of the receiver

The porosity and pores size of the porous volumetric receivers strongly affect the spatial distribution of absorbed solar radiation, temperature of both phases, and fluid flow and heat transfer conditions. It was found that the pores size is the most influential parameter. Regarding the concentrated solar radiation flux at the receiver inlet, it was found that convergent incident angles lead to peaks of temperature in the solid and fluid. These hot spots exist more often in receivers with high porosity and pores size. For these conditions, hot spots in the solid material are in the region close to the focal point of the concentration system, while in the fluid are slightly downstream in direction of the flow due to the convection. A way to minimise these hot spots is to design the concentration system or place the receiver in such way to obtain lower incidence angles at the inlet, which also leads to an increases of the thermal efficiency because slightly lower temperatures are obtained for this configuration. It was also found that in the core flow region close to the outlet of the receiver an inversion of temperature difference may occur, where the fluid is hotter than the solid, which means that there is heat transfer from the fluid to the porous structure. This is mainly due to low depth of solar radiation propagation,

which causes low absorption, and thus low temperature of the porous material in that region.

It was found that the main thermal losses of porous volumetric receivers are due to the propagation and absorption of the solar radiation in the porous media through diffuse reflectance (backscattering). Depending on the porosity and pores size, a fraction of the incident solar radiation is lost through the inlet plane due to backscattering. In porous volumetric receivers made of open-cell SiC ceramic foam the diffuse reflectance is approximately between 14% and 17%. Lower reflectances can be achieved by using or designing porous structures that provide more forward scattering, which can be obtained by changing the pores geometry and orientation, and by improving the optical properties of the porous material. Another technique is to design the receiver as a cavity for example, aiming at to absorb and redirect to other part of the receiver some amount of the backscattered solar radiation.

The conditions to achieve high thermal efficiency while not increasing pressure drop and not decreasing the mean fluid temperature at outlet correspond in most cases to a receiver with high porosity and pores size. For a given value of porosity, there is a mean pores size that maximise the thermal efficiency, being this value lower for increasing porosity. Two optimum configurations are highlighted in this thesis, which are a receiver with porosity $\phi = 0.85$ and a pores size that maximise the thermal efficiency of $d_p = 4.5$ mm, and a receiver with porosity of $\phi = 0.9$ and an optimum value of pores size of $d_p = 3$ mm. In these cases, the maximum efficiency is 79.66% and 79.17%, respectively, while the mean temperature of the gas (air) at the outlet is 334.38 °C and 332.59 °C, respectively, for an incident concentrated solar radiation of 374.86 kW m^{-2} and inlet fluid velocity of $|\vec{U}_{in}| = 0.75$ m s^{-1}.

Regarding the velocity of fluid at the receiver inlet, higher velocities increase the thermal efficiency and pressure drop and decrease the mean fluid temperature at the outlet. It was found that the geometric parameters that optimise the receiver performance do not depend significantly of the inlet velocity. Therefore, the velocity of the fluid should be selected as function of target temperature at the receiver outlet.

6.4 Future work

As for future work, two main research lines can be followed: (i) use of the developed numerical model to study new designs of porous volumetric receivers in open and closed systems coupled to different solar concentration systems; and (ii) experimental study of different samples and designs of porous volumetric receiver elements aiming to validate the global model with experimental measurements. New designs that decrease the diffuse reflectance losses through the receiver aperture (cavity receivers and structured porous media, for example), which is the main way to further increase

the thermal efficiency, should be considered in the future. For the experimental study, temperature in the solid and fluid can be measured for different conditions of solar radiation flux (different positions of the receiver, for example) and fluid flow (mass flow rate and temperature, for example), and then compared with results obtained with the global model for the same conditions, which permits to better calibrate the model. When considering the entire CSP plant (including the thermodynamic cycle), the main way to increase the global efficiency is the use of a pressurized gas as heat transfer fluid in the receiver (closed system), as for example, carbon dioxide at supercritical conditions. Combining this type of receivers with solar concentration systems with high concentration factors (high temperatures) and a Brayton cycle will increases the efficiency of the plant.

The developed numerical model includes significant additional details regarding previous models, but some parts can be further improved. This can be, for example, modelling of the transient response and further improvements on the boundary conditions. The latter will increase the accuracy of the results when the model is used to study this type of receivers for higher temperature applications.

UNIVERSIDADE DE ÉVORA
INSTITUTO DE INVESTIGAÇÃO
E FORMAÇÃO AVANÇADA

Contactos:

Universidade de Évora

Instituto de Investigação e Formação Avançada - IIFA

Palácio do Vimioso | Largo Marquês de Marialva, Apart. 94

7002-554 Évora | Portugal

Tel: (+351) 266 706 581